Analytic Optimization Modeling of Anti-Reflection Coatings for Solar Cells

ANALYTIC OPTIMIZATION MODELING OF ANTI-REFLECTION COATINGS FOR SOLAR CELLS

BY

SARRY AL-TURK, B.A.Sc.

A THESIS

SUBMITTED TO THE DEPARTMENT OF ENGINEERING PHYSICS

AND THE SCHOOL OF GRADUATE STUDIES

OF MCMASTER UNIVERSITY

IN PARTIAL FULFILMENT OF THE REQUIREMENTS

FOR THE DEGREE OF

MASTER OF APPLIED SCIENCE

Master of Applied Science (2011)   McMaster University

(Engineering Physics)   Hamilton, Ontario, Canada

TITLE: Analytic Optimization Modeling of Anti-Reflection
                    Coatings for Solar Cells

AUTHOR: Sarry Al-Turk

                    B.A.Sc. (Engineering Science)

                    University of Toronto, Toronto, Canada

SUPERVISOR: Dr. Rafael Kleiman

NUMBER OF PAGES: xii, 94

Abstract

The world's dependence on oil cannot continue indefinitely. As reserves dwindle and demand continues to increase, prices will soar to new highs and fundamentally change the way society deals with energy generation and consumption. Use of oil and other carbon-based fuels also have detrimental effects on human health, as pollution that arises from the combustion of these fuels necessitates treating respiratory problems in millions of people annually. Moreover, evidence that climate change is anthropogenic has become undeniable and has been proven to be direct related to dependence on carbon-based fuels.

Renewable energy offers clean and dependable alternatives for electricity, heating and transport. In particular, solar energy looks to be the most promising owing to its sheer abundance and ubiquity. The main obstacle hindering the adoption of solar cell technology en masse is cost. One of the ways to reduce cost is to fabricate thinner solar cells, but this compromises efficiency due to lower optical absorption that results, especially in silicon. In order to become a serious competitor in the energy market, highly absorptive solar cells must be developed at reduced material costs, which is the essence of light-trapping.

In this study, two of the most common ways to trap light by reducing reflection were investigated: the application of anti-reflection coatings and surface texturing in silicon. Analytic models were created to optimize optical design in both single-junction and multi-junction solar cells. The single-junction silicon models accounted for non-normal incidence, which allowed angle-averaged calculations to be made for planar and textured surfaces. Single-junction GaAs models included a GaInP window layer whose optical effects were considered in anti-reflection coating optimization. The multi-junction GaAs-on-silicon (GaAs/Si) and AlGaAs-on-silicon (AlGaAs/Si) models that were created clearly demonstrated the need to adjust individual subcell thicknesses in order to optimize optical design.

Acknowledgements

Contents

List of Figures

List of Tables

Chapter 1

Introduction

1.1. Renewable Energy and Solar Power

Sustainable energy development is a multidimensional issue with environmental, economic, social and political aspects. Pollution, climate change and lack of energy security are all consequences of the exploitation of non-renewable energy sources such as oil, natural gas, coal and uranium. Besides the detrimental effects to human health and the environment that result from use of these energy sources, there remains the issue of the energy availability for future generations. For example, analyses show that oil production will irreversibly start declining within the next few decades, even according to the most optimistic scenarios [1]. Coupled with the fact that global demand for energy will undoubtedly continue to increase (Figure 1.1), the need for renewable energy becomes increasingly apparent.
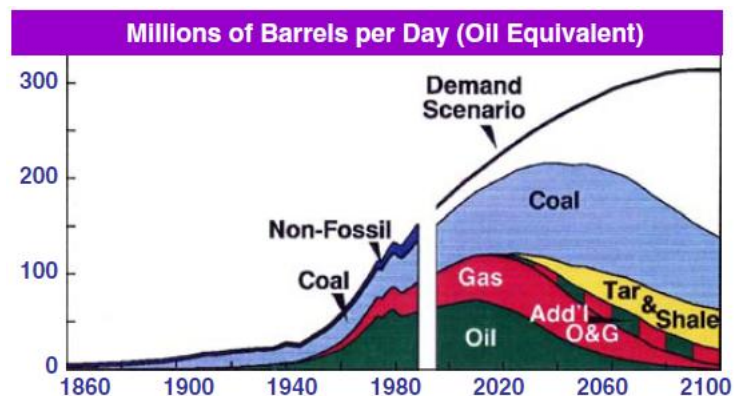
Figure 1.1: World energy supply and demand, historical and projected. Source: [2]

Renewable energy is generated from natural sources and is replenished naturally over time. Types of renewable energy include solar (electric or thermal), hydroelectric, tidal, wind and geothermal. Of these, solar energy holds the promise of being a significant portion of all energy generated globally in the future as it dwarfs all other forms of energy combined, including non-renewables. The sun irradiates the earth with 120,000 TW of energy continuously, while the world's current energy consumption rate is around 13 TW [2]. In theory, the world would be able to fulfill all its energy needs if only a fraction of the energy from the Sun could be harnessed.

However, solar energy has several shortcomings. One issue is that the energy source is diffuse, so harnessing a large amount of energy requires a large area. Another is that it is intermittent; storing solar energy is difficult and presently not very economical. Other issues are installation costs of solar power systems and the high material cost of the modules. Electrical components of the system, such as charge controllers and inverters, have shorter lifetimes than the modules and need to be replaced more often.

Despite these limitations, solar energy has many aspects working in its favour. Apart from being the most abundant (and a practically infinite) energy source, solar energy is everywhere; in contrast, most of the world's oil reserves are concentrated in a handful of geographic locations. It is ideal for power in remote areas not connected to energy grids and for satellites in orbit. Solar modules do not produce emissions or any other type of pollution, have no moving parts (with the exception of trackers in concentrator systems) and require little maintenance. They are easily scalable; solar power systems can range from several kilowatts on a rooftop to tens of megawatts on solar farms.

Most of the worldwide production of solar cells today focuses on silicon because it is much cheaper and more abundant (Figure 1.2) than other semiconductors. Unfortunately, it displays low optical absorption which requires relatively large cell thicknesses. This raises the cell's cost per watt, and it is well-recognized that this cost must decrease in order for solar energy to become a serious competitor to non-renewable sources [3]. Reduction of silicon cell thickness, while decreasing material cost, should not compromise the maximum amount of light absorbed in the cell, lest efficiency be also compromised. Because optical absorption is such an important issue, optical losses must be minimized as much as possible. In the last 50 years, numerous techniques have been investigated to trap light in solar cells. Deposition of anti-reflection coatings (ARCs) and surface texturing have become the most widely-used methods in silicon cells, their success owing to the convenience in which they can be implemented and their relatively low cost compared to other, more elaborate light-trapping techniques.

Year	Annual solar-cell production*	Material		
		Si (c-Si)	Te (CdTe)	In (CuInSe$_2$)
2000	0.3 GW$_p$	4	0.03	0.03
2005	1.5 GW$_p$	15	0.15	0.15
2020	50 GW$_p$	150	5	5
World production (1,000 tonnes per year)		1,000	0.3	0.5
Reserve base (1,000 tonnes)		Abundant	47	6

Figure 1.2: Annual solar cell production and the required materials feedstock, as well as reserves. Source: [4]

1.2. Thesis Overview

The motivation behind this thesis was to create thorough and realistic models with the purpose of optimizing ARC design for solar cells. An analytic method was chosen in order to provide greater control over the models and to gain a deeper understanding of the principles of optical design. While similar work has been carried out in the past, it has come with certain limitations such as neglecting dispersion [5] or non-normal incidence on textured silicon [6, 7]. This study sought to form a more complete investigation in optical design of single-junction solar cells. Additionally, there was also the motivation of creating models for multi-junction solar cells with a silicon bottom junction and a III-V semiconductor top junction. Although not widely used, such solar cells benefit from reduced cost by having a silicon subcell as opposed to more expensive semiconductors. Futhermore, with the right top subcell material, III-V/silicon solar cells can compete in efficiency with some triple-junction cells.

Chapter 2

Review of Light-Trapping Techniques

2.1. Anti-Reflection Coating Design for Single- and Multi-Junction Solar Cells

While optical phenomena arising from thin films have been observed for centuries, it was not until the 19th century that scientists were able to develop a theory for the nature of light to sufficiently explain and make use of these observations. According to [8], the first ARCs were probably made by Joseph Fraunhofer in 1817, just one year after Augustin Jean Fresnel developed his diffraction theory based on the works of Thomas Young and Christiaan Huygens, and 56 years before James Clerk Maxwell published his treatise on electromagnetism. Despite this early development, there was not much progress in anti-reflection technology mainly due to the lack of necessary instrumentation to deposit and analyze thin films, which came around the early- to mid-20th century. The first practical solar cell was announced in 1954 [9]; although it did not employ any ARCs, they became a common feature shortly thereafter.

The simplest use of ARCs is to apply a single layer on the surface of the solar cell substrate. The arrangement is optimized by choosing a material with an appropriate thickness and refractive index (the square root of the refractive index of the substrate, as discussed in section 3.4.1.), at which point reflectance becomes minimized at a particular wavelength. Usually the wavelength of choice is close to the peak of the solar spectrum. The material is usually an oxide or a nitride; among the most common are Si_3N_4, SiO_2, TiO_2 and Al_2O_3 [5, 10-12]. Si_3N_4 is widely used in silicon solar cells because it can also passivate the surface, thereby increasing carrier collection efficiency; the same is true of SiO_2 but it is used to a lesser extent as its refractive index is lower than optimal [12].

A slightly more complex ARC arrangement is the use of two layers. Two materials of varying thicknesses, when optimized, allow minimal reflectance at a broader range of wavelengths. Whereas a single-layer coating can lower average reflectance to ~10% under normal incidence (~20% under angle-averaged incidence), a double-layer coating can decrease it further to ~4% (~10%). The most commonly used double-layer coating combination is MgF_2/ZnS [5, 13-16]; others include MgF_2/BN [13], MgF_2/TiO_2 [17] and Al_2O_3/TiO_2 [15, 18, 19].

The greater the number of layers in an ARC arrangement, the lower the average reflectance becomes, provided the materials are chosen such that they are close to the optimal refractive indices:

$$n_m = n_{sup}^{\left(\frac{M+1-m}{M+1}\right)} n_{sub}^{\left(\frac{m}{M+1}\right)}$$

where n_m is the refractive index of the mth layer out of M layers, n_{sub} is the refractive index of the substrate and n_{sup} is the refractive index of the superstrate [15]. In practice, however, more than two layers are rarely employed for several reasons. Firstly, the added complexity and processing time that comes with additional layers is not justified by the slight increase in performance [19]. As illustrated in Figure 2.1, the decrease in reflectance is usually minimal after two layers.
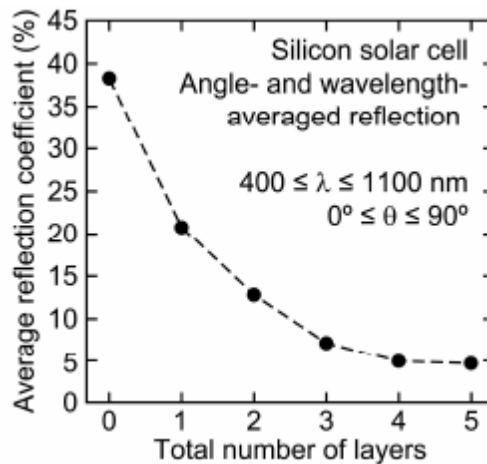
Figure 2.1: Reflection coefficient (i.e. percentage of light reflected), angle- and wavelength-averaged, as a function of the number of layers for optimized ARCs for silicon solar cells. Source: [20]

5
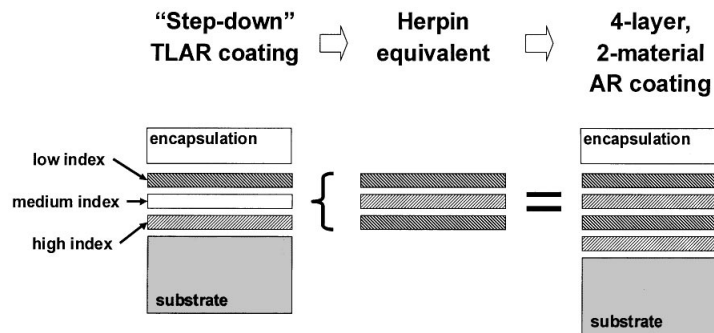
Figure 2.2: Thin film replaced by a Herpin equivalent. Source: [19]

More importantly, as the number of layers increases, it becomes more difficult to find suitable materials with refractive indices that closely match the values required (in addition to being transmissive, chemically and mechanically stable, and ably deposited in thin-film form) [19]. One way to bypass this obstacle is through the use of symmetrical multi-layer combinations called Herpin equivalent layers, named after André Herpin. A film with a refractive index that is unavailable or impractical can be replaced by a symmetrical combination of materials with refractive indices that are higher and lower, thus creating the Herpin equivalent (Figure 2.2). When properly constructed, the stack has approximately the same total optical thickness and the same equivalent refractive index as the single film [19]. The Herpin equivalence is not a true physical equivalence and is only valid at one wavelength and angle of incidence; nevertheless, it is able to outperform double-layer structures (Figure 2.3) although it has been shown to be more sensitive to thickness variation than both double- and triple-layer arrangements [19].
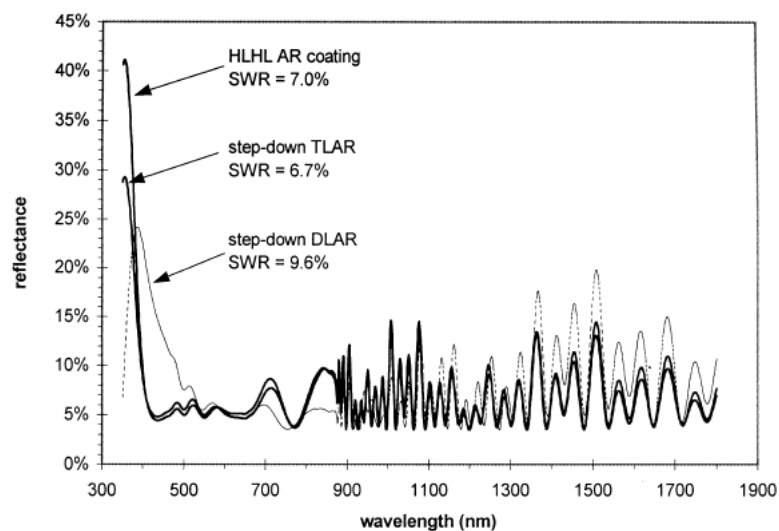
Figure 2.3: Comparison of modeled reflectance of different ARC structures. Source: [19]

6

Another way to sidestep the need to find new materials with certain refractive indices is to alter the composition or deposition process of existing materials in order to tailor their refractive indices. One such method involves the use of oblique-angle deposition and self-shadowing to create nanoporous films. By changing the deposition angle, the porosity of the film can be varied and its refractive index can be controlled – the higher the angle, the lower the refractive index. Refractive indices in SiO_2 as low as 1.05 have been reported [20]. Another method that can be used to fine-tune a film's refractive index is the simultaneous deposition of two materials, referred to as co-sputtering. By varying the relative deposition rate of each material – and hence the composition of the film – a refractive index value can be attained that lies between those of the deposited materials. This has been carried out with SiO_2 and TiO_2 in silicon single-junction solar cells and GaInP/GaAs/Ge triple-junction solar cells, in conjunction with nanoporous SiO_2 thin films [20].

Yet another technique is to create a graded refractive index ARC in an attempt to mimic an ideal one. An ideal ARC is one that reduces reflection at all wavelengths and angles, which would be possible in a thin film with a gradual increase in refractive index from ambient (or superstrate) to substrate (Figure 2.4). While this is not presently possible owing to the lack of dielectrics with very low or very high refractive indices, materials can be fabricated with graded refractive indices within a certain range. Silicon oxynitrides, SiO_xN_y, are a common choice [22, 23], although mixtures of silicon and titanium oxides have been suggested due to the high refractive index of TiO_2 [22]. By modifying the composition of the SiO_xN_y film as it is grown, the refractive index can be varied between ~1.45 (SiO_2) and ~2.1 (Si_3N_4). While a linear profile of refractive index against ARC depth is simplest, more complicated profiles such as the "Fermi" profile in Figure 2.5 have been shown to be more optimal.
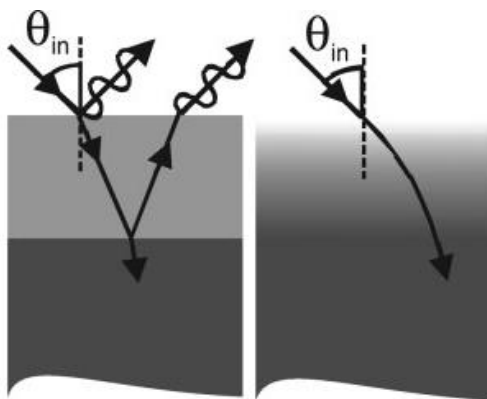
Figure 2.4: Interference in a single-layer homogeneous coating vs. an ideal graded refractive index coating. Source: [21]
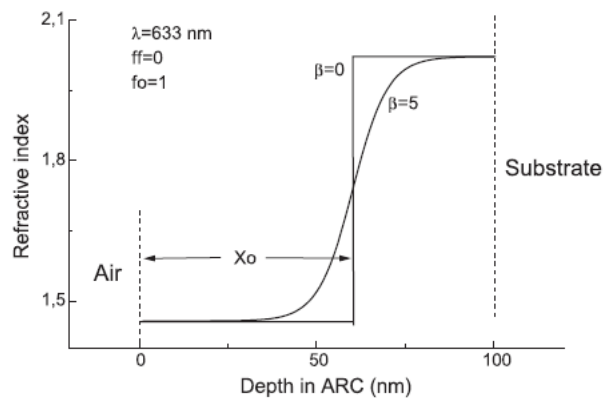
Figure 2.5: "Fermi" profile of refractive index in a graded ARC. Source: [22]

Regardless of which of the aforementioned ARC techniques is used in a solar cell, it must be optimized in order to help maximize the cell's efficiency. However, optimization is approached differently in multi-junction solar cells compared to single-junction solar cells. In the latter, the objective is to simply couple as much light as possible into the cell since the more light is trapped, the greater the generated photocurrent and the higher the efficiency of the device. Thus, ARC design should serve to minimize reflection to the greatest extent over the relevant part of the solar spectrum. This is usually a straightforward task, especially in classical ARCs. In multi-junction solar cells, proper ARC design is more difficult for several reasons. Firstly, multi-junction solar cells often have a larger spectral range and so require ARCs that are more broadband [18]. Secondly, while the objective remains to couple as much light as possible, there is the added requirement of ensuring that the light is dispersed throughout the device so that the subcells produce the same amount of current. This need for current-matching means the optimization process minimizes reflectance in certain spectral regions (where a subcell is underpowered) while increasing it elsewhere (for overpowered subcells) [18]. Multi-junction cells are also more likely to be sensitive to variations in ARC design because a slight deviation from optimal parameters can easily result in current mismatch between subcells [18]. Lastly, since multi-junction solar cells are often used in concentrator systems that affect the device temperature, a temperature-dependent reflectance spectrum may arise from variations in the temperature-dependence of the refractive index of each coating layer. This in turn may affect performance [15].

2.2. Surface Texturing of Silicon

Surface texturing has long been used as a reflection-reducing technique in silicon solar cells and combining it with ARCs has been a standard feature since the mid-1970s [24]. In the most general sense, texturing involves roughening the silicon surface to scatter or redirect light. The most common texturing method is wet chemical etching in an alkaline solution, usually KOH or NaOH. Immersing single-crystalline silicon substrates in the solution leads to anisotropic etching; the resulting surface morphology is dependent on the orientation of the wafer and the relative etch rate between different crystal planes. For effective light coupling in solar cells, (100)-oriented substrates are textured so that the surface becomes composed of square-based pyramids (Figure 2.6) formed by (111) crystal planes, which etch much more slowly than (100) planes [25]. The pyramid heights and base widths are usually on the order of several microns, meaning reflection falls within the framework of geometric optics. Pyramid size can vary greatly, but the distribution can be made narrower by controlling the many variables of the texturing

process: etch time, solution temperature, solute concentration, etc. [26]. Anisotropic etching can be performed in multi-crystalline silicon wafers as well, but the random orientation of crystalline planes reduces its effectiveness. Multi-crystalline silicon is often etched in acidic solutions or by mechanical means, and sometimes through laser texturing or reactive ion etching [27].
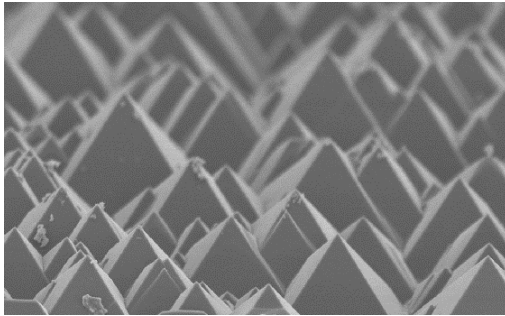
Figure 2.6: SEM cross-section image of textured (100)-oriented silicon. Source: [28]
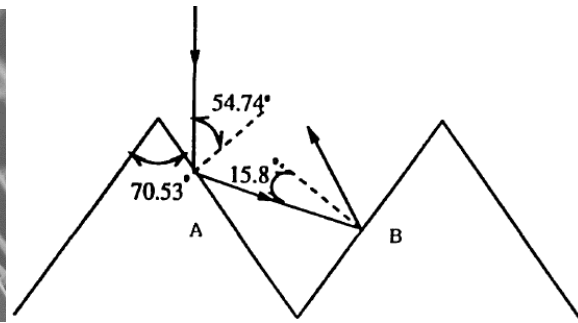
Figure 2.7: Double reflection on a textured silicon surface. Source: [6]

Texturing of (100)-oriented silicon substrates is particularly useful because of the multiple surface reflections it creates. Whereas in a planar silicon substrate any reflected light is lost, on a textured substrate light is redirected to another part of the surface (the so-called "double-bounce" effect, illustrated in Figure 2.7). This leads to partial transmission of light into the substrate on two separate pyramidal facets. Thus, reflection is reduced from a value R to approximately R^2, a much smaller number. This surface morphology is also favoured at high angles; for example, when light is incident at an angle of 55° to the substrate, it is actually at near-normal incidence to some of the pyramidal facets. Another benefit to surface texturing is an increase in quantum efficiency in the 600 nm – 1,100 nm wavelength range compared to planar silicon cells [29]. This occurs due to the fact that light entering a textured substrate does so at an angle, which increases its optical path length and provides long-wavelength photons with low absorption coefficients a higher chance of absorption. One downside to surface texturing is that it can cause damage that reduces collection efficiency; however, this can be offset by the passivation effect of some ARCs [22].

It has been reported that the symmetrical, square-based pyramids resulting from wet chemical etching are not ideal for light coupling and that a lower degree of symmetry offers a greater degree of light trapping. For example, tilted pyramids have been shown to offer better performance than their symmetrical counterparts when combined with a

planar rear surface [30]. This is due to the fact that light rays re-striking pyramidal facets from within at a different angle at which they entered the substrate have a higher probability or being internally reflected (Figure 2.8). This results in more reflection and a greater chance for absorption. Interestingly, tilted pyramids can be formed quite easily: cutting silicon wafers off-axis towards the (110) plane at the sawing stage prior to a routine etch. Furthermore, the tilt need not be great: angles of tilt as small as 5° for encapsulated cells and 8° for unencapsulated cells are sufficient [30]. Other possible non-symmetric textures include grooves and pyramids at various facet angles; however, these morphologies require the silicon to be mechanically textured [31].
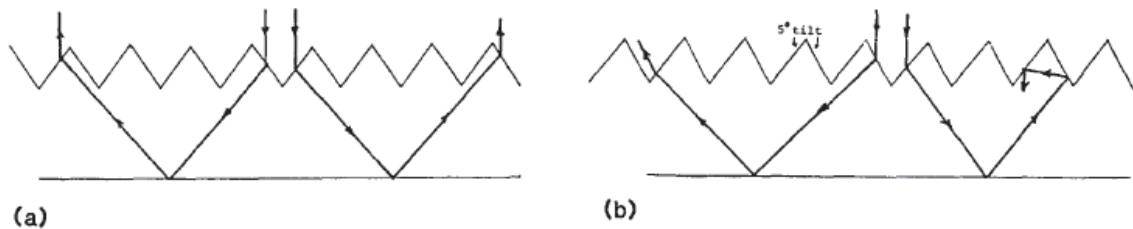
Figure 2.8: Light trapping in symmetrically (left) and asymmetrically (right) textured silicon. Source: [30]

There is also some interest in silicon texturing at the submicron level/nanoscale, where light falls within the framework of wave optics. Research has shown that wet and reactive ion etching can be combined with laser interferometric lithography to create one- and two-dimensional structures at or below the wavelength of light [32]. The lasers are used to create interference effects that produce periodic patterns. Part of the interest in this technique arises from the fact that low-cost poly-silicon substrates can be used as well [32].

2.3. Transparent Conductive Layers

Although more widely used in thin-film solar cells such as cadmium telluride (CdTe), copper indium gallium selenide (CIGS) and tandem amorphous/microcrystalline silicon (a-Si/μc-Si), another light-trapping method is the use of a transparent conductive layer (TCL). TCLs are usually doped oxides with high bandgaps to allow for high optical transparency and low electrical resistance. They are also required to be mechanically, thermally and chemically stable [33]. TCLs are attractive because they can serve multiple purposes in a solar cell: in addition to serving as an ARC, they passivate the surface and replace the front metallic-grid electrode, thus eliminating shadowing [15]. Their use in

multi-junction solar cells is coupled with extra constraints, however. As previously mentioned, multi-junction solar cells are usually more broadband and so require a TCL that is transparent over a large spectral range. Furthermore, since multi-junction solar cells are often used in concentrated photovoltaic systems that produce greater resistive losses, there exists a trade-off between resistivity and transparency in the film [15]. TCLs are also considerably thicker than classical ARCs and can range from 200 nm to over 1 μm in thickness.
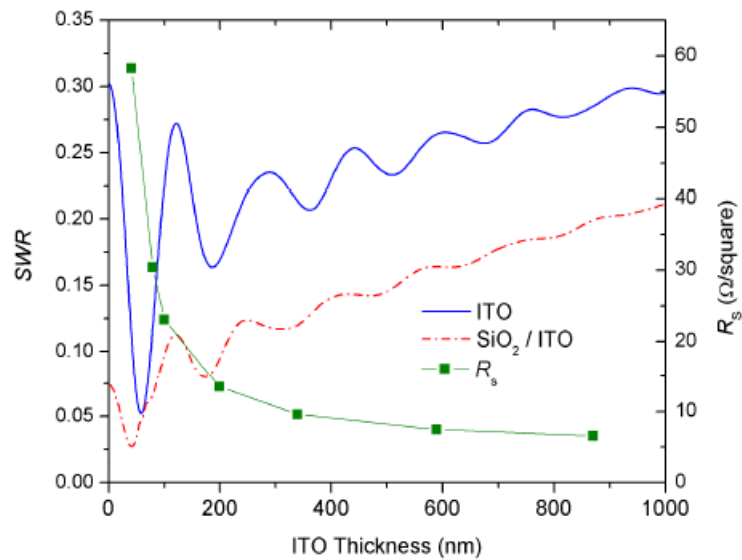
Figure 2.9: Solar-weighted reflectance and sheet resistance vs. ITO thickness. Modified from [15]

While many articles have been published about TCLs [33], experiment and discussion appear to revolve around a few select materials. Among the most commonly used ones is tin-doped indium oxide (also called indium tin oxide, ITO). ITO is favoured for its high transparency in the visible spectrum and high conductivity [33]. However, although its properties are strongly deposition-dependent, ITO exhibits high absorption in the infrared region [15]. As a result, reflectance tends to increase as ITO thickness increases, as shown in Figure 2.9. One way to keep transparency high without compromising conductivity is to apply a thin, low-refractive index material such as SiO_2 over the ITO to create a double-layer ARC combination [15]. Some have taken this further and applied an extra nanoporous SiO_2 layer through oblique-angle deposition to effectively create an oblique $SiO_2/$ SiO_2/ITO triple-layer ARC [34]. Relatively to the SiO_2/ITO combination, it has been shown to increase the conversion efficiency by up to 3.5%.

Another disadvantage of ITO is the cost and availability of indium [4]. This has led to interest in TCLs composed of cheaper and more abundant elements such as tin (in SnO_2) and zinc (in ZnO). The former is often fluorine-doped (SnO_2:F) and the latter is usually doped with aluminum or gallium (ZnO:Al or ZnO:Ga). ZnO is preferred to SnO_2 due to the fact that it can be deposited at lower temperatures [35] and at higher rates with scaling up to 1 m^2 [3], which are important in mass manufacturing. Their surface morphologies are similar, as is their optical properties (Figure 2.10). The texured surface of ZnO (which eliminates the need to texture the substrate) can be obtained in two ways: texturing can take place after deposition through a chemical etching process using a diluted acidic solution [36], or it can be naturally formed during deposition [35, 37, 38]. The latter case is not limited to one deposition method, as several have been reportedly used including expanding thermal plasma CVD, low-pressure CVD and laser molecular beam epitaxy.
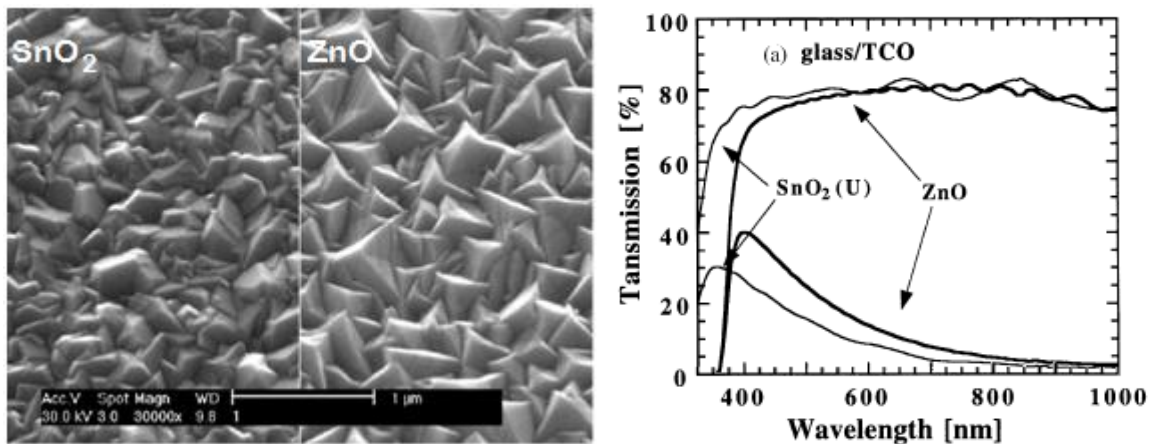
Figure 2.10: SEM images (left) and transmission graphs (right) of deposited SnO_2 and ZnO. Source: [37]

2.4. Nanostructures

A more recent development in light-trapping technology is the use of structural components on the nanoscale. For example, nanowires (Figure 2.11) have demonstrated the graded refractive index effect achieved in some ARCs. As in surface texturing, this type of design is favoured at higher angles of incidence. It has been shown that nanowires that are tapered (i.e. nanocones) outperform those with a constant diameter [21]. In a case of biomimicry, an ordered arrangement of nanocones has been shown to imitate the eyes of moths, which are known to have anti-reflective properties [39]. The AlInP nanocones in the square array in Figure 2.12 have a period of 300 nm, a height of 190 nm and a base

diameter of 130 nm. They were formed by nanoimprint lithography on a GaAs substrate. At normal incidence, they exhibited an average reflectance of 2.7% in the 450 nm – 1650 nm range. It is claimed that these broadband anti-reflective structures can be fabricated cost-effectively [39].
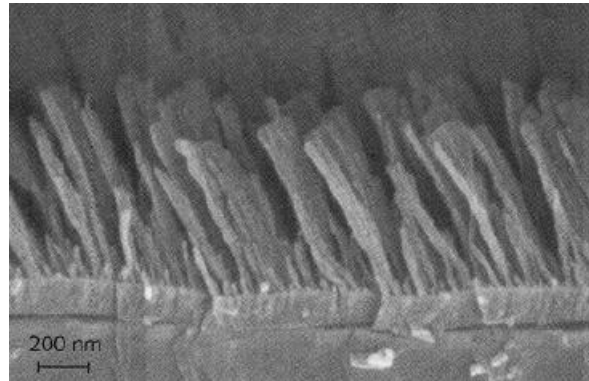
Figure 2.11: SEM image of nanowires. Source: [40]
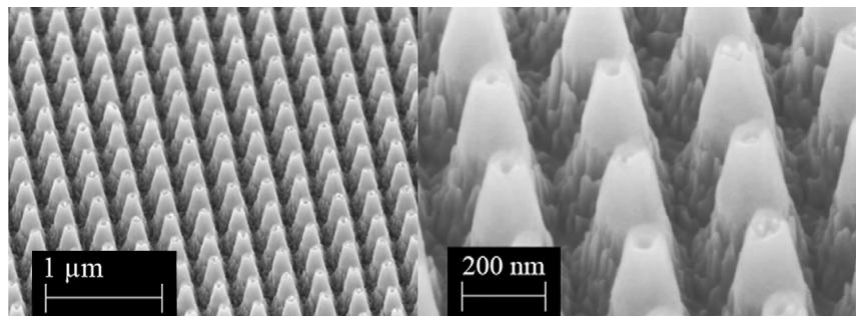
Figure 2.12: SEM images of nanocones at different magnifications. Source: [39]

Another approach is to vastly shrink the nanostructures in all dimensions, creating nanoparticles; specifically, metallic nanoparticles that support surface plasmons. Surface plasmons are excitations of the conduction electrons at the interface between a metal and a dielectric and occur when photons interact with nanoparticles [4]. The interaction can be used in several ways, as illustrated in Figure 2.13. For instance, nanoparticles situated near the surface of a solar cell can scatter light internally (Figure 2.13a). This occurs because scattering from nanoparticles – which is normally equal in forward and reverse directions – close to the interface between two dielectrics occurs preferentially in the dielectric with the larger permittivity [4]. If a metal back contact is present, light reflected from the rear towards the nanoparticles can be reabsorbed and scattered into the cell again, thereby increasing the optical path length of the light [4]. This has been

demonstrated with gold nanoparticles in three-junction InGaP/InGaAs/Ge solar cells. The nanoparticles, 2 nm in size, were deposited by placing drops of colloidal solution onto the surface of solar cells. Their implementation increased the short-circuit current of the device by 13.3%, yielding a 3% increase in absolute efficiency (22.6% compared to 19.6%) [41].
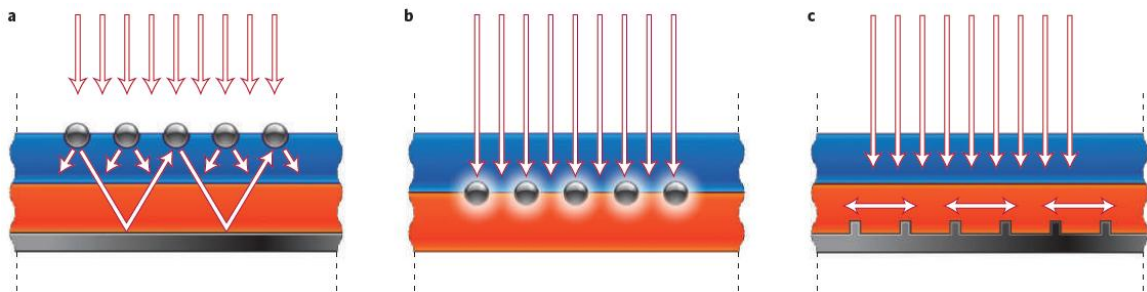
Figure 2.13: Possible light-trapping mechanisms from nanoparticles in solar cells. Source: [4]

Nanoparticles can also be embedded inside the solar cell, near the p-n junction (Figure 2.13b). This makes use of the strong local field enhancement around the metal nanoparticles to increase absorption in the surrounding semiconductor material [4]. This local field generates charge carriers in the semiconductor and becomes particularly useful in materials with small carrier diffusion lengths. Lastly, light can be converted into surface plasma polaritons, which are electromagnetic waves that travel along the interface between a corrugated metal back contact and the semiconductor absorber layer [4]. Polaritons excited at this interface can trap light and guide it laterally into the solar cell. (Figure 2.13c). Since solar cell width is much greater than thickness, absorption can be greatly increased especially among long-wavelength photons. The ridges on the back contact are approximately 50 nm in height.

There are also other reasons to incorporate nanostructures in solar cells. Their integration on the surface can reduce surface sheet resistance, leading to greater output power. Additionally, nanoscale metal contacts could potentially reduce shadowing loss that results from coverage of macroscopic metal fingers [4].

Chapter 3

Theory

3.1. Solar Spectrum

Until the end of the 19th century, it was accepted that light was a wave and obeyed Maxwell's equation like x-rays, microwaves, radio waves and other parts of the electromagnetic spectrum. The blackbody problem, among others, forced scientists to re-evaluate their understanding of the nature of light. In 1900, Planck proposed [42] that electromagnetic radiation is composed of discrete packets of energy; Einstein later called these packets "photons". These two seemingly contradictory views of light, the wave nature and particle nature, can be reconciled through quantum mechanical theory. If a photon is thought of as a collection of waves, then its behaviour depends of how spatially localized that wave-packet is; it acts as a particle when highly-localised, otherwise it acts as a wave. This concept is referred to as "wave-particle duality" and is observed among other elementary particles as well.

Photons can be characterised by their energy, frequency of wavelength. A relation exists between all three:

$$E = h\nu = \frac{hc}{\lambda}$$

where

- E is the energy of the photon;
- ν is its frequency;
- h is Planck's constant, 6.63×10^{-34} J · s;

- c is the speed of light in a vacuum, 3.00×10^8 m/s;
- λ is the wavelength of the photon.

To understand the characteristics of sunlight, it is useful to model the Sun as a blackbody. A blackbody is an object that, upon absorbing all electromagnetic radiation incident on its surface, emits a spectrum of light that is dependent on its temperature. This, of course, is a mathematical ideal; in reality, objects reflect and are transparent to electromagnetic radiation to some degree. Nevertheless, many physical objects can be approximated as having blackbody properties, including the Sun. The temperature-specific distribution emitted by blackbodies is governed by Planck's law [43]:

$$I(\lambda, T) = \frac{2hc^2}{\lambda^5 \left(e^{\left(\frac{hc}{\lambda kT}\right)} - 1 \right)}$$

where:

- I is the spectral irradiance (power per unit area for a given wavelength);
- k is Boltzmann's constant, 1.38×10^{-23} J/K;
- T is the absolute temperature;
- h, c and λ are as previously defined.

To approximate the Sun's spectrum, an irradiance with T = 6,000 K in Planck's law is often used (although the surface temperature of the Sun is slightly lower [44]).

It is important to distinguish between the irradiance at the top of the Earth's atmosphere and the irradiance reaching the surface of the Earth. While the former is mostly constant, the latter is affected by many factors including latitude, time of day and year, cloud cover, and absorption/scattering in the atmosphere. Atmospheric effects, in particular, allow for the designation of different spectra according to air mass (AM), which quantifies the reduction in irradiance as light passes through the atmosphere. It is defined as $1/\cos(\theta)$ where θ is the angle from the vertical, as in Figure 3.1 below. This, of course, assumes that the atmosphere is flat whereas in reality its curvature more or less matches the Earth's; nevertheless, it remains a useful metric in distinguishing solar spectra. For example, AM1.0 is the spectrum for when the Sun is directly overhead, while AM2.0 is when the Sun makes a 60° angle with the vertical (meaning light effectively travels through twice as much atmosphere). By definition, AM0 is the irradiance above the Earth's atmosphere (extraterrestrial spectrum).
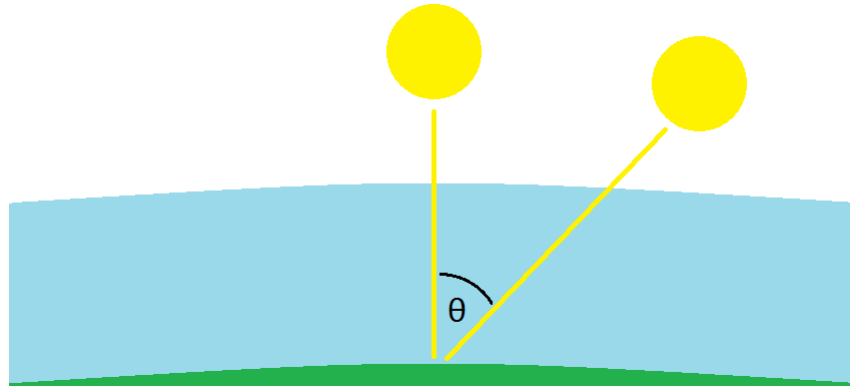
Figure 3.1: Sunlight travelling to the Earth's surface through two different air masses.

AM1.5 is used as a standard spectrum for testing solar cells because it represents "a reasonable average for the 48 contiguous states of the United States of America over a period of one year" [45]. A distinction must be made, however, between the direct and diffuse radiation that comprise the spectrum. Direct radiation is that which travels straight from the Sun to the surface of the Earth, whereas diffuse radiation is that which is scattered from the atmosphere and local surroundings. This distinction is important when considering concentrated photovoltaic systems, which do not make use of diffuse radiation, and are thus characterised by the AM1.5D spectrum (D = direct). Unconcentrated photovoltaics can make use of both direct and diffuse radiation, i.e. the AM1.5G spectrum (G = global = direct + diffuse). A comparison of the irradiance from these spectra, as well as a 6,000 K blackbody and the AM0 spectrum, is presented in Figure 3.2 below.
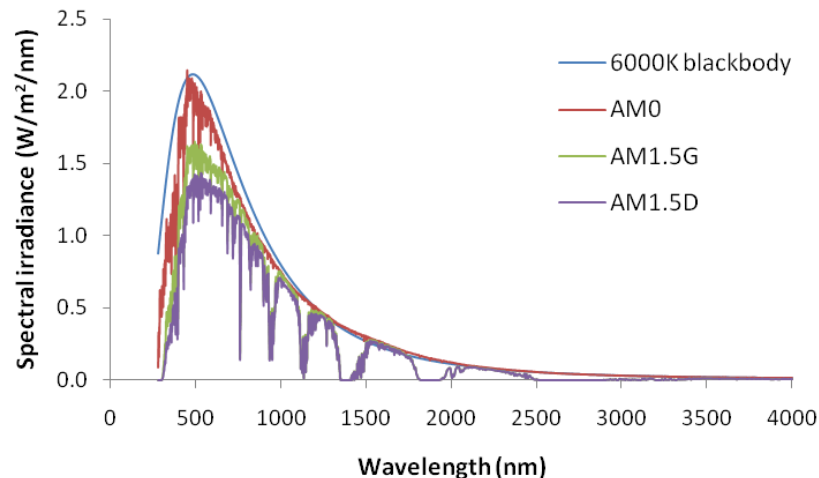
Figure 3.2: Comparison of several solar spectra and a 6,000 K blackbody spectrum. Data from [45]

3.2. Solar Cells

3.2.1. Overview

Solar cells are essentially p-n junction devices that are capable of converting photon energy into electrical power and delivering it to a load. In a p-n junction, an n-type semiconductor is brought into contact with a p-type semiconductor. Free electrons from the n-type material and free holes from the p-type material naturally diffuse across the junction to their opposite sides, leaving behind ionized donor atoms from which they originated. This separation of charge gives rise to an electric field that prevents further diffusion across the junction. The result is an area around the junction, referred to as the depletion region, acting as a potential barrier. In a solar cell, electron-hole pairs can be generated across the depletion region under illumination of photons with sufficient energy. Electrons in the valence band are promoted to the conduction band, leaving holes behind; this is called the photovoltaic effect, illustrated in Figure 3.3. The difference in potential between the conduction band and valence band is referred to as the semiconductor bandgap and is proportional to the output voltage of the solar cell. The charge carriers are then swept out of the depletion region by the electric field with the aim of collecting them before they can recombine. The ratio of the number of carriers collected to the number of photons absorbed by the solar cell is the internal quantum efficiency, IQE (also called the carrier collection efficiency). Ideally, every photon absorbed would result in the collection of an electron-hole pair so that the IQE would be unity across the solar spectrum above the semiconductor's bandgap energy. In reality, however, the IQE is reduced due to factors such as high surface recombination velocity, low diffusion length and low absorption coefficients of photons in the near-infrared.
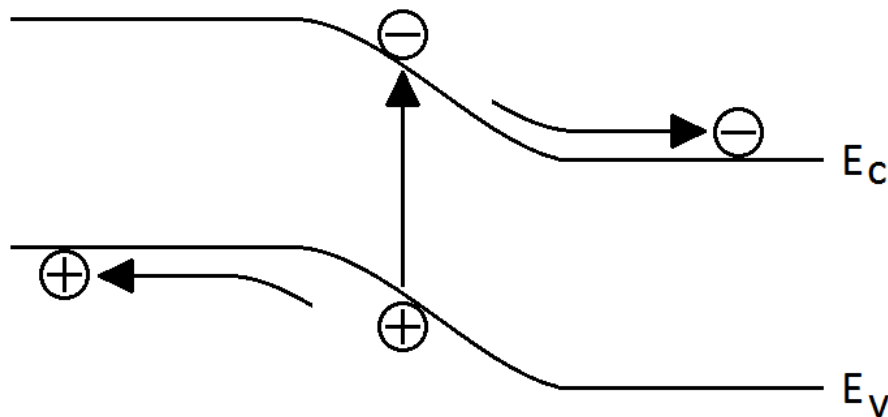
Figure 3.3: Illustration of the photovoltaic effect.

The built-in electric field causes excess minority electrons to drift to the n-type area and excess minority holes to drift to the p-type area. This spatial separation produces a photocurrent density J_{sc} across the cell in the reverse-bias direction. However, it also produces a voltage drop across the load which forward-biases the p-n junction, resulting in another (forward-bias) current density J_F. The net current density across the junction in the forward-bias direction is then found to be:

$$J = J_F - J_{sc} = J_0[e^{\left(\frac{qV}{k_B T}\right)} - 1] - J_{sc}$$

In other words, the net current density in an ideal solar cell is the current density described by the ideal diode equation minus the generated photocurrent density. The power delivered to the load is the product of the applied voltage and the current generated at that voltage. The maximum power is not simply the product of the maximum voltage (the open-circuit voltage, V_{oc}) and the maximum current density (the short-circuit current density, J_{sc}), since at the point of maximum voltage the current density in the cell is zero and vice versa. For this reason, J_{mp} and V_{mp}, the current density and voltage at which maximum power is delivered, are sometimes used to characterize cells rather than J_{sc} and V_{oc}.

The efficiency of a solar cell is defined as the ratio of output electrical power to incident optical power:

$$\eta = \frac{P_{out}}{P_{in}} = \frac{J_{mp} \cdot V_{oc}}{P_{in}} = \frac{FF \cdot J_{sc} \cdot V_{oc}}{P_{in}}$$

FF is the fill factor, a measure of the realizable power from a solar cell. This is depicted graphically in Figure 3.4 as the ratio of the area of the shaded region to the total area under the I-V curve. Low efficiency is usually attributed to a small short-circuit current density (indicating poor carrier collection efficiency or high optical loss) or a small fill factor (indicating high series resistance or low shunt resistance within the device).
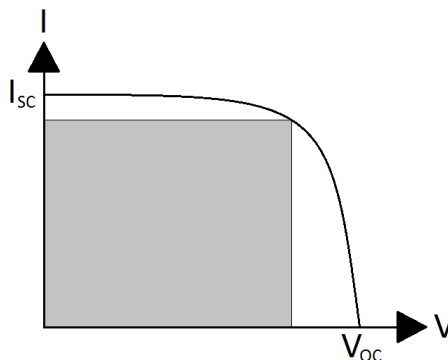
Figure 3.4: Typical I-V curve for a solar cell.

3.2.2. Single- vs. Multi-Junction Solar Cells

A major drawback of single-junction solar cells is the fundamental limit to their efficiency, called the detailed balance limit [46]. This limit is often quoted at 31%, although it depends on a number of factors such as material bandgap, spectral irradiance and optical system concentration. A number of photovoltaic technologies are being developed with the purpose of surpassing this limit; these technologies are collectively referred to as third-generation solar cells (the first generation being single-junction solar cells restricted by the detailed balance limit and the second generation being thin-film technologies that offer lower cost but no improvements in efficiency). One third-generation approach is to create a multi-layer stack of different photovoltaic materials: a multi-junction solar cell. Whereas single-junction solar cells are composed of only one p-n junction from a material such as silicon, their multi-junction counterparts are composed of many p-n junctions of different materials (usually compound semiconductors). The advantage of this design is that the bandgap of each p-n junction – or subcell – can be tailored to absorb a certain wavelength range, so that a larger portion of the solar spectrum can be utilized (Figure 3.5).
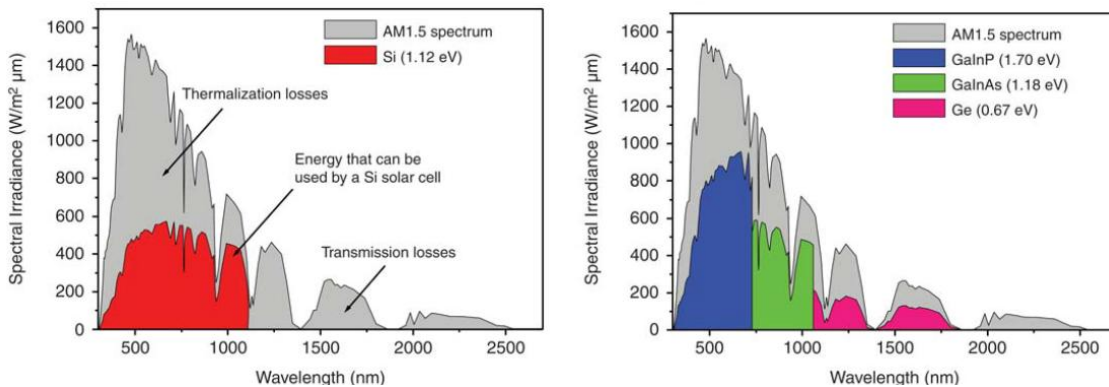
Figure 3.5: Spectral range of silicon solar cells (left) and triple-junction GaInP/GaInAs/Ge solar cells. Source: [47]

The cross-section of a generalized multi-junction solar cell is shown in the Figure 3.6. Multi-junction solar cells are able to surpass the detailed balance limit of efficiency due to the fact each subcell produces its own voltage and current density that contribute to the overall power output. Since the subcells are connected in parallel, the output voltage is the sum of the individual voltages generated. However, this also means that the current densities throughout the subcells must be equal (which is usually ensured through the use of tunnel junctions), so the current density of the device is the minimum of the current densities generated. As such, current matching becomes an issue in multi-junction solar

cells. The primary method of current matching is to vary the thicknesses of the subcells so as to adjust their absorption profiles. Proper ARC design is also used as a current matching technique by lowering reflection in the spectral region for current-limiting subcells and increasing it elsewhere.

$$V = V_1 + V_2 + ... + V_N$$
$$I = \min (I_1 , I_2 , ... , I_N)$$
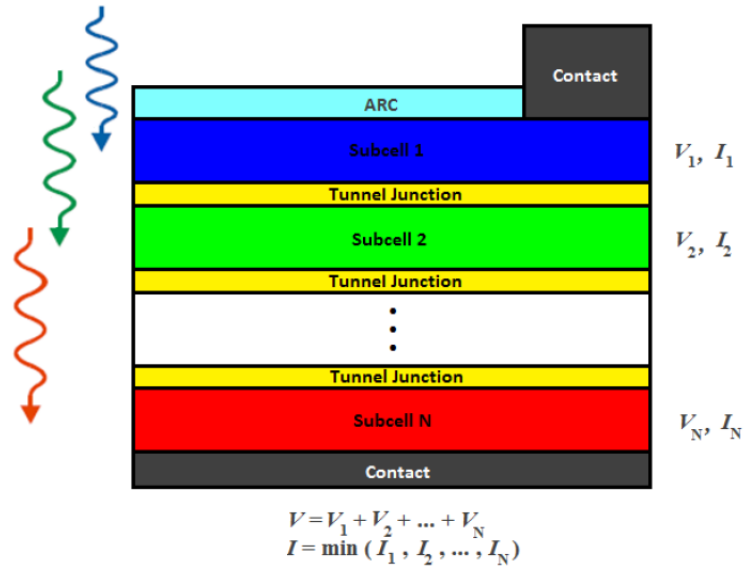
Figure 3.6: Cross-section of a multi-junction solar cell with N subcells.

3.3. Optical Properties of Materials

3.3.1. Refractive index

In free space, light travels at 3.0 x 10^8 m/s, a constant denoted by the letter c. In other media, however, light travels more slowly since photons interact with the atoms comprising the media. The ratio of the speed of light in free space to its speed v in any particular medium is called the refractive index:

$$N = \frac{c}{v}$$

The refractive index is usually a complex number with a real and imaginary part:

$$N = n - i \cdot k$$

where n is the real refractive index (often referred to simply as the refractive index), k is the extinction coefficient (also called the damping constant) and i is the imaginary unit (i^2 = -1). The real refractive index indicates phase speed while the extinction coefficient is a measure of the absorption in a material. Both parts are wavelength-dependent, a phenomenon known as dispersion. An example is given in the Figure 3.7 which shows how both n and k vary with wavelength in silicon. The refractive indices of other materials relevant to this thesis are presented in Appendix A.
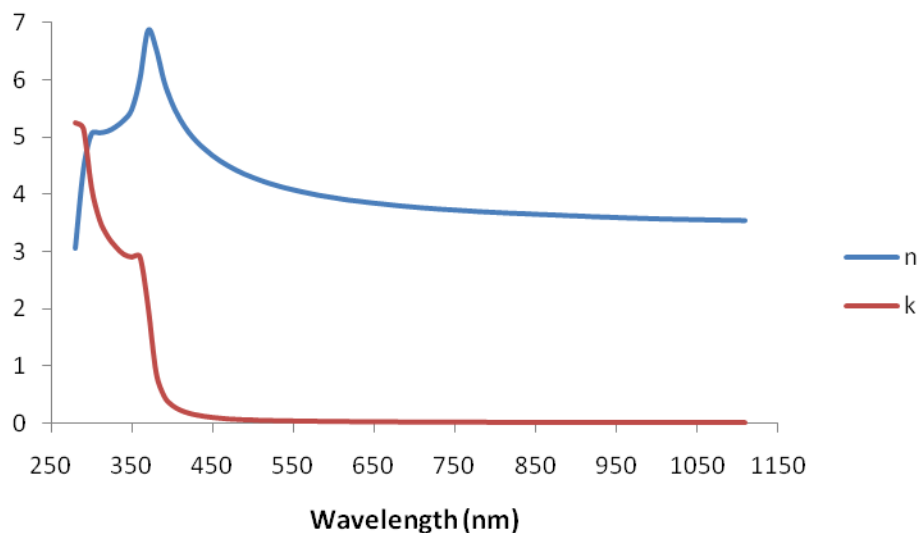
Figure 3.7: Real and imaginary parts of the refractive index of silicon. Data from [48]

The following section describes how the real and imaginary parts of refractive index are related to reflection and absorption in materials.

3.3.2. Reflection and Absorption

3.3.2.1. Reflection

When a wave is incident on the boundary between two media, a fraction of its energy is reflected back into the first medium and the rest is transmitted into the second. This applies to electromagnetic waves, including light. In this case, the reflected and transmitted quantities depend on multiple factors:

- differences in the refractive index of the media;
- the angle of incidence upon the boundary;

- the polarization of the incident light.

The equations that allow one to calculate reflectance and transmittance are called the Fresnel equations; a simplified derivation adapted from [49] is presented here.

In Figure 3.8 below, a linearly polarized electromagnetic wave is incident on the boundary between two media at point P. The xz- and xy- planes define the plane of incidence and the boundary interface, respectively. The electric field component of the wave is oscillating orthogonally to the plane of incidence, while the magnetic field component lies in the plane of incidence; this is referred to as transverse electric (TE) mode of propagation.
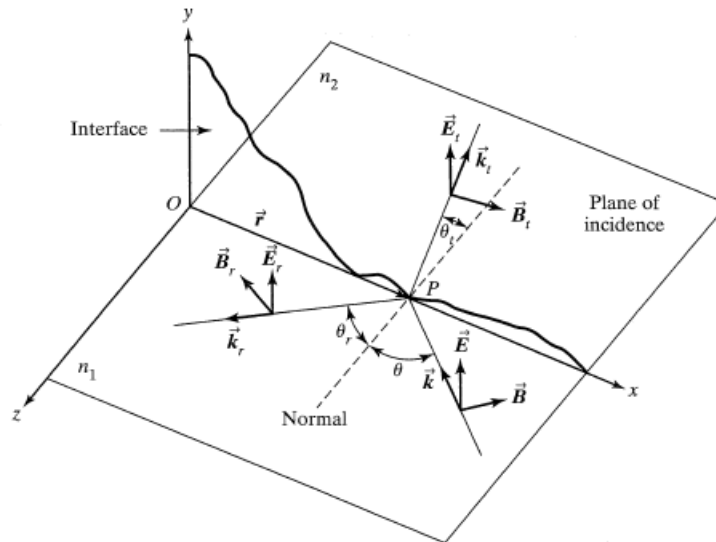
Figure 3.8: TE-polarized light incident on the boundary between two media. Source: [49]

At the boundary, it is required that the components of the electric field parallel to the interface be continuous; denoting E, E_r and E_t to be the amplitudes of the incident, reflected and transmitted components (respectively), then:

$$E + E_r = E_t \quad (3.1)$$

Similarly, it is also required that the parallel components of the magnetic field be continuous:

$$B\cos(\theta) - B_r \cos(\theta) = B_t \cos(\theta_t) \quad (3.2)$$

If the magnetic field component of the wave were oscillating orthogonally to the plane of incidence while the electric field component were to lie in the plane of incidence, as in the Figure 3.9, the mode of propagation would instead be transverse magnetic (TM). However, even in this case the continuity of the parallel components of the electric and magnetic fields is still required at the boundary:

$$-B + B_r = -B_t \quad (3.3)$$

$$E\cos(\theta) + E_r\cos(\theta) = E_t\cos(\theta_t) \quad (3.4)$$
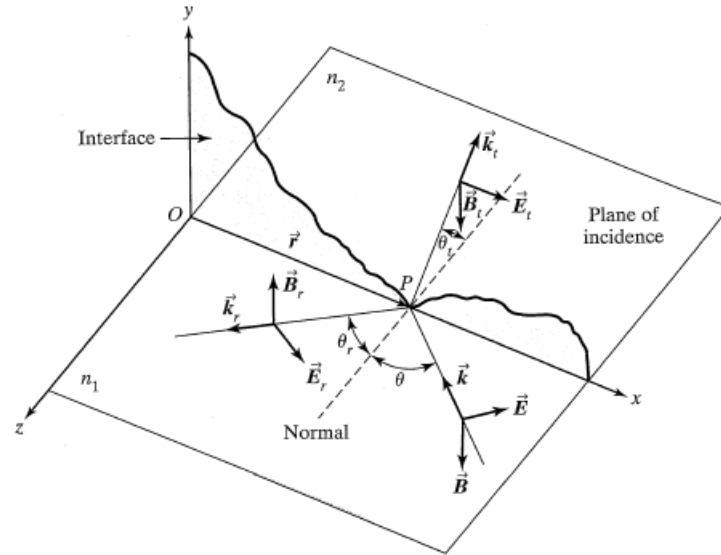
Figure 3.9: TM-polarized light incident on the boundary between two media. Source: [49]

Using the relation between electric and magnetic fields:

$$E = \frac{c}{n}B$$

equations (3.2) and (3.3) can be written as:

$$n_1 E\cos(\theta) - n_1 E_r\cos(\theta) = n_2 E_t\cos(\theta_t) \quad (3.5)$$

$$-n_1 E + n_1 E_r = -n_2 E_t \quad (3.6)$$

The pair of TE equations (3.1) and (3.5) and the pair of TM equations (3.4) and (3.6) can be solved simultaneously after eliminating E_t and defining the ratio $r \equiv E_r/E$:

$$r_{TE} = \frac{\cos(\theta) - \left(\frac{n_2}{n_1}\right)\cos(\theta_t)}{\cos(\theta) + \left(\frac{n_2}{n_1}\right)\cos(\theta_t)} \quad (3.7)$$

$$r_{TM} = \frac{-\left(\frac{n_2}{n_1}\right)\cos(\theta) + \cos(\theta_t)}{\left(\frac{n_2}{n_1}\right)\cos(\theta) + \cos(\theta_t)} \quad (3.8)$$

θ_t can be eliminated using Snell's law, $n_1\sin(\theta) = n_2\sin(\theta_t)$, and the following relation:

$$\left(\frac{n_2}{n_1}\right)\cos(\theta_t) = \left(\frac{n_2}{n_1}\right)\sqrt{1 - \sin^2(\theta_t)} = \sqrt{\left(\frac{n_2}{n_1}\right)^2 - \sin^2(\theta)}$$

Thus, the TE reflection coefficient from equation (3.7) can be written as:

$$r_{TE} = \frac{\cos(\theta) - \sqrt{\left(\frac{n_2}{n_1}\right)^2 - \sin^2(\theta)}}{\cos(\theta) + \sqrt{\left(\frac{n_2}{n1}\right)^2 - \sin^2(\theta)}}$$

The TM reflection coefficient from equation (3.8) can be written as:

$$r_{TM} = \frac{-\left(\frac{n_2}{n_1}\right)^2\cos(\theta) + \sqrt{\left(\frac{n_2}{n_1}\right)^2 - \sin^2(\theta)}}{\left(\frac{n_2}{n_1}\right)^2\cos(\theta) + \sqrt{\left(\frac{n_2}{n_1}\right)^2 - \sin^2(\theta)}}$$

Finally, reflectance is simply the square of the reflection coefficient, $R = r^2$. For linearly polarized light, either r_{TE} or r_{TM} is used depending on the polarization orientation, but in the case of unpolarized light a linear combination of the two is used:

$$R = \frac{(r_{TE}^2 + r_{TM}^2)}{2}$$

It must be noted that when the Fresnel equations are applied to metals, the real refractive index must be replaced with the complex refractive index ($N = n - i \cdot k$). This is also true when applying the equations to semiconductors if the light has energy greater than the semiconductors' bandgap. In the case of dielectrics, or if the light has energy less than the semiconductors' bandgap, the extinction coefficient is usually much lower in value than the real refractive index so that only the latter need be considered.

3.3.2.2. Absorption

The amplitude of an electromagnetic wave incident on an optically dense material decreases exponentially with the distance through the material. This is called the Beer-Lambert law and can be expressed as the following:

$$I(x) = I_0 e^{-\alpha x}$$

where $I(x)$ is the irradiance for a given wavelength at a distance x into the material, I_0 is the irradiance at the surface and α is the absorption coefficient. The amount absorbed (absorptance) is then:

$$a(x) = \frac{I_0 - I(x)}{I_0} = 1 - e^{-\alpha x}$$

The absorption coefficient is directly related to the extinction coefficient by the relation:

$$\alpha = \frac{4\pi k}{\lambda}$$

Figure 3.10 shows the absorption coefficient of silicon as a function of wavelength. Materials with high extinction coefficients are able to absorb light much more easily than materials with low extinction coefficients. The result is that a semiconductor such as gallium arsenide can be much thinner than a semiconductor such as silicon and still be able to absorb as much light. In fact, the thickness of gallium arsenide solar cells is often two orders of magnitude smaller than that of silicon solar cells.
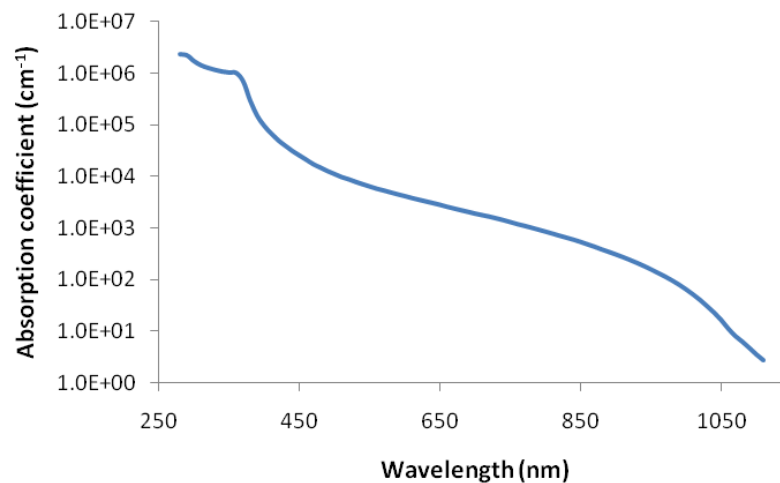
Figure 3.10: Absorption coefficient of silicon. Data from [48]

3.4. Anti-Reflection Coatings

3.4.1. Basic Principles

The key idea behind ARCs is interference of light. When a thin film of transparent material rests on a much thicker material, incident light on this arrangement undergoes two external reflections: one at the surface of the film, and another at the boundary of the film and substrate. This is depicted in Figure 3.11. The light beam that traverses the film eventually recombines with the beam which was reflected from the film surface; however, due to the difference in path length, a phase difference arises between the two beams. In the case of normal incidence, the second beam travels an extra optical distance of twice the thickness of the film times its refractive index:

$$\Delta = 2n_1 t$$

If this optical path difference is equal to one wavelength of the (monochromatic) light, the interfering beams find themselves in phase and the light is perfectly reflected. On the other hand, if the optical path difference is equal to half the wavelength, the beams interfere destructively. Mathematically:

$$\Delta = 2n_1 t = \frac{\lambda_0}{2} \quad \text{or} \quad t = \frac{\lambda_0}{4n_1}$$
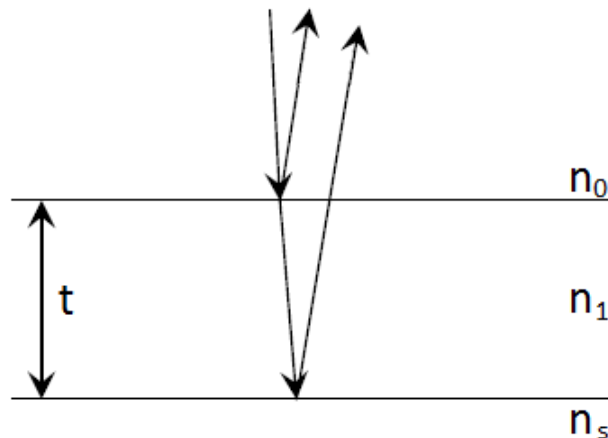
Figure 3.11: External reflection at the surface of the film and the film/substrate boundary.

The thickness of the film to be used thus depends on its refractive index. In order to achieve maximum destructive interference, the coefficients for the external reflections must be equal. The reflection coefficient at the film surface can be written as:

$$r_1 = \frac{n_1 - n_0}{n_1 + n_0} = \frac{1 - \frac{n_0}{n_1}}{1 + \frac{n_0}{n_1}}$$

Similarly, at the film/substrate boundary:

$$r_2 = \frac{n_s - n_1}{n_s + n_1} = \frac{1 - \frac{n_1}{n_s}}{1 + \frac{n_1}{n_s}}$$

These can only be equal if the ratios between the refractive indices are equal, i.e. if:

$$\frac{n_0}{n_1} = \frac{n_1}{n_s} \quad \text{or} \quad n_1 = \sqrt{n_0 n_s}$$

If the incident medium is taken to be air (as it often is) so that $n_0 = 1$, then for maximum destructive interference the refractive index of the film is simply the square root of the refractive index of the substrate.

While this analysis is valid, it comes with several caveats. Firstly, it only considers normally incident light; for non-normal incidence, the transmission angle plays a role in determining film thickness and must be determined using Snell's law. Secondly, this analysis neglects dispersion and so is only valid at one wavelength or a small range of wavelengths. Also important is the fact that materials with refractive indices that agree with this geometrical result are not usually available. As such, it is necessary to resort to other means in order to be able to determine reflection from thin films under different scenarios.

3.4.2. Transfer Matrix Method

While there are multiple ways to determine reflection from thin films, such as the Rouard method [50] and Transfer Matrix method [8, 49, 50], the latter is one of the more commonly used ones and details describing it can be found in many sources. The approach presented here is adopted from [49].

Consider a single thin film, homogenous and isotropic, on a substrate as depicted in Figure 3.12. A beam of light with its associated electric and magnetic fields undergoes an external reflection at (a) and the transmitted portion undergoes another reflection at (b). Multiple beams in the interference are accounted for by ensuring that E_{r1} represents the sum of all reflected beams at (a) emerging from the film, E_{i2} represents the sum of all beams incident on the film/substrate boundary at (b), etc.
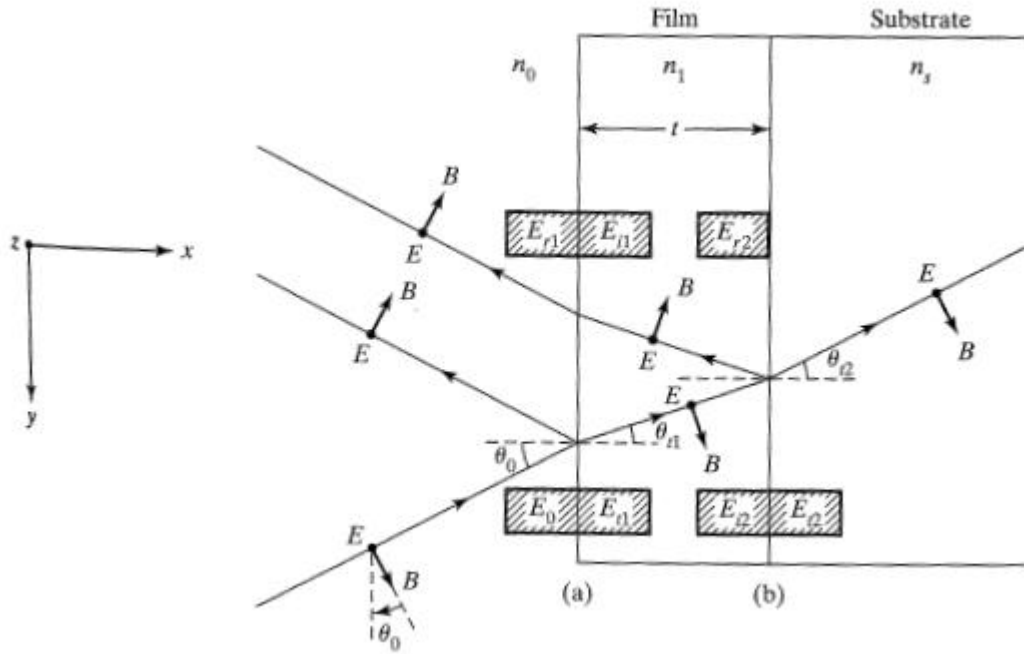
Figure 3.12: Electric and magnetic fields associated with light interfering in a thin film on a substrate. Source: [40]

As in the derivation of the Fresnel equations, the boundary conditions of the electric and magnetic fields are considered at each interface. The requirement that the components of the fields parallel to the interfaced be continuous still holds, giving:

$$E_a = E_0 + E_{r1} = E_{t1} + E_{i1} \quad (3.9)$$

$$E_b = E_{i2} + E_{r2} = E_{t2} \quad (3.10)$$

$$B_a = B_0 \cos(\theta_0) - B_{r1} \cos(\theta_0) = B_{t1} \cos(\theta_{t1}) - B_{i1} \cos(\theta_{t1}) \quad (3.11)$$

$$B_b = B_{i2} \cos(\theta_{t1}) - B_{r2} \cos(\theta_{t1}) = B_{t2} \cos(\theta_{t2}) \quad (3.12)$$

Using the generic equation relating electric fields to magnetic fields:

$$B = \left(\frac{n}{c}\right) E = n\sqrt{\varepsilon_0 \mu_0} E \quad (3.13)$$

Equations (3.11) and (3.12) can be rewritten as:

$$B_a = \gamma_0 (E_0 - E_{r1}) = \gamma_1 (E_{t1} - E_{i1}) \quad (3.14)$$

$$B_b = \gamma_1 (E_{i2} - E_{r2}) = \gamma_s E_{t2} \quad (3.15)$$

Where the following substitutions have been made:

$$\gamma_0 = n_0 \sqrt{\varepsilon_0 \mu_0} \cos(\theta_0), \ \gamma_1 = n_1 \sqrt{\varepsilon_0 \mu_0} \cos(\theta_{t1}), \ \gamma_s = n_s \sqrt{\varepsilon_0 \mu_0} \cos(\theta_{t2}) \quad (3.16)$$

E_{i2} and E_{t1} differ from the phase difference that develops from a single traversal of the film. The optical path length associated with *two* traversals of the film was presented in the previous section; the optical path length associated with *one* traversal of film is simply one-half that expression:

$$\Delta_1 = n_1 t \cos(\theta_{t1})$$

The phase difference that develops from this is the product of the optical path length with the wavenumber:

$$\delta = k_0 \Delta_1 = \left(\frac{2\pi}{\lambda_0}\right) n_1 t \cos(\theta_{t1})$$

(Note: the variable t for thickness should not be confused with the subscript t for "transmitted".)

Thus:

$$E_{i2} = E_{t1} e^{-i\delta} \quad \text{and} \quad E_{i1} = E_{r1} e^{-i\delta} \quad (3.17)$$

using similar logic for E_{i1} and E_{r2}. E_{i2} and E_{r2} in equations (3.10) and (3.15) can then be eliminated using equation (3.17):

$$E_b = E_{t1} e^{-i\delta} + E_{i1} e^{i\delta} = E_{t2} \quad (3.18)$$

$$B_b = \gamma_1 \left(E_{t1} e^{-i\delta} - E_{i1} e^{i\delta} \right) = \gamma_s E_{t2} \quad (3.19)$$

Solving for E_{t1} and E_{i1} in terms of E_a and E_b yields:

$$E_{t1} = \left(\frac{\gamma_1 E_b + B_b}{2\gamma_1}\right) e^{i\delta} \quad (3.20)$$

$$E_{i1} = \left(\frac{\gamma_1 E_b - B_b}{2\gamma_1}\right) e^{-i\delta} \quad (3.21)$$

With the help of the Euler identities for sine and cosine, equations (3.20) and (3.21) can be substituted into (3.9) and (3.14):

$$E_a = E_b \cos(\delta) + B_b \left(\frac{i \sin(\delta)}{\gamma_1}\right) \quad (3.22)$$

$$B_a = E_b \left(i\gamma_1 \sin(\delta)\right) + B_b \cos(\delta) \quad (3.23)$$

The last two equations can be written in matrix form:

$$\begin{bmatrix} E_a \\ B_a \end{bmatrix} = \begin{bmatrix} \cos(\delta) & \dfrac{i \sin(\delta)}{\gamma_1} \\ i\gamma_1 \sin(\delta) & \cos(\delta) \end{bmatrix} \begin{bmatrix} E_b \\ B_b \end{bmatrix} \quad (3.24)$$

The 2x2 matrix in (3.24) is called the transfer matrix, which is generally represented by:

$$M = \begin{bmatrix} m_{11} & m_{12} \\ m_{21} & m_{22} \end{bmatrix} \quad (3.25)$$

For a multilayer stack of N thin films, each layer is associated with its own transfer matrix. (3.24) can then be generalized as:

$$\begin{bmatrix} E_a \\ B_a \end{bmatrix} = M_1 M_2 M_3 \dots M_N \begin{bmatrix} E_b \\ B_b \end{bmatrix} \quad (3.26)$$

The product of the individual transfer matrices is an overall transfer matrix representing the entire stack in the order in which light rays encounter them:

$$M_T = M_1 M_2 M_3 \dots M_N \quad (3.27)$$

In finding the transfer matrix, parts of equations (3.9), (3.10), (3.14) and (3.15) were ignored. Those remaining equations are:

$$E_a = E_0 + E_{r1} \quad (3.28)$$

$$E_b = E_{t2} \quad (3.29)$$

$$B_a = \gamma_0 (E_0 - E_{r1}) \quad (3.30)$$

$$B_b = \gamma_s E_{t2} \quad (3.31)$$

Equations (3.28) through (3.31) can be substituted into (3.24), along with (3.25) for the generic transfer matrix, to yield:

$$\begin{bmatrix} E_0 + E_{r1} \\ \gamma_0(E_0 - E_{r1}) \end{bmatrix} = \begin{bmatrix} m_{11} & m_{12} \\ m_{21} & m_{22} \end{bmatrix} \begin{bmatrix} E_{t2} \\ \gamma_s E_{t2} \end{bmatrix} \quad (3.32)$$

The matrix system in (3.32) is equivalent to the following two equations:

$$E_0 + E_{r1} = m_{11}E_{t2} + m_{12}\gamma_s E_{t2}$$

$$\gamma_0(E_0 - E_{r1}) = m_{21}E_{t2} + m_{22}\gamma_s E_{t2}$$

Dividing these equations by E_0 and making use of the reflection and transmission coefficients defined as $r \equiv \frac{E_{r1}}{E_0}$ and $t \equiv \frac{E_{t2}}{E_0}$ results in:

$$1 + r = m_{11}t + m_{12}\gamma_s t \quad (3.33)$$

$$\gamma_0(1 - r) = m_{21}t + m_{22}\gamma_s t \quad (3.34)$$

Equations (3.33) and (3.34) can be solved simultaneously for the reflection and transmission coefficients:

$$r = \frac{\gamma_0 m_{11} + \gamma_0\gamma_s m_{12} - m_{21} - \gamma_s m_{22}}{\gamma_0 m_{11} + \gamma_0\gamma_s m_{12} + m_{21} + \gamma_s m_{22}} \quad (3.35)$$

$$t = \frac{2\gamma_0}{\gamma_0 m_{11} + \gamma_0\gamma_s m_{12} + m_{21} + \gamma_s m_{22}} \quad (3.36)$$

These coefficients, with the elements of the overall transfer matrix, can be used to determine the reflective and transmissive properties of one or many thin films represented by the matrix.

Chapter 4

Models

4.1. General Approach

The approach to setting up the single- and multi-junction models consisted of these steps:

- procuring optical data of the desired substrates and ARC materials;
- deriving and applying the needed reflection equations under various cases;
- calculating short-circuit current density, J_{sc}, and solar-weighted reflectance, SWR;
- optimizing ARC parameters to maximize J_{sc} or minimize SWR.

The following sections describe each component in detail.

4.2. Procuring Optical Data

Values of the real and complex refractive index were obtained from [48] for silicon and [51] for all other materials investigated: $Al_{0.198}Ga_{0.802}As$, Al_2O_3, GaAs, $Ga_{0.5}In_{0.5}P$, MgF_2, Si_3N_4, SiO_2, Ta_2O_5, TiO_2 and ZnS. The optical data is presented in Appendix A. The selection of ARC materials was based on those most often investigated or used in practice and for which the optical data was available in the required wavelength range.

Not much optical data for AlGaAs was available past its bandgap of 730 nm, although it was needed for up to 1,110 nm in multi-junction modeling. To overcome this obstacle, the refractive index was calculated for the required wavelengths with formulas

from [52]. In order to ensure that the calculated values remain continuous with the tabulated values, the former were shifted downwards linearly by a factor 0.062.

4.3. Calculating Reflectance

Using the transfer matrix treatment presented in chapter 3, the following reflectance equations were determined and used to calculate wavelength-dependent reflection coefficients. Derivations are presented in Appendix B.

- Single-layer ARC under normal incidence:

$$R = \frac{(n_0 - n_s)^2 + \left(\frac{n_0 n_s}{n_1} - n_1\right)^2 \tan^2(\delta)}{(n_0 + n_s)^2 + \left(\frac{n_0 n_s}{n_1} + n_1\right)^2 \tan^2(\delta)}$$

- Single-layer ARC under non-normal incidence; TE polarization:

$$R = \frac{[n_0 \cos(\theta_0) - n_s \cos(\theta_s)]^2 + \left[\frac{n_0 n_s}{n_1} \cdot \frac{\cos(\theta_0)\cos(\theta_s)}{\cos(\theta_1)} - n_1 \cos(\theta_1)\right]^2 \tan^2(\delta)}{[n_0 \cos(\theta_0) + n_s \cos(\theta_s)]^2 + \left[\frac{n_0 n_s}{n_1} \cdot \frac{\cos(\theta_0)\cos(\theta_s)}{\cos(\theta_1)} + n_1 \cos(\theta_1)\right]^2 \tan^2(\delta)}$$

- Single-layer ARC under non-normal incidence; TM polarization:

$$R = \frac{[n_0 \cos(\theta_0) - n_s \cos(\theta_s)]^2 + \left[\frac{n_0 n_s}{n_1} \cdot \cos(\theta_0)\cos(\theta_1)\cos(\theta_s) - \frac{n_1}{\cos(\theta_1)}\right]^2 \tan^2(\delta)}{[n_0 \cos(\theta_0) + n_s \cos(\theta_s)]^2 + \left[\frac{n_0 n_s}{n_1} \cdot \cos(\theta_0)\cos(\theta_1)\cos(\theta_s) + \frac{n_1}{\cos(\theta_1)}\right]^2 \tan^2(\delta)}$$

- Double-layer ARC under normal incidence:

$$R = \frac{\begin{aligned}&n_0^2\left[\cos(\delta_1)\cos(\delta_2) - \frac{n_2}{n_1}\sin(\delta_1)\sin(\delta_2)\right]^2 + (n_0 n_s)^2\left[\frac{\cos(\delta_1)\sin(\delta_2)}{n_2} + \frac{\sin(\delta_1)\cos(\delta_2)}{n_1}\right]^2\\&+[n_1\sin(\delta_1)\cos(\delta_2) + n_2\cos(\delta_1)\sin(\delta_2)]^2 + n_s^2\left[\cos(\delta_1)\cos(\delta_2) - \frac{n_1}{n_2}\sin(\delta_1)\sin(\delta_2)\right]^2 - 2n_0 n_s\end{aligned}}{\begin{aligned}&n_0^2\left[\cos(\delta_1)\cos(\delta_2) - \frac{n_2}{n_1}\sin(\delta_1)\sin(\delta_2)\right]^2 + (n_0 n_s)^2\left[\frac{\cos(\delta_1)\sin(\delta_2)}{n_2} + \frac{\sin(\delta_1)\cos(\delta_2)}{n_1}\right]^2\\&+[n_1\sin(\delta_1)\cos(\delta_2) + n_2\cos(\delta_1)\sin(\delta_2)]^2 + n_s^2\left[\cos(\delta_1)\cos(\delta_2) - \frac{n_1}{n_2}\sin(\delta_1)\sin(\delta_2)\right]^2 + 2n_0 n_s\end{aligned}}$$

- Double-layer ARC under non-normal incidence; TE polarization:

$$R = \frac{\begin{aligned} &n_0^2\cos^2(\theta_0)\left[\cos(\delta_1)\cos(\delta_2) - \frac{n_2\cos(\theta_2)}{n_1\cos(\theta_1)}\sin(\delta_1)\sin(\delta_2)\right]^2 \\ &+[n_0\cos(\theta_0)n_s\cos(\theta_s)]^2\left[\frac{\cos(\delta_1)\sin(\delta_2)}{n_2\cos(\theta_2)} + \frac{\sin(\delta_1)\cos(\delta_2)}{n_1\cos(\theta_1)}\right]^2 \\ &+[n_1\cos(\theta_1)\sin(\delta_1)\cos(\delta_2) + n_2\cos(\theta_2)\cos(\delta_1)\sin(\delta_2)]^2 \\ &+n_s^2\cos^2(\theta_s)\left[\cos(\delta_1)\cos(\delta_2) - \frac{n_1\cos(\theta_1)}{n_2\cos(\theta_2)}\sin(\delta_1)\sin(\delta_2)\right]^2 - 2n_0\cos(\theta_0)\,n_s\cos(\theta_s) \end{aligned}}{\begin{aligned} &n_0^2\cos^2(\theta_0)\left[\cos(\delta_1)\cos(\delta_2) - \frac{n_2\cos(\theta_2)}{n_1\cos(\theta_1)}\sin(\delta_1)\sin(\delta_2)\right]^2 \\ &+[n_0\cos(\theta_0)n_s\cos(\theta_s)]^2\left[\frac{\cos(\delta_1)\sin(\delta_2)}{n_2\cos(\theta_2)} + \frac{\sin(\delta_1)\cos(\delta_2)}{n_1\cos(\theta_1)}\right]^2 \\ &+[n_1\cos(\theta_1)\sin(\delta_1)\cos(\delta_2) + n_2\cos(\theta_2)\cos(\delta_1)\sin(\delta_2)]^2 \\ &+n_s^2\cos^2(\theta_s)\left[\cos(\delta_1)\cos(\delta_2) - \frac{n_1\cos(\theta_1)}{n_2\cos(\theta_2)}\sin(\delta_1)\sin(\delta_2)\right]^2 + 2n_0\cos(\theta_0)\,n_s\cos(\theta_s) \end{aligned}}$$

- Double-layer ARC under non-normal incidence; TM polarization:

$$R = \frac{\begin{aligned} &n_0^2\cos^2(\theta_0)\left[\cos(\delta_1)\cos(\delta_2) - \frac{n_2\cos(\theta_1)}{n_1\cos(\theta_2)}\sin(\delta_1)\sin(\delta_2)\right]^2 \\ &+[n_0\cos(\theta_0)n_s\cos(\theta_s)]^2\left[\frac{\cos(\theta_2)\cos(\delta_1)\sin(\delta_2)}{n_2} + \frac{\cos(\theta_1)\sin(\delta_1)\cos(\delta_2)}{n_1}\right]^2 \\ &+\left[\frac{n_1\sin(\delta_1)\cos(\delta_2)}{\cos(\theta_1)} + \frac{n_2\cos(\delta_1)\sin(\delta_2)}{\cos(\theta_2)}\right]^2 \\ &+n_s^2\cos^2(\theta_s)\left[\cos(\delta_1)\cos(\delta_2) - \frac{n_1\cos(\theta_2)}{n_2\cos(\theta_1)}\sin(\delta_1)\sin(\delta_2)\right]^2 - 2n_0\cos(\theta_0)\,n_s\cos(\theta_s) \end{aligned}}{\begin{aligned} &n_0^2\cos^2(\theta_0)\left[\cos(\delta_1)\cos(\delta_2) - \frac{n_2\cos(\theta_1)}{n_1\cos(\theta_2)}\sin(\delta_1)\sin(\delta_2)\right]^2 \\ &+[n_0\cos(\theta_0)n_s\cos(\theta_s)]^2\left[\frac{\cos(\theta_2)\cos(\delta_1)\sin(\delta_2)}{n_2} + \frac{\cos(\theta_1)\sin(\delta_1)\cos(\delta_2)}{n_1}\right]^2 \\ &+\left[\frac{n_1\sin(\delta_1)\cos(\delta_2)}{\cos(\theta_1)} + \frac{n_2\cos(\delta_1)\sin(\delta_2)}{\cos(\theta_2)}\right]^2 \\ &+n_s^2\cos^2(\theta_s)\left[\cos(\delta_1)\cos(\delta_2) - \frac{n_1\cos(\theta_2)}{n_2\cos(\theta_1)}\sin(\delta_1)\sin(\delta_2)\right]^2 + 2n_0\cos(\theta_0)\,n_s\cos(\theta_s) \end{aligned}}$$

In the double-layer coating models, δ_1 and δ_2 refer to the phase differences from a single traversal in the top film and bottom film, respectively. Whenever the incidence angle was non-zero, an average of the TE and TM reflection coefficients was calculated.

4.3.1. Textured Surface Model

For modeling reflection on planar wafers, the appropriate reflectance equations can be used directly. On textured wafers, the various angles of incidence from multiple reflections must first be calculated. In the simplest case, under normal incidence, the symmetry of the surface requires only a primary and a secondary reflection be calculated. However, a manner is needed to determine the angles light makes on all the textured facets for an arbitrary angle of incidence to the wafer, as well as an equation for total reflectance. The method employed here is based on vector geometry in which three-dimensional vectors are specified for facets and light rays, and dot products and projections are used to determine the angles of interest.

It is sensible to begin by describing the textured surface in terms of vectors. The planes that form the surface pyramids are the family of {111} planes; thus, by defining the unit vectors **i** and **j** along the diagonals of the pyramids (with **k** normal to the bulk of the substrate), the normal vector **n** of each facet can be specified, as illustrated in Figure 4.1.
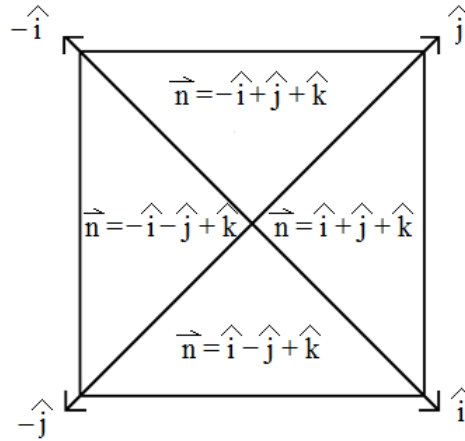
Figure 4.1: Unit vectors and normal vectors on a textured silicon surface.

In order to determine the angles of incidence of the light with each of the facets, it is necessary to parameterize the light with respect to the angle it makes with the substrate. The light ray can be defined as a vector $\mathbf{v} = -\mathbf{i} + \mathbf{j} - x*\mathbf{k}$, where x is a parameter which we must correlate to angle. The normal vector of the bulk substrate is simply $\mathbf{n} = \mathbf{k}$, since it points in the (001) direction. The angle between **v** and **n** can be determined with use the dot product:

$$\mathbf{v} \cdot \mathbf{n} = |\mathbf{v}||\mathbf{n}| \cos(\theta)$$

where $|\mathbf{v}|$ and $|\mathbf{n}|$ denote the magnitudes of vectors and θ is the angle of interest. We find that

$$\cos(\theta) = \frac{-x}{\sqrt{2 + x^2}} \quad \text{or} \quad x = \sqrt{2}\cot(\theta)$$

With the light ray vector determined for a given angle of incidence, it becomes possible to determine the angles of incidence for primary reflections. Note that the only exception to the above formula for x is when the angle of incidence is 0°; in this case, the light ray vector is simply defined as $\mathbf{v} = -\mathbf{k}$.

For secondary reflections, if the incident light ray vector is known, the angles it makes with the facets can be calculated. The following equation is used to determine the coordinates of a reflected vector:

$$\mathbf{r} = 2\frac{\mathbf{v} \cdot \mathbf{n}}{\mathbf{n} \cdot \mathbf{n}}\mathbf{n} - \mathbf{v}$$

i.e. twice the projection of $\mathbf{v}$ on $\mathbf{n}$, less $\mathbf{v}$. The dot product is then used between this vector and the normal vector of the facet of interest.

As an example, consider light normally incident to the substrate. In this case, it is clear from the symmetry of the surface that all primary reflections are 54.7° and all secondary reflections are 15.9°. If we apply the above equation to a light ray ($\mathbf{v} = -\mathbf{k}$) incident on a facet with $\mathbf{n_1} = \mathbf{i} + \mathbf{j} + \mathbf{k}$, the secondary reflection occurs on a neighbouring facet with $\mathbf{n_2} = -\mathbf{i} - \mathbf{j} + \mathbf{k}$. Thus:

$$\mathbf{r} = 2\frac{(0,0,-1) \cdot (1,1,1)}{(1,1,1) \cdot (1,1,1)}(1,1,1) - (0,0,-1) = -\frac{2}{3}\left(1,1,-\frac{1}{2}\right)$$

$$\cos(\theta) = \frac{-\frac{2}{3}\left(1,1,-\frac{1}{2}\right) \cdot (-1,-1,1)}{(1) \cdot (\sqrt{3})} = \frac{5}{\sqrt{27}} \quad \text{so} \quad \theta = 15.9°$$

as expected.

Since angles between vectors can always be calculated in the abstract, the method outlined above is incomplete. While it allows for the calculation of angles between any incoming ray of light and any pyramidal facet, it fails to address whether a given reflection actually occurs or not. Another issue is the need to determine what fraction of light rays are incident on each facet, so that every reflection term comes with a factor of how much it contributes to the total reflection. To resolve this, we begin by examining a

simpler system consisting of a uniform, periodic array of textured grooves and then expanding to a surface of textured pyramids.

4.3.1.1. 2D Model

Consider such an array of grooves as in Figure 4.2, which can be fabricated by placing a mask over the silicon wafer prior to texturing. With the assumption that light rays are incident on the surface perpendicularly to the grooves and not parallel, such a system with only two distinct facets (A and B) can be reduced to a two-dimensional problem (Figure 4.3).
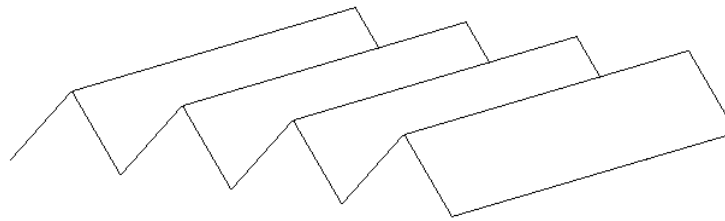
Figure 4.2: Periodic array of (111)-oriented textured grooves.
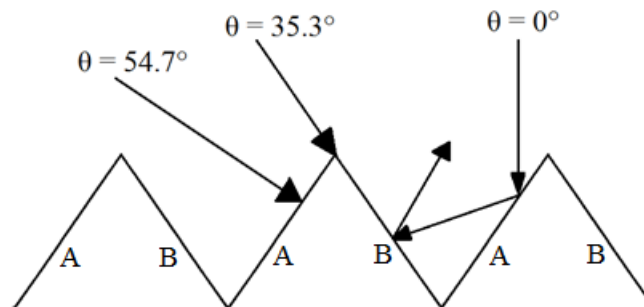
Figure 4.3: Side view of Figure 4.2.

As incoming light rays move in the direction of facet A when the incident angle is increased, it becomes more tangential to facet B; at 35.3°, it becomes perfectly tangential to it so that all reflections off of facet B no longer occur past this angle. At 54.7°, the light ray becomes normally incident to facet A and past this angle reflected light is directed away from the substrate rather than towards it. As such, secondary reflections from facet A do not occur for angles greater than 54.7°.

If we denote θ_A and θ_B to be the angles which a ray of light makes with the normal vectors of facets A and B for primary reflections, then the fraction of light falling on each facet is simply a ratio of that angle's cosine to the sum of both angles' cosines. Thus:

$$F_{A1} = \frac{\cos(\theta_A)}{\cos(\theta_A) + \cos(\theta_B)} \quad \text{and} \quad F_{B1} = \frac{\cos(\theta_B)}{\cos(\theta_A) + \cos(\theta_B)}$$

Of course, these equations are only valid up to 35.3° (where reflection from facet B vanishes), after which the factors remain constant at $F_{A1} = 1$ and $F_{B1} = 0$.

The factor F_{B2} (denoting the fractional contribution of secondary reflections from facet B that occur on a neighbouring facet A) is set to unity since any light reflected from facet B experiences a secondary reflection. The factor F_{A2} (secondary reflections from facet A) is more complicated. By inspection, all light is completely reflected on the adjacent facet (B) when the angle of incidence to the substrate is less than 19.4°. Between 19.4° and 35.3°, some light reflected from facet A is lost, while shading becomes an issue between 35.3° and 54.7°. Furthermore, as previously stated, secondary reflections no longer occur when the angle of incidence reaches 54.7°. Thus, the factor F_{A2} varies from 1 to 0 between 19.4° and 54.7°.

For an arbitrary angle of incidence 19.4° < θ < 35.3°, illustrated in Figure 4.4, any light incident on facet A between points O and N (i.e. line segment x) does not experience a secondary reflection. Therefore, the percentage of light rays that do not experience a secondary reflection is the ratio of the length of line segment x to the length of the pyramid side s. To determine this ratio, consider triangle MNO (enlarged in Figure 4.5).
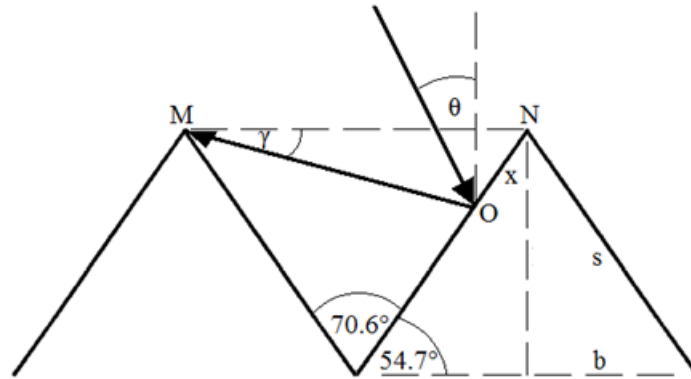
Figure 4.4: Light striking a facet at an arbitrary angle between 19.4° and 35.3°.
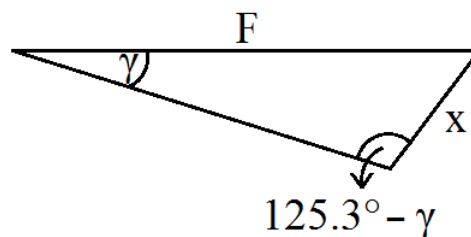
Figure 4.5: Close-up of triangle MNO in Figure 4.4.

Line segment F that connects two pyramid peaks is twice the length of line segment b, which is related to the length of the pyramid side by $s = \sec(54.7°) * b = \sqrt{3}b$. Hence, $F = \frac{2}{\sqrt{3}}s$. Angle γ is related to the angle of incidence by $\gamma = \theta - 19.4°$. From the law of sines:

$$\frac{\sin(\gamma)}{x} = \frac{\sin(125.3° - \gamma)}{\frac{2}{\sqrt{3}}s} \qquad so \qquad \frac{x}{s} = \frac{\frac{2}{\sqrt{3}}\sin(\gamma)}{\sin(125.3° - \gamma)}$$

and F_{A2} is simply $1 - \frac{x}{s}$ in this range.

For angles of incidence $35.3° < \theta < 54.7°$, illustrated in Figure 4.6, part of facet A between points Q and R (i.e. line segment x') will be inaccessible to a certain percentage of light rays due to shading, which further reduces F_{A2}. This percentage is the ratio of the length of line segment x' to the length of the pyramid side s. To determine this ratio, consider triangle PQR (enlarged in Figure 4.7).
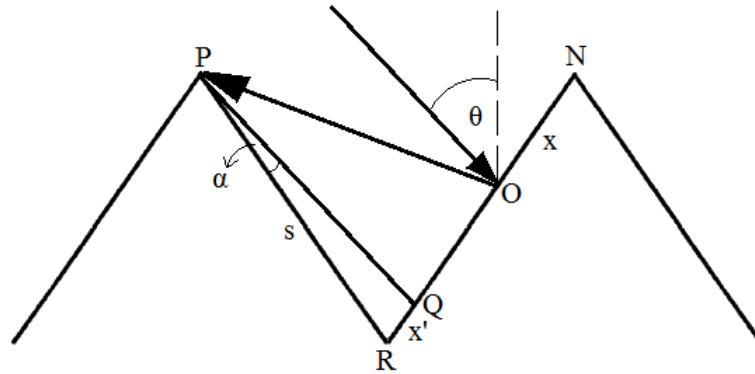
Figure 4.6: Light striking a facet at an arbitrary angle between 35.3° and 54.7°.
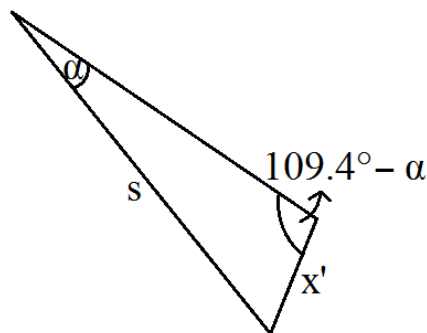
Figure 4.7: Close-up of triangle PQR in Figure 4.6.

Angle α is related to the angle of incidence by $\gamma = \theta - 35.3°$. Again, from the law of sines:

$$\frac{\sin(\alpha)}{x'} = \frac{\sin(109.4° - \alpha)}{s} \quad \text{so} \quad \frac{x'}{s} = \frac{\sin(\alpha)}{\sin(109.4° - \alpha)}$$

and F_{A2} is defined as $1 - \frac{x}{s} - \frac{x'}{s}$ in this range. Hence, for all angles (after substituting θ for γ and α):

$$F_{A2} = \begin{cases} 1 & \theta \leq 19.4° \\[2ex] 1 - \dfrac{\dfrac{2}{\sqrt{3}}\sin(\theta - 19.4°)}{\sin(144.7° - \theta)} & 19.4° \leq \theta \leq 35.3° \\[3ex] 1 - \dfrac{\dfrac{2}{\sqrt{3}}\sin(\theta - 19.4°) + \sin(\theta - 35.3°)}{\sin(144.7° - \theta)} & 35.3° \leq \theta \leq 54.7° \\[2ex] 0 & \theta \geq 54.7° \end{cases}$$

This is displayed graphically in Figure 4.8 below.
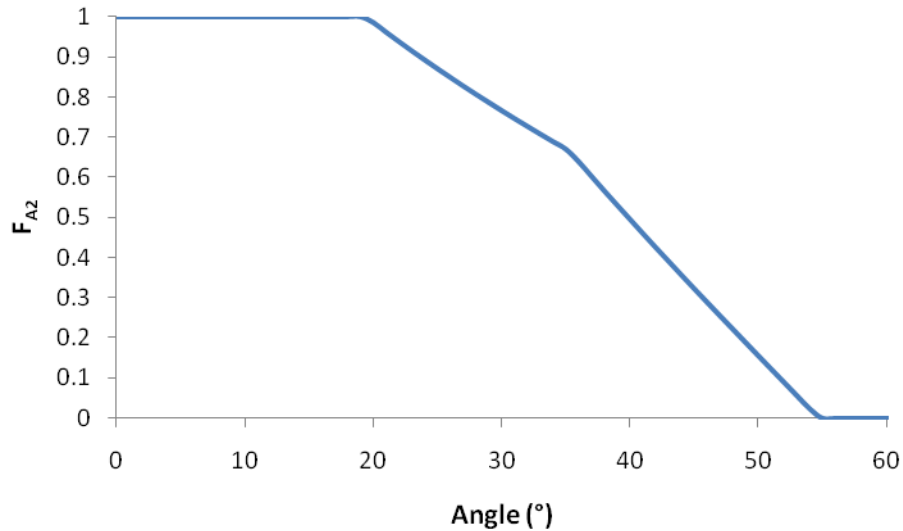
Figure 4.8: Variation of F_{A2} vs. incident angle.

Taking all individual reflections and their contributing factors together, the resulting equation for total reflectance comes to:

$$R_T = R_{A1}*F_{A1}*[R_{A2}*F_{A2} + (1-F_{A2})] + R_{B1}*F_{B1}*R_{B2}$$

where:

- R_{A1} and R_{B1} are the primary reflection coefficients from facets A and B;
- F_{A1} and F_{B1} are the contribution factors of R_{A1} and R_{B1};
- R_{A2} is the secondary reflection coefficient from facet A (occurs on facet B);
- F_{A2} is the contribution factor of R_{A1};
- $(1-F_{A2})$ accounts for light not subjected to a secondary reflection from facet A;
- R_{B2} is the secondary reflection coefficient from facet B (occurs on facet A).

4.3.1.2. 3D Model

In extending this analysis of grooves to pyramids – essentially moving from a 2D problem to a 3D problem – some assumptions must be made regarding the surface. As before, the features are taken to be uniform in size and periodic. For simplicity, a further assumption will be made: that the pyramids are aligned as in Figure 4.9.
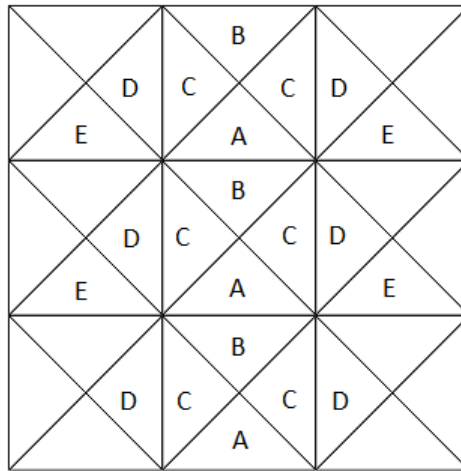
Figure 4.9: "Aligned" arrangement of pyramids.

While there are only four distinct pyramid facets, they are given five labels – A to E. The reason for this is the way the direction from which incident light on the substrate is defined: for non-normal incidence, light comes from the direction of facet A and away from facet B. This means that reflections from the facets beside A and B will be symmetrical (hence both sides are labelled C) but opposite in direction and will have secondary reflections with two different groups of facets, labelled D and E.

As in the previous model, if we denote θ_A, θ_B and θ_C to be the angles which a ray of light makes with the normal vectors of facets A, B and C, respectively, then the fraction of light falling on each facet is a ratio of that angle's cosine to the sum of the other angles' cosines. For example, for facet A:

$$F_{A1} = \frac{\cos(\theta_A)}{\cos(\theta_A) + \cos(\theta_B) + 2 * \cos(\theta_C)}$$

with factors F_{B1} and F_C calculated the same way. (The multiple of 2 in the denominator accounts for the two C facets on either side of A and B.) Since reflection from facet B vanishes at 35.3° as before, these equations are only valid for angles of incidence up to that point. The factors remain constant after that with $F_{A1} = 0.5$, $F_{B1} = 0$ and $F_C = 0.25$. It may appear at first that F_{A1} should continue to increase and F_C should continue to decrease past 35.3°; however, as illustrated in Figure 4.10, this is prevented by the fact that part of facet A becomes hidden due to shading from the pyramid in front of it.
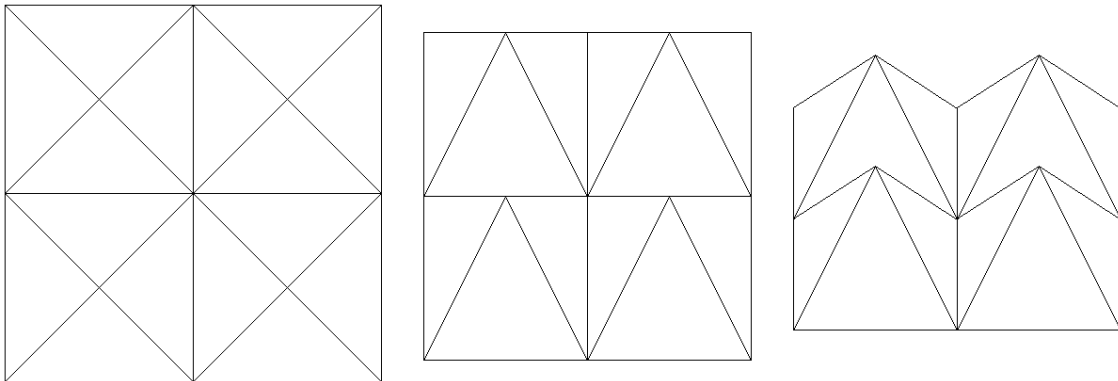
Figure 4.10: Textured surface viewed at normal incidence (left), 35.3° (middle) and > 35.3° (right).

The alignment of the pyramids results in secondary reflections from facets A and B being identical to those in the textured grooves model, meaning factors F_{A2} and F_{B2} are identical to the ones in that model as well. Light reflected off of facet C will be directed to facets D and E. For these secondary reflections, towards which facet a reflected ray is directed depends where on facet C it was incident. For an exact expression, this requires ray tracing software. Nevertheless, an approximation of the fraction of rays falling incident on each facet can be sought. If we consider that at normal incidence all reflected light is directed to facet D and that as the incident angle is increased more light becomes directed towards facet E, then F_D can vary from 1 to 0 for $0° < \theta < 90°$ while F_E varies from 0 to 1. As a first-order approximation, this transition can be linear such that:

$$F_D = 1 - \frac{\theta}{90°} \quad \text{and} \quad F_E = 1 - F_D = \frac{\theta}{90°}$$

Taking all individual reflections and their factors together, the resulting equation for total reflectance on a textured surface comes to:

$$R_T = R_{A1}*F_{A1}*[R_{A2}*F_{A2} + (1-F_{A2})] + R_{B1}*F_{B1}*R_{B2} + 2*R_C*F_C*[R_D*F_D+R_E*F_E]$$

where:

- R_{A1} and R_{B1} are the primary reflection coefficients from facets A and B;
- F_{A1} and F_{B1} are the contribution factors of R_{A1} and R_{B1};
- R_{A2} is the secondary reflection coefficient from facet A (occurs on facet B);
- F_{A2} is the contribution factor of R_{A1};
- $(1-F_{A2})$ accounts for light not subjected to a secondary reflection from facet A;
- R_{B2} is the secondary reflection coefficient from facet B (occurs on facet A);
- R_C, R_D and R_E are the reflection coefficients from facets C, D and E;
- F_C, F_D and F_E are the contribution factors of R_C, R_D and R_E.

4.3.1.3. Discussion of Models

Both models neglect to take tertiary reflections into account, but this has a minor effect on the overall accuracy because they do not occur often. In the 3D textured surface model, it was assumed that the pyramids were all aligned as in Figure 4.9. This is not the case in reality, as can be seen in the SEM image of Figure 2.6 (reproduced below); however, trying to model a more realistic morphology like the "staggered" arrangement in Figure 4.11 is much too complicated analytically and requires ray tracing software.
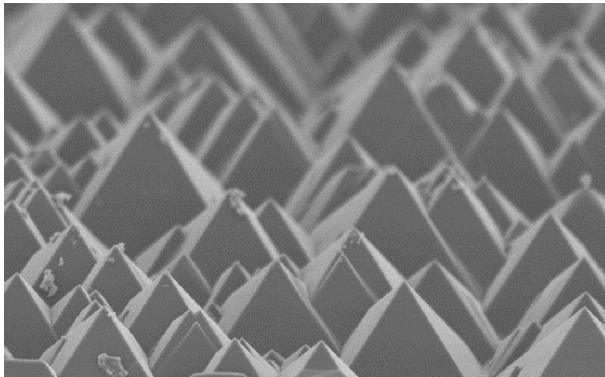
Figure 2.6: SEM cross-section image of textured (100)-oriented silicon. Source: [28]
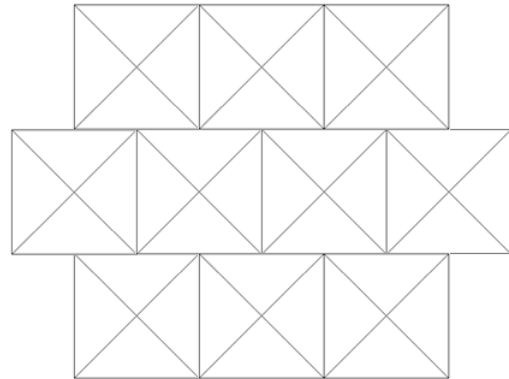
Figure 4.11: "Staggered" arrangement of pyramids.

Nevertheless, while the 2D textured surface model may be a closer approximation to its physical counterpart than the 3D textured surface model, the latter is still a fair representation of reality. Its validation is presented by comparing it to experimental results. The two figures below are graphs of total reflectance as a function of incidence angle for silicon wafers with different surface treatments. Reflectance curves in Figure 4.12 result from applying the equations discussed, while those in Figure 4.13 are a result of prepared samples measured with a variable angle reflectometer [53]. The reflectance from the 3D textured surface model shows good agreement with that measured from experiment, suggesting that the model is fairly reliable. The reflectance from the 2D textured surface model is quite different from the measured reflectance. As such, the 3D textured surface model is chosen for the optimization of ARCs.
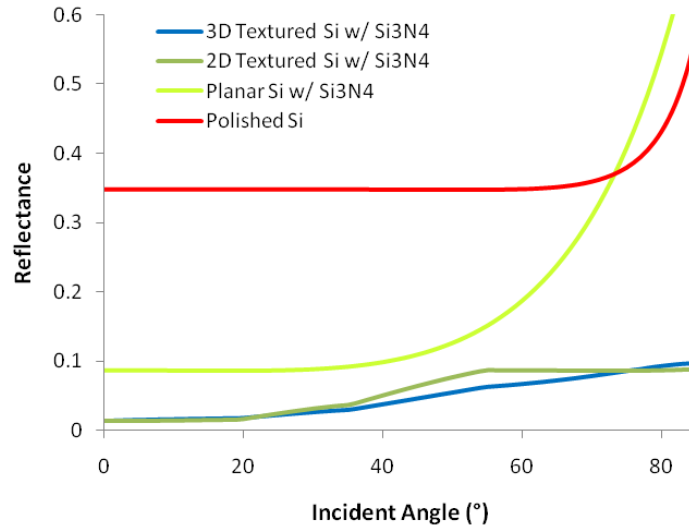
Figure 4.12: Calculated reflectance vs. angle for several non-optimized surface treatments at $\lambda = 630$ nm.
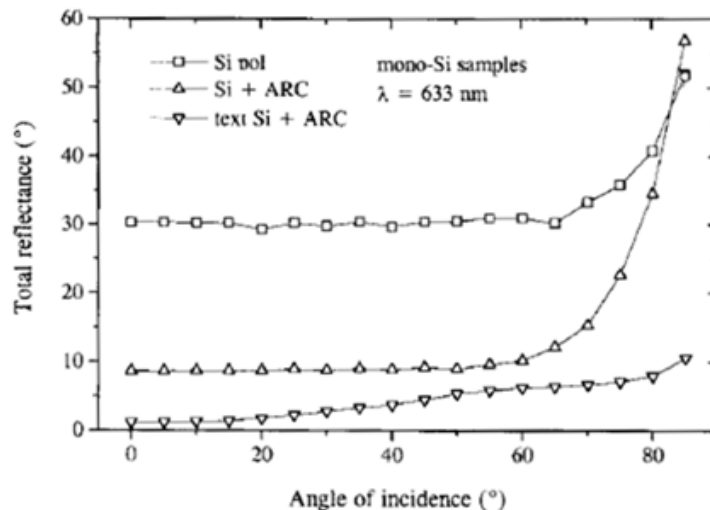
Figure 4.13: Measured reflectance vs. angle for several non-optimized surface treatments. Source: [53]

4.3.2. Thin Semiconductor Layer

The single-junction models consisted of a structure of {air, ARC(s), substrate}, even for the GaInP window layer in some of the GaAs models. The multi-junction models consisted of a structure of {air, ARC(s), top subcell, bottom subcell}, the top subcell being GaAs or AlGaAs and the bottom subcell being Si. Since the thicknesses of the top subcells in the multi-junction models are on the order of the wavelength of light, a question arises as to whether they should be treated as thin films for the purpose of calculating reflectance. It might seem so at first, but the theory for thin films presented in chapter 3 assumes that the materials are optically transparent, whereas the semiconductors clearly are not. The reflectance equation for a single-layer thin film can be modified to account for absorption:

$$R = \frac{(n_0 - n_s)^2 \left[1 + \tan^2(\delta)\tanh^2\left(\frac{\alpha t}{2}\right)\right] + 2(n_0 - n_s)\left(\frac{n_0 n_s}{n_1} - n_1\right)\tanh\left(\frac{\alpha t}{2}\right)\left[1 + \tan^2(\delta)\right] + \left(\frac{n_0 n_s}{n_1} - n_1\right)^2\left[\tanh^2\left(\frac{\alpha t}{2}\right) + \tan^2(\delta)\right]}{(n_0 + n_s)^2 \left[1 + \tan^2(\delta)\tanh^2\left(\frac{\alpha t}{2}\right)\right] + 2(n_0 + n_s)\left(\frac{n_0 n_s}{n_1} + n_1\right)\tanh\left(\frac{\alpha t}{2}\right)\left[1 + \tan^2(\delta)\right] + \left(\frac{n_0 n_s}{n_1} + n_1\right)^2\left[\tanh^2\left(\frac{\alpha t}{2}\right) + \tan^2(\delta)\right]}$$

where t is the thickness of the film and α is the absorption coefficient. (A derivation is presented in Appendix B.) Applying this equation to GaAs and AlGaAs shows that the results do not differ much from treating the thin semiconductors as bulk material. For example, a comparison of the thin-film-GaAs on Si reflectance and GaAs bulk reflectance is shown on the following page for thicknesses of 1.0 μm and 0.4 μm. In either case, the two curves overlap nearly perfectly with most of the discrepancy occurring in wavelengths past the bandgap of GaAs (where the extinction coefficient becomes zero). Thus, top subcells can be treated as bulk material instead of thin films, which greatly simplifies the models.
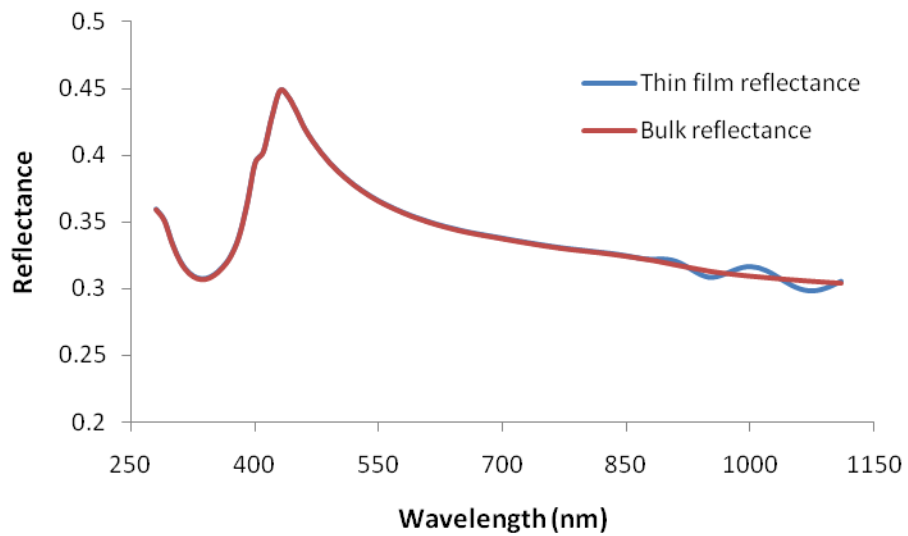
Figure 4.14: Reflectance vs. wavelength for 1.0-μm thick GaAs on silicon treated as a thin film and as bulk.
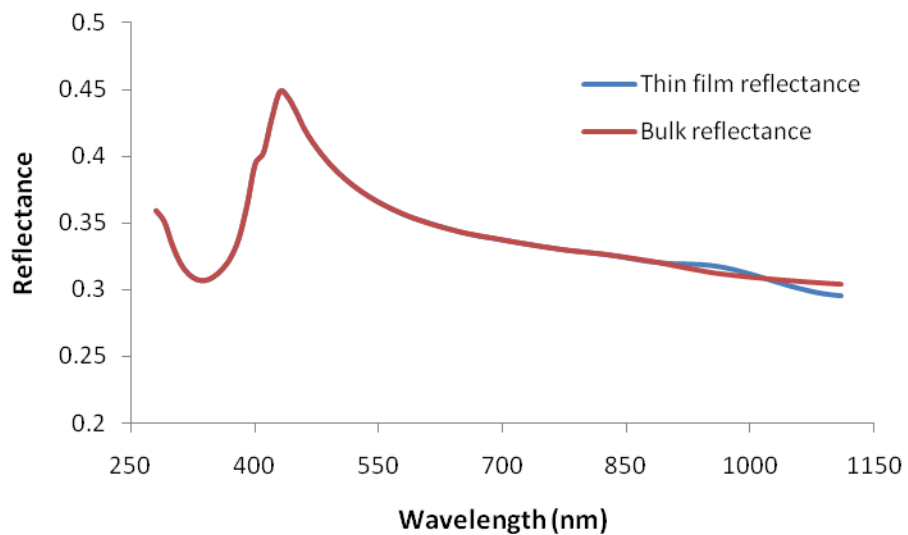
Figure 4.15: Reflectance vs. wavelength for 0.4-μm thick GaAs on silicon treated as a thin film and as bulk.

4.4. Calculating J_{sc} and SWR

4.4.1. Normal Incidence

The most general form of the equation for short-circuit current density is an integral comprising an incident spectrum $F(\lambda)$, internal quantum efficiency $IQE(\lambda)$, absorption coefficient $a(\lambda)$ and transmission coefficient written as $1 - R(\lambda)$:

$$J_{sc} = q \int_0^\infty F(\lambda)IQE(\lambda)a(\lambda)[1 - R(\lambda)]d\lambda$$

where q is the elementary charge of an electron. The limits of integration are modified to finite non-zero values because the atmosphere blocks UV and other short-wavelength light and semiconductors are transparent to photons with energy lower than their bandgap. Furthermore, thick substrates result in near-unity absorption up to the bandgap so that the absorption coefficient resembles a step function:

$$\lim_{t \to \infty} a(\lambda) = \lim_{t \to \infty}\left[1 - e^{-\alpha(\lambda)t}\right] = \begin{cases} 1 \text{ for } \lambda < \lambda_g \\ 0 \text{ for } \lambda < \lambda_g \end{cases}$$

Thus, the short-circuit current density for (infinitely) thick single-junction solar cells is:

$$J_{sc} = q \int_{\lambda_{min}}^{\lambda_g} F(\lambda)IQE(\lambda)[1 - R(\lambda)]d\lambda$$

The objective of ARC design, of course, is to maximize the current density. Another useful parameter in optimizing ARC design is the solar-weighted reflectance, SWR, defined as [18]:

$$SWR = \frac{\int F(\lambda)IQE(\lambda)R(\lambda)d\lambda}{\int F(\lambda)IQE(\lambda)d\lambda}$$

It is essentially a ratio of the number of useable photons lost to reflection over the total number of useable photons ("useable" meaning able to generate carriers). Minimizing the SWR is equivalent to maximizing the current density, which becomes clear when the equation is manipulated and expressed as the following [15, 18]:

$$SWR = 1 - \frac{J_{sc}}{J_{sc0}}$$

where J_{sc0} is the current density under zero reflection (the maximum possible current density).

In multi-junction solar cells, the short-circuit current density equation varies for each subcell as its optical performance is dependent on the subcells above it. For the top subcell of finite thickness in a double-junction solar cell:

$$J_{sc1} = q \int_{\lambda_{min}}^{\lambda_{g1}} F(\lambda)IQE_1(\lambda)a_1(\lambda)[1 - R_1(\lambda)]d\lambda$$

For the bottom subcell, assumed to be infinitely thick:

$$J_{sc2} = q \int_{\lambda_{min}}^{\lambda_{g2}} F(\lambda)IQE_2(\lambda)[1 - a_1(\lambda)][1 - R_1(\lambda)][1 - R_2(\lambda)]d\lambda$$

where the subscripts 1 and 2 are used to differentiate between the top and bottom subcells. Due to the current-matching requirement in multi-junction solar cells, the current density of the device is the lesser of those generated by each subcell:

$$J_{sc} = \min(J_{sc1}, J_{sc2})$$

The term $[1 - R_2(\lambda)]$ accounts for reflection at the interface between the subcells but the equations do not consider that some of the light reflected back into the top subcell would be absorbed. The semiconductors considered (AlGaAs, GaAs and Si) are very close in refractive index, however, so this reflection is very low (less than 1% on average) and the omission is negligible.

4.4.2. Angle-Averaged Incidence

Non-normal incidence does more than affect the reflection coefficient; it also decreases the light intensity per unit area. As shown in Figure 4.16, light incident on a surface at an angle θ to the normal spreads out so that the effective area is reduced by a factor of $\cos(\theta)$. The current density diminishes accordingly, becoming $J_{sc}(\theta)\cos(\theta)$.
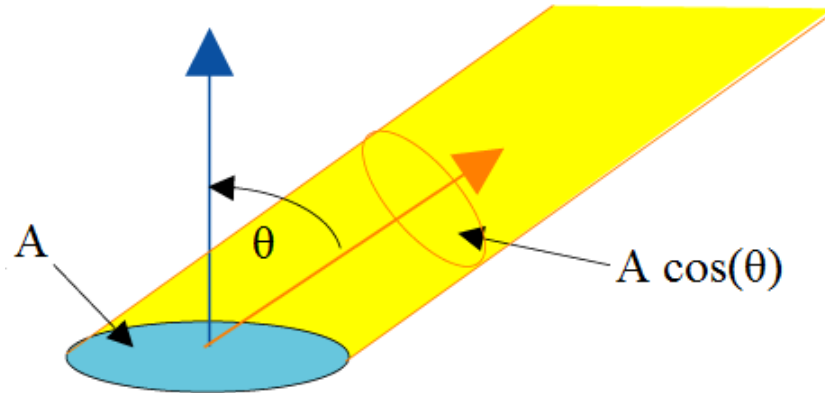
Figure 4.16: Non-normal incidence leading to a reduced effective area. Modified from [54]

A question arises as to whether there is much difference in ARC optimization between solar cells that track the Sun (perpetual normal incidence) and those that are fixed in orientation (perpetual variance of incidence). To determine this, the contribution of current density from all daylight hours must be considered. On an equinoctial day (i.e. the vernal equinox or autumnal equinox) and for a solar cell orientated facing the equator tilted at latitude, the apparent motion of the Sun from sunrise to sunset is a semicircle directly overhead the solar cell. If the Sun is said to have an apparent angular speed ω, then:

$$\omega = \frac{d\theta}{dt} \quad or \quad d\theta = \omega dt$$

hence a calculation for current density over time is equivalent to one over angles. Integrating the product of the current density with a cosine and dividing by the integral of said cosine gives the angle-averaged current density weighted over the length of an equinoctial day:

$$J_{sc,ave} = \frac{\int J_{sc}(\theta)\cos(\theta)\, d\theta}{\int \cos(\theta)\, d\theta}$$

Thus, the cosine in the numerator accounts for the Sun's path as well as the reduction in light intensity. The SWR parameter can be applied here as well, although it is expected to be noticeably higher than for normal incidence.

4.5. Other Notes

The short-circuit current densities were calculated using trapezoidal integration steps of 10 nm starting at λ_{min} = 280 nm. Angle-averaging of current density was calculated in steps of 1° from 0° to 90°. AM1.5D was chosen for the incident solar spectrum; its values were obtained from [45] and converted to the appropriate units. For simplicity, the modeled solar cells were assumed to have ideal internal quantum efficiencies rather than realistic ones in order for the results to be general and not device-specific. (However, the models can be modified fairly easily to include non-ideal IQE.) The IQE was thus treated as a step function for each substrate:

$$IQE(\lambda) = \begin{cases} 1 \text{ for } \lambda < \lambda_g \\ 0 \text{ for } \lambda > \lambda_g \end{cases}$$

For completeness, theoretical efficiency was also calculated as a measure of performance. Open circuit voltages were determined by Dr. Kleiman for both the single- and multi-junction models by calculating the maximum amount of work done per absorbed photon, as described in [55]. Fill factors were calculated according to the following equation from [56]:

$$FF = \frac{V_{oc} - \frac{kT}{q} \ln\left(\frac{qV_{oc}}{kT} + 0.72\right)}{V_{oc} + \frac{kT}{q}}$$

where k is Boltzmann's constant and T is temperature set at 300 K. Efficiency was then calculated as presented in section 3.2.1., namely:

$$\eta = \frac{FF \cdot J_{sc} \cdot V_{oc}}{P_{in}}$$

Chapter 5

Results

5.1. Single-Junction Models

5.1.1. Silicon Cell

5.1.1.1. Normal incidence

Table 5.1 summarizes the results from modeling various ARCs on planar and textured silicon under normal incidence. Optimal thicknesses for the coatings are listed accompanied by their corresponding current density and solar-weighted reflectance. The maximum attainable short circuit current density (i.e. under zero reflection) for silicon is 39.046 mA/cm^2 under the AM1.5D spectrum.

	Planar Surface			Textured Surface		
ARC	t (nm)	J_{sc} (mA/cm^2)	SWR (%)	t (nm)	J_{sc} (mA/cm^2)	SWR (%)
None	-	25.467	34.78	-	34.267	12.24
Al_2O_3	92	35.467	9.17	91	38.005	2.67
Si_3N_4	80	35.654	8.69	78	37.874	3.00
SiO_2	112	33.434	14.37	117	37.770	3.27
TiO_2	62	34.154	12.53	62	37.174	4.79
Al_2O_3/TiO_2	82 / 52	37.075	5.05	89 / 55	38.500	1.40
MgF_2/ZnS	113 / 58	37.875	3.00	134 / 51	38.807	0.61

Table 5.1: Optimized results for planar and textured silicon under normal incidence.

Figure 5.1 is a graph of SWR as a function of ARC thickness on both planar and textured silicon for Si_3N_4 and SiO_2. Out of the four single-layer ARCs, Si_3N_4 demonstrates the best performance on a planar surface and SiO_2 the worst. On a textured surface, however, Si_3N_4 no longer has the best performance and SiO_2 no longer has the worst. Furthermore, SiO_2 benefits greatly from texturing, which can be seen in the figure from the fact that the gap between its two curves is much greater than that of Si_3N_4. The SWR for SiO_2 reduces the most among all materials when comparing that for a planar surface to that of a textured surface.
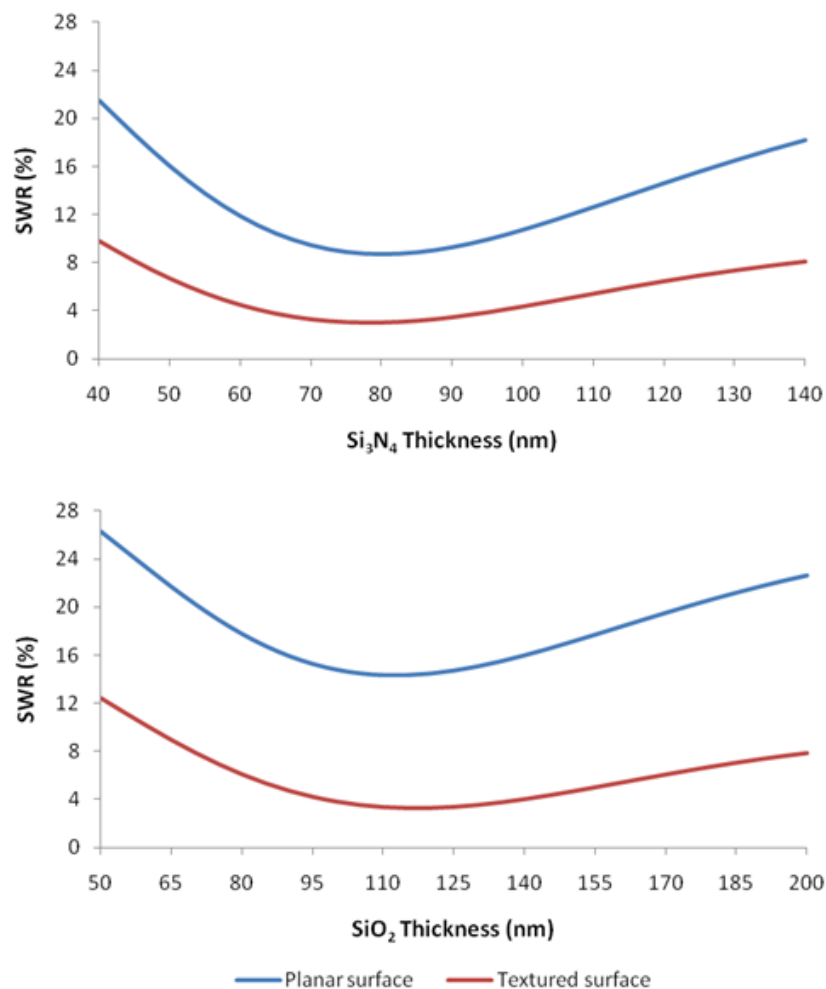
Figure 5.1: Normal incidence SWR of Si_3N_4-coated (top) and SiO_2-coated (bottom) planar and textured silicon.

In comparing the optimal thicknesses for the single-layer ARCs between planar and textured surfaces, it appears there is very little difference – only a few nanometres, the most being 5 nm for SiO_2.

Figures 5.2 and 5.3 are contour plots and overlapping surface plots of SWR as a function of both thicknesses in the double-layer ARC combinations. From Table 5.1, it is evident that the MgF_2/ZnS combination outperforms Al_2O_3/TiO_2 in both the planar and textured cases as it has a SWR of about half the other. Furthermore, 0.61% reflectance indicates that almost all light is captured and transmitted into the cell when MgF_2/ZnS is deposited on a textured surface.

In the Al_2O_3/TiO_2 combination, there is little difference in the optimal thicknesses between planar and textured surfaces, just 7 nm in the Al_2O_3 in the top layer and 3 nm in the bottom layer. In the MgF_2/ZnS combination, however, there is a fairly large difference in the optimal thicknesses as the contour seems to warp somewhat (Figure 5.3). The previous global minimum becomes a local minimum and the new global minimum has shifted in both axes to result in an increase of 21 nm in top layer and a decrease of 7 nm in bottom layer.

Table 5.2 shows the theoretical solar cell efficiencies associated with the current densities for each optimized scenario. Open-circuit voltage V_{oc} was set at 0.8105 V, resulting in a fill factor of 0.8613 as per the equation in section 4.5. The data in the table indicates that, under normal incidence, a single-layer ARC on a textured surface is comparable in performance to a double-layer ARC on a planar surface. Not surprisingly, the efficiency of a MgF_2/ZnS-coated textured surface approaches the detailed balance limit for silicon.

	Planar Surface		Textured Surface	
	J_{sc} (mA/cm^2)	η (%)	J_{sc} (mA/cm^2)	η (%)
None	25.467	19.75	34.267	26.58
Al_2O_3	35.467	27.51	38.005	29.47
Si_3N_4	35.654	27.65	37.874	29.37
SiO_2	33.434	25.93	37.770	29.29
TiO_2	34.154	26.49	37.174	28.83
Al_2O_3/TiO_2	37.075	28.75	38.500	29.86
MgF_2/ZnS	37.875	29.37	38.807	30.10

Table 5.2: Optimized J_{sc} and theoretical efficiencies of planar and textured silicon under normal incidence.

Figure 5.2: Contour and surface plots of normal incidence SWR for Al_2O_3/TiO_2-coated planar and textured silicon.

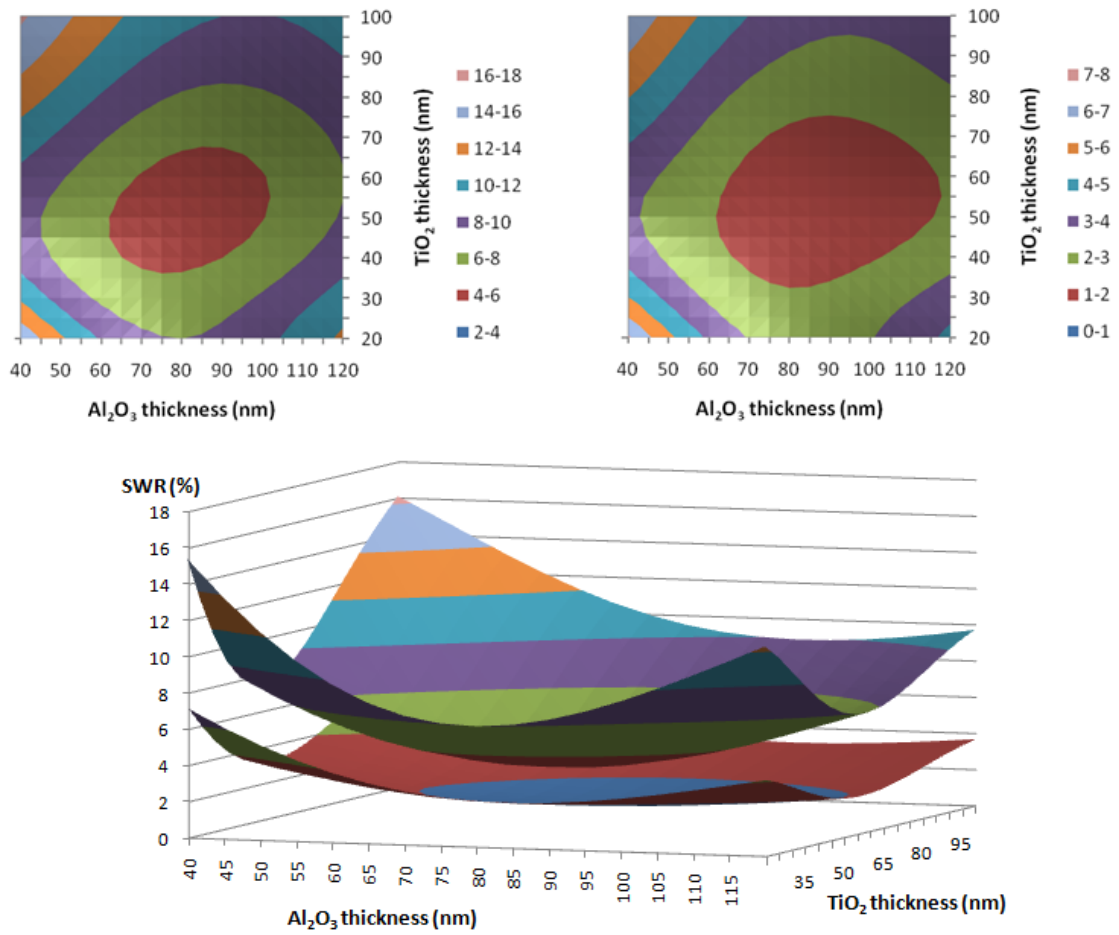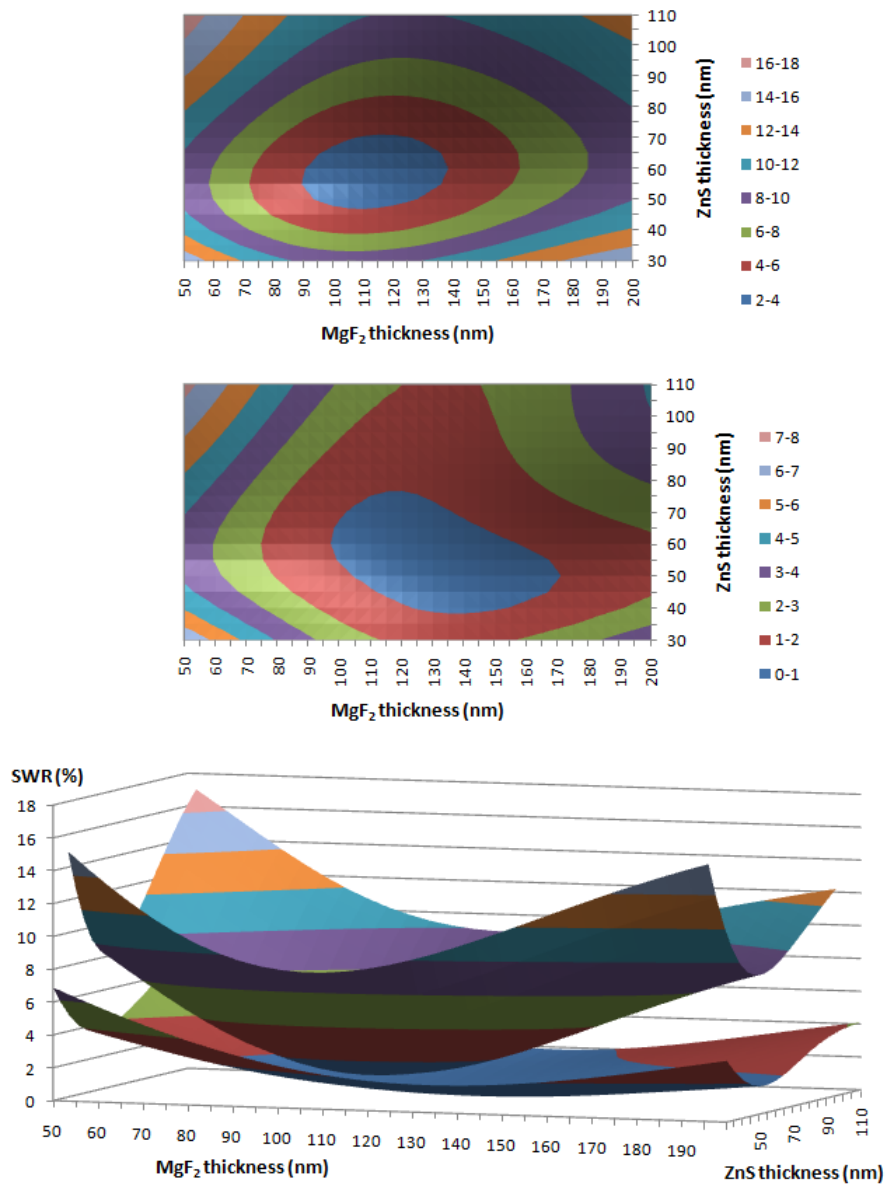Figure 5.3: Contour and surface plots of normal incidence SWR for MgF_2/ZnS-coated planar and textured silicon.

5.1.1.2. Angle-averaged incidence

Table 5.3 summarizes the results from modeling various ARCs on planar and textured silicon for angle-averaged incidence. Figure 5.4 is a graph of SWR versus ARC thickness on both planar and textured silicon for Si_3N_4 and SiO_2, akin to Figure 5.1.

Predictably, the SWRs are higher than for normal incidence due to low current density contribution from higher angles. The relative performance of the single-layer coatings on a planar surface is the same as for normal incidence on a textured surface: Al_2O_3 offers the lowest SWR followed by Si_3N_4, SiO_2 and TiO_2. An unexpected result is found in the textured surface case in that SiO_2, once the worst-performing of the four single-layer coatings, becomes the best and is the only one with a SWR less than 5%. There is a little more difference in the optimal thicknesses between planar and textured surface compared to under normal incidence, but it remains less than 10 nm.

Figures 5.5 and 5.6 are contour plots and overlapping surface plots of SWR as a function of both thicknesses in the double-layer ARC combinations, just as Figures 5.2 and 5.3. MgF_2/ZnS again outperforms Al_2O_3/TiO_2 for both planar and textured surfaces, but especially so for the latter. The Al_2O_3/TiO_2 combination is actually *worse* on a textured surface than most of the single-layer ARCs with the exception of TiO_2 by itself. Figure 5.7 shows how the current density varies with angle on a textured surface for optimized MgF_2/ZnS, Al_2O_3/TiO_2 and SiO_2. It is clear that while Al_2O_3/TiO_2 works fairly well at normal incidence, it performs consistently worse as the angle increases.

As was for normal incidence, in the Al_2O_3/TiO_2 combination there is little difference in the optimal thicknesses between planar and textured surfaces. For MgF_2/ZnS, there is a mild difference (8 nm) in the optimal thickness of the top layer.

Table 5.4 shows the theoretical solar cell efficiencies associated with the current densities for each optimized angle-averaged scenario.

	Planar Surface			Textured Surface		
ARC	t (nm)	J_{sc} (mA/cm^2)	SWR (%)	t (nm)	J_{sc} (mA/cm^2)	SWR (%)
None	-	25.293	35.22	-	32.348	17.15
Al_2O_3	99	33.174	15.04	95	36.997	5.25
Si_3N_4	84	32.615	16.47	81	36.770	5.83
SiO_2	127	32.204	17.52	118	37.349	4.35
TiO_2	64	30.215	22.62	63	35.530	9.00
Al_2O_3/TiO_2	91 / 49	33.753	13.56	89 / 49	36.512	6.49
MgF_2/ZnS	129 / 58	35.834	8.23	121 / 56	38.391	1.68

Table 5.3: Optimized results for planar and textured silicon under angle-averaged incidence.
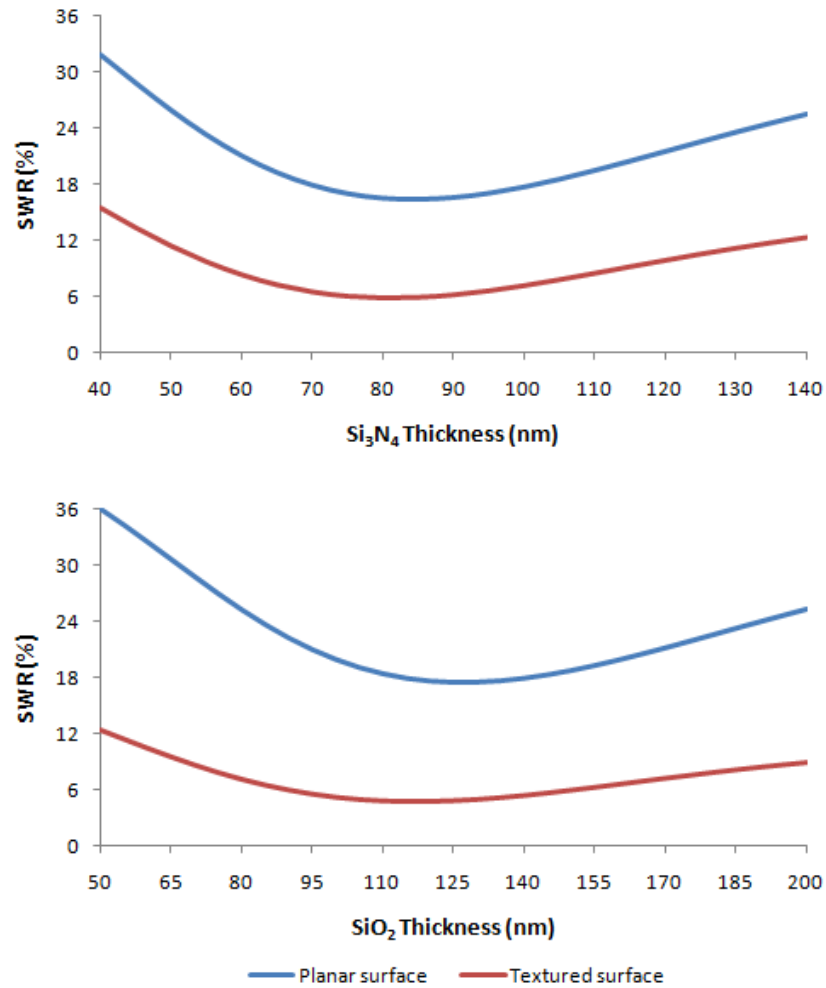
Figure 5.4: Angle-averaged incidence SWR of Si_3N_4-coated (top) and SiO_2-coated (bottom) planar and textured silicon.

	Planar Surface		Textured Surface	
	J_{sc} (mA/cm^2)	η (%)	J_{sc} (mA/cm^2)	η (%)
None	25.293	19.62	32.348	25.09
Al_2O_3	33.174	25.73	36.997	28.69
Si_3N_4	32.615	25.29	36.770	28.52
SiO_2	32.204	24.98	37.349	28.97
TiO_2	30.215	23.43	35.530	27.55
Al_2O_3/TiO_2	33.753	26.18	36.512	28.32
MgF_2/ZnS	35.834	27.79	38.391	29.77

Table 5.4: Optimized J_{sc} and theoretical efficiencies of planar and textured silicon under angle-averaged incidence.
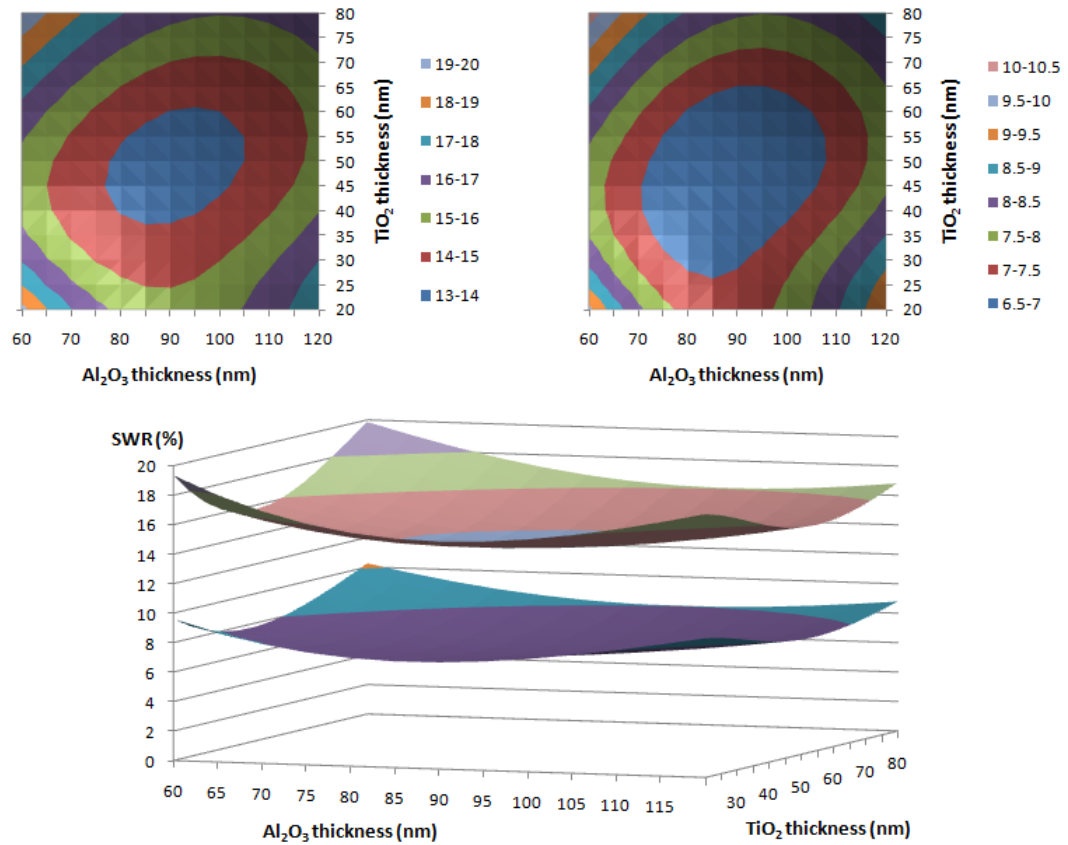
Figure 5.5: Contour and surface plots of angle-averaged incidence SWR for Al_2O_3/TiO_2-coated planar and textured silicon.
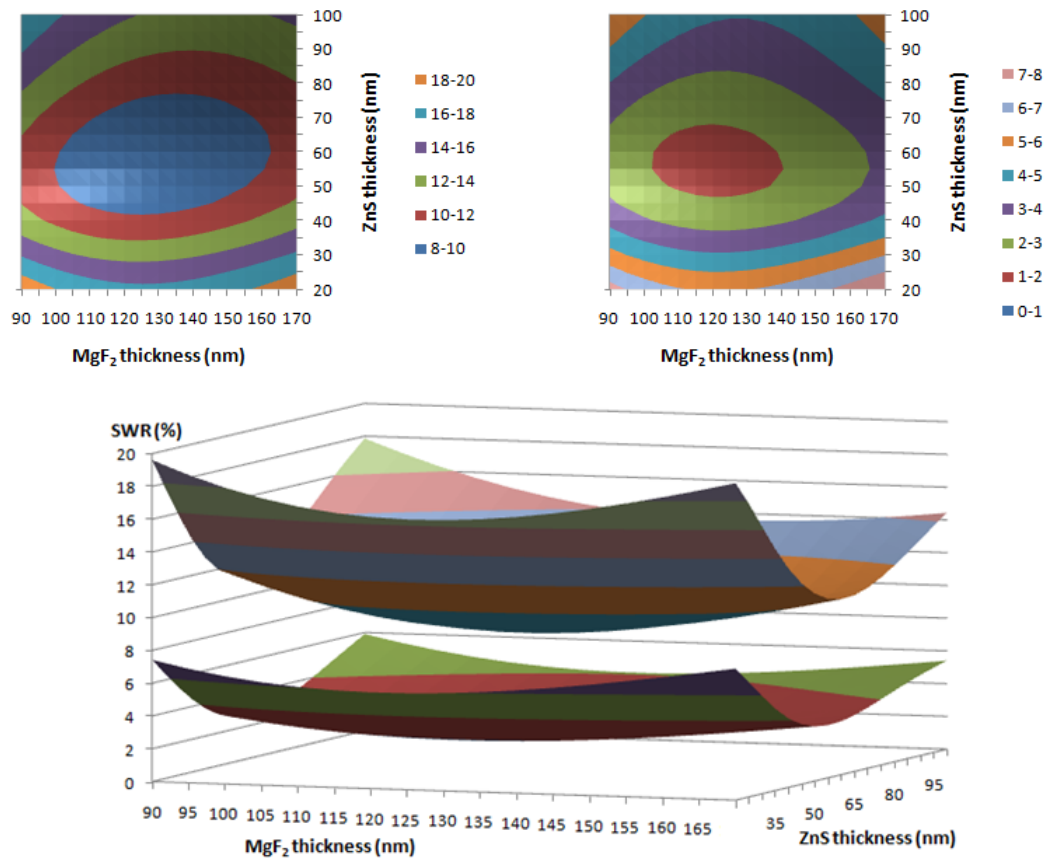
Figure 5.6: Contour and surface plots of angle-averaged incidence SWR for MgF$_2$/ZnS-coated planar and textured silicon.
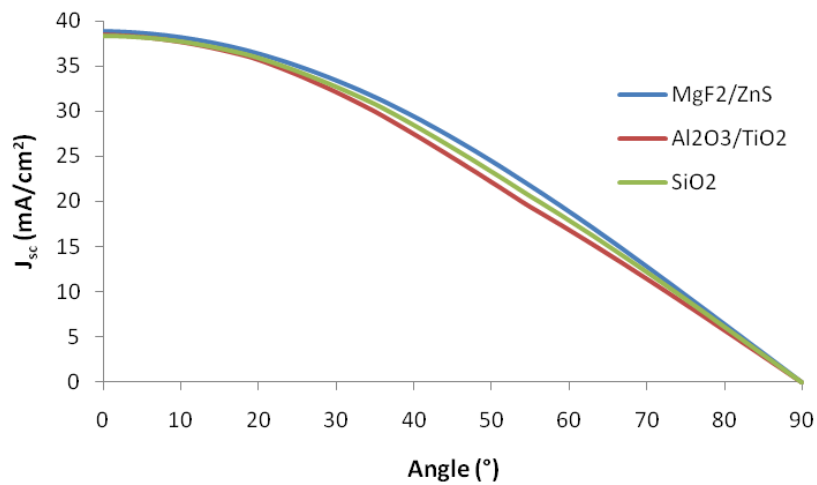
Figure 5.7: J$_{sc}$ vs. angle for textured silicon coated with MgF$_2$/ZnS, Al$_2$O$_3$/TiO$_2$ and SiO$_2$.

5.1.2. Gallium Arsenide Cell

5.1.2.1. Without window layer

Table 5.5 shows the results from modeling a bare GaAs solar cell, one with a single-layer Si_3N_4 coating and one with a double-layer MgF_2/ZnS coating. The model was not as thorough as that for silicon solar cell since the purpose was to demonstrate that the models created could be easily modified to account for different substrates. Seeing as this was not an in-depth investigation of ARCs for GaAs solar cells, fewer materials were considered and angular dependence was neglected.

Figure 5.8 is a graph of SWR as a function of the Si_3N_4 thickness, and Figure 5.9 is a surface plot of SWR as a function of both the MgF_2 and ZnS thicknesses. Both are similar to the ones for silicon solar cells, although the SWR and optimal ARC thicknesses are lower for GaAs because it has a slightly lower refractive index than silicon. Furthermore, due to its higher bandgap, the maximum attainable short circuit current density for GaAs is lower, only 27.711 mA/cm^2 under the AM1.5D spectrum.

ARC	t (nm)	J_{sc} (mA/cm^2)	SWR (%)
None	-	17.830	35.66
Si_3N_4	72	25.995	6.19
MgF_2/ZnS	101 / 53	27.288	1.53

Table 5.5: Optimized results for GaAs without a window layer.
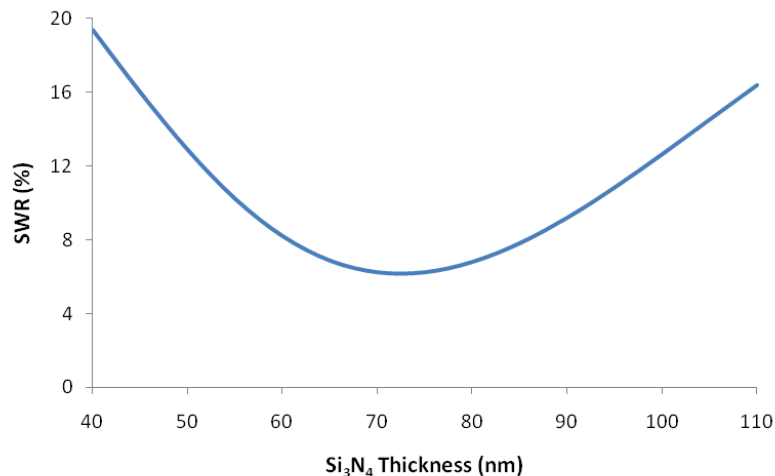
Figure 5.8: SWR of Si_3N_4-coated GaAs.
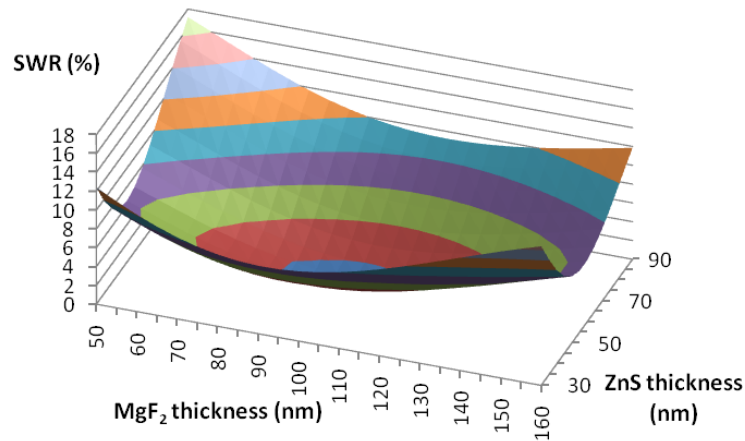
Figure 5.9: Surface plot of SWR for MgF_2/ZnS-coated GaAs.

Table 5.6 shows the theoretical efficiencies associated with the current densities for each optimized scenario. Open-circuit voltage V_{oc} was set at 1.0904 V, resulting in a fill factor of 0.8893 as per the equation in section 4.5. The ensuing efficiencies are very close to those calculated for planar silicon under normal incidence.

ARC	J_{sc} (mA/cm^2)	η (%)
None	17.830	19.21
Si_3N_4	25.995	28.00
MgF_2/ZnS	27.288	29.40

Table 5.6: Optimized J_{sc} and theoretical efficiencies of GaAs without a window layer.

5.1.2.2. With GaInP window layer

By virtue of the models' ideal IQEs, the window layer that would usually reduce surface recombination velocity simply acts as an optical thin film. Normally, a material such as GaInP would raise concern that its bandgap is not wide enough or its extinction coefficient is too high for it to function as a good window layer. However, the refractive index of GaInP is close to that of GaAs and it is sufficiently thin so that absorption becomes negligible. Figure 5.10 is a graph of the reflectance from a thin layer of GaInP on GaAs at a wavelength of 500 nm. The difference between the two curves (one considering absorption and one neglecting it) is minimal for very small thicknesses, demonstrating that the layer can be taken as non-absorbing without sacrificing accuracy.

62
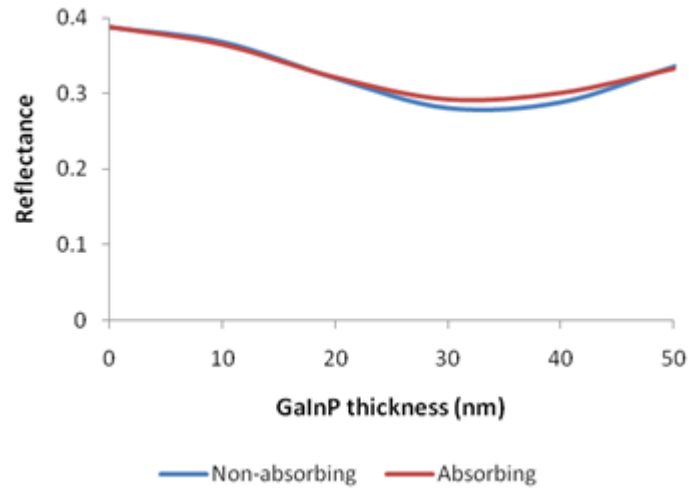
Figure 5.10: Reflectance of thin-film GaInP on GaAs treated as absorbing and non-absorbing.

Table 5.7 summarizes the optimal parameters of several ARC/window layer combinations, as well as the corresponding current densities and SWRs. Figure 5.11 shows the SWR as a function of the layer thicknesses of each model. Compared to a bare GaAs surface, the window layer by itself is capable of lowering reflection about 8%; with the right ARC material, reflection can be reduced further to below 5%. The TiO_2 layer presents an interesting case in which the refractive index of the coating is too high to be favourable and, as a result, the optimal design requires the window layer thickness to become close to zero.

Theoretical efficiencies associated with the current densities for each optimized scenario are shown in Table 5.8. Comparing the efficiency of the Si_3N_4-coated solar cell to one with a Si_3N_4/GaInP coating, it can be seen that the window layer results in an increase of a little more than 0.5%.

ARC	t (nm)	J_{sc} (mA/cm^2)	SWR (%)
GaInP only	42	20.083	27.53
Si_3N_4/GaInP	70 / 36	26.470	4.48
Ta_2O_5/GaInP	68 / 35	26.332	4.98
TiO_2/GaInP	55 / 7	24.960	9.93

Table 5.7: Optimized results for GaAs with a GaInP window layer.
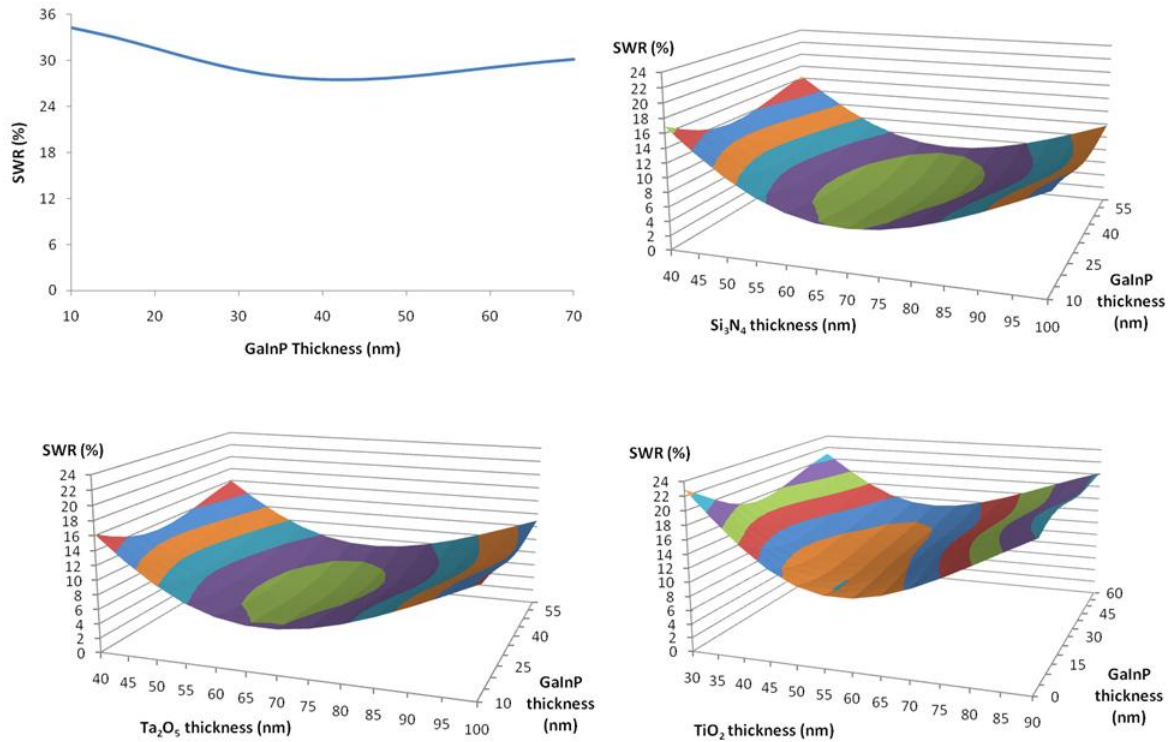
Figure 5.11: SWR of GaAs with a GaInP window layer and various ARCs.

ARC	J_{sc} (mA/cm^2)	η (%)
GaInP only	20.083	21.63
Si_3N_4/GaInP	26.470	28.52
Ta_2O_5/GaInP	26.332	28.37
TiO_2/GaInP	24.960	26.89

Table 5.8: Optimized J_{sc} and theoretical efficiencies of GaAs with a GaInP window layer.

5.2. Multi-Junction Models

5.2.1. Aluminum Gallium Arsenide / Silicon Cell

Figure 5.12 shows how the current density in each subcell varies with the thickness of the top subcell. As the AlGaAs thickness increases, it absorbs more light and leaves less available for absorption by the silicon junction. Thus, the current density decreases in silicon, but since the AlGaAs subcell is current-limiting, the overall current

density of the solar cell increases. The two current density curves do not intersect, indicating that adjusting AlGaAs thickness is not enough to current-match the device.
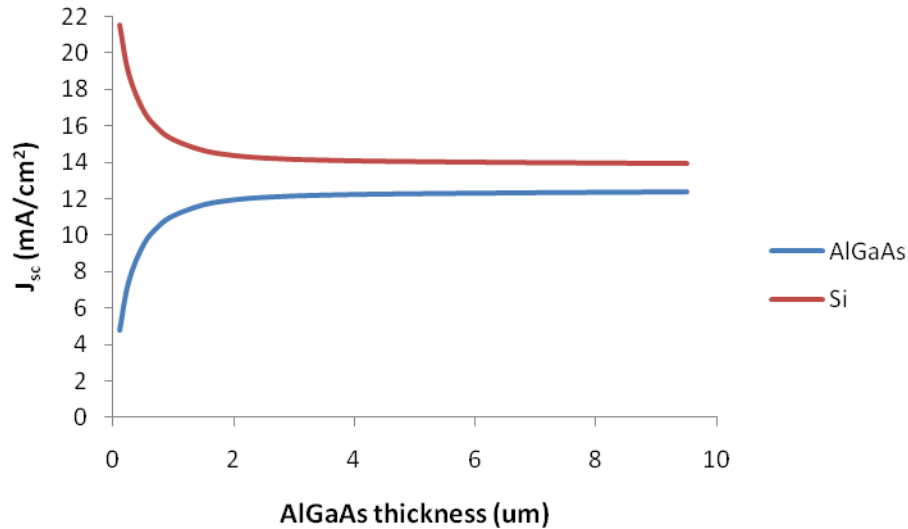
Figure 5.12: J_{sc} of the top and bottom subcells in bare AlGaAs/Si.

Under the AM1.5D spectrum, the maximum attainable short circuit current density for this multi-junction arrangement is 19.523 mA/cm^2. As in the single-junction case, ARCs are crucial to lowering reflection and increasing current density. Table 5.9 summarizes the optimal parameters of several ARCs and the AlGaAs subcell. Since current-matching is not possible without any ARC, the AlGaAs thickness was capped at 250 μm in that case. With the application of a single-layer ARC, the optimal AlGaAs thickness works out to several microns depending on the material. In Figure 5.13, a surface plot shows the output current density of the solar cell as a function of a Si$_3$N$_4$ coating thickness and the AlGaAs subcell thickness. If the Si$_3$N$_4$ coating thickness is held constant, say at 75 nm as in Figure 5.14, the current density curves for the subcells intersect (i.e. the subcells become current-matched), giving the optimal parameters for the device under those conditions.

ARC	t (nm)	AlGaAs (μm)	J_{sc} (mA/cm^2)	SWR (%)
None	-	250	13.019	33.31
Al$_2$O$_3$	85	8.6	17.921	8.20
Si$_3$N$_4$	75	6.7	17.949	8.06
TiO$_2$	60	4.5	17.077	12.53
MgF$_2$/ZnS	114 / 57	22.0	18.990	2.73

Table 5.9: Optimized results for AlGaAs/Si.
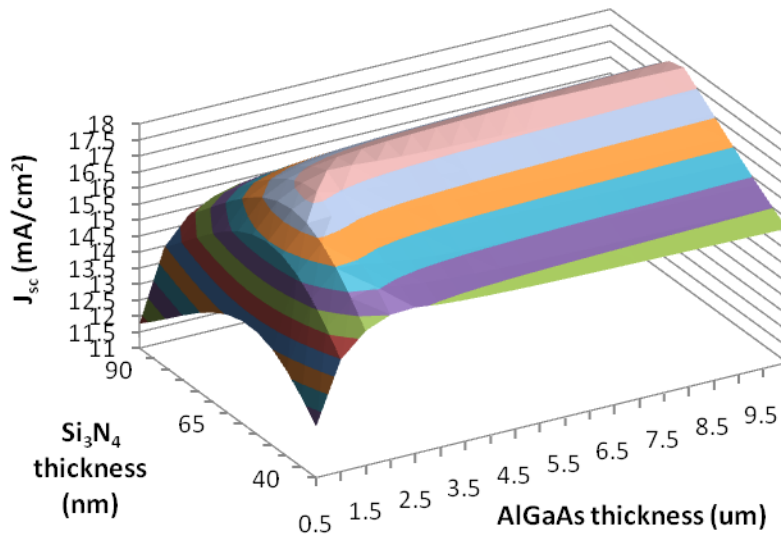
Figure 5.13: Output J_{sc} in Si_3N_4-coated AlGaAs/Si.
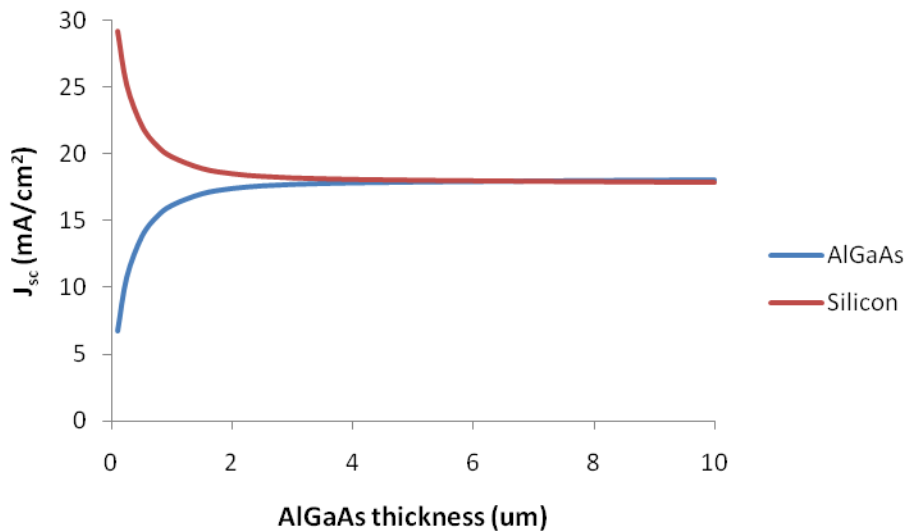
Figure 5.14: J_{sc} of the top and bottom subcells in Si_3N_4-coated AlGaAs/Si.

In Figure 5.15, output current density is plotted as a function of AlGaAs thickness under the application of a MgF_2/ZnS double-layer coating. The optimal thicknesses of the MgF_2 and ZnS for each AlGaAs value are also plotted. Although not shown, the current density peaks at an AlGaAs thickness of 22.0 μm, after which it decreases slightly. Figure 5.16 is an output current density surface plot that varies with MgF_2 and ZnS thickness while the AlGaAs is fixed at 3.0 μm. It is interesting to note that the current density drops

off sharply away from the peak, whereas the same surface plot for a single-junction solar cell would show a much smoother drop-off (essentially the inverse of Figure 5.9). This indicates that the multi-junction solar cell is more sensitive to variations in ARC thickness than a single-junction one.

Figure 5.15: Output J_{sc} and ARC thickness in MgF$_2$/ZnS-coated AlGaAs/Si.
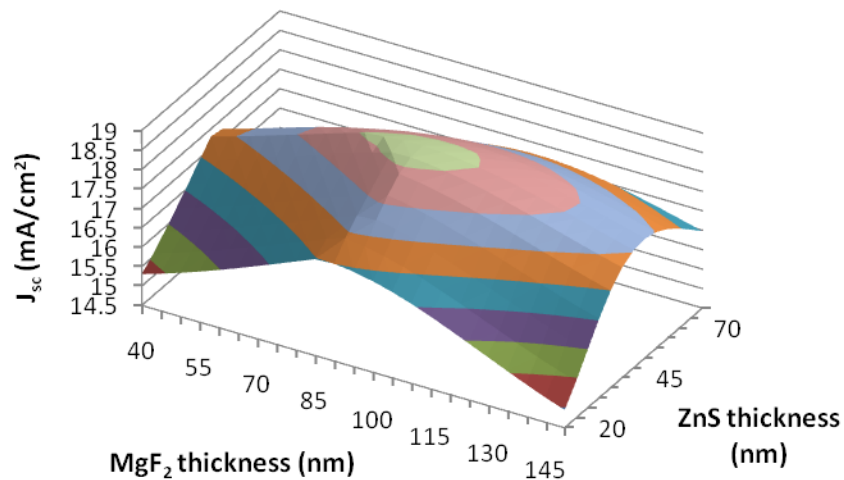
Figure 5.16: Surface plot of output J_{sc} in MgF$_2$/ZnS-coated AlGaAs/Si for an AlGaAs thickness of 3 μm.
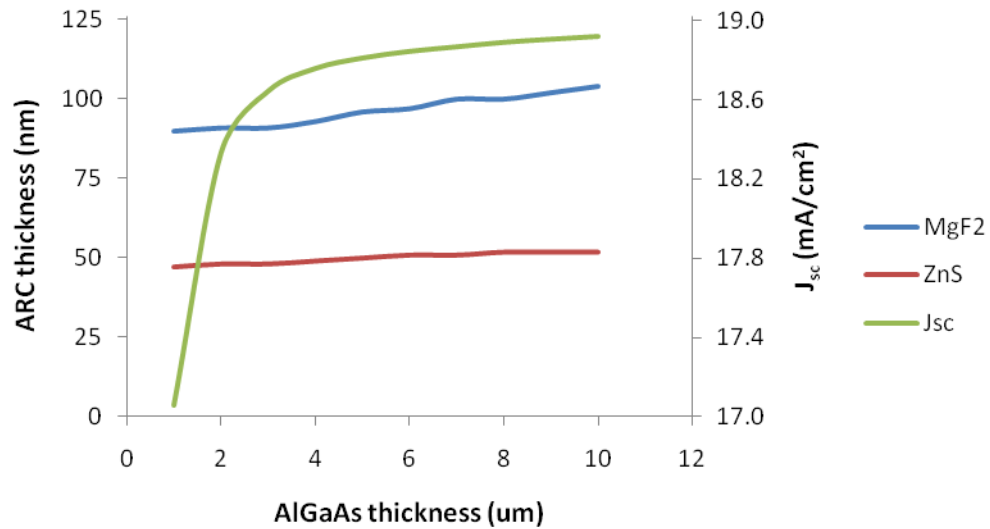
Theoretical efficiencies associated with the current densities for each optimized scenario are shown in Table 5.10. Open-circuit voltage V_{oc} was set at 2.1315 V and a fill factor of 0.8890 was used. The detailed balance limit of single-junction solar cells can easily be surpassed with a single-layer ARC, and with a double-layer coating this multi-junction arrangement can reach an efficiency of just about 40%.

ARC	J_{sc} (mA/cm^2)	η (%)
None	13.019	27.41
Al$_2$O$_3$	17.921	37.72
Si$_3$N$_4$	17.949	37.79
TiO$_2$	17.077	35.95
MgF$_2$/ZnS	18.990	39.98

Table 5.10: Optimized J_{sc} and theoretical efficiencies of AlGaAs/Si.

5.2.2. Gallium Arsenide / Silicon Cell

Figure 5.17 shows how the current density in each subcell varies with the thickness of the top GaAs subcell. As in the AlGaAs/Si multi-junction solar cell, increasing the GaAs thickness allows it to absorb more light and leave less available for absorption by the silicon. However, unlike the AlGaAs/Si solar cell, the two current density curves *do* intersect, meaning that the device can be current-matched solely by adjusting the GaAs thickness (although ARCs are still necessary for increasing efficiency). This also implies that either the GaAs or the silicon can be current-limiting subcell, as opposed to the AlGaAs/Si solar cell in which the AlGaAs was nearly always underpowered and thus current-limiting.

Under the AM1.5D spectrum, the maximum attainable short circuit current density for a GaAs/Si multi-junction solar cell is 19.520 mA/cm^2. Table 5.11 summarizes the optimal parameters of several ARCs and the GaAs subcell. Regardless of the surface treatment, the optimal thickness for GaAs appears to fall within a small range around 0.40 μm, allowing around 30% of light below its bandgap to reach the bottom subcell. In Figure 5.18, a surface plot shows the output current density of the solar cell as a function of a Si$_3$N$_4$ coating thickness and the GaAs subcell thickness. If the Si$_3$N$_4$ coating thickness is held constant, say at 78 nm as in Figure 5.19, the current density curves for the subcells intersect at a higher value compared to those in Figure 5.17 (i.e. in the absence of any coating).
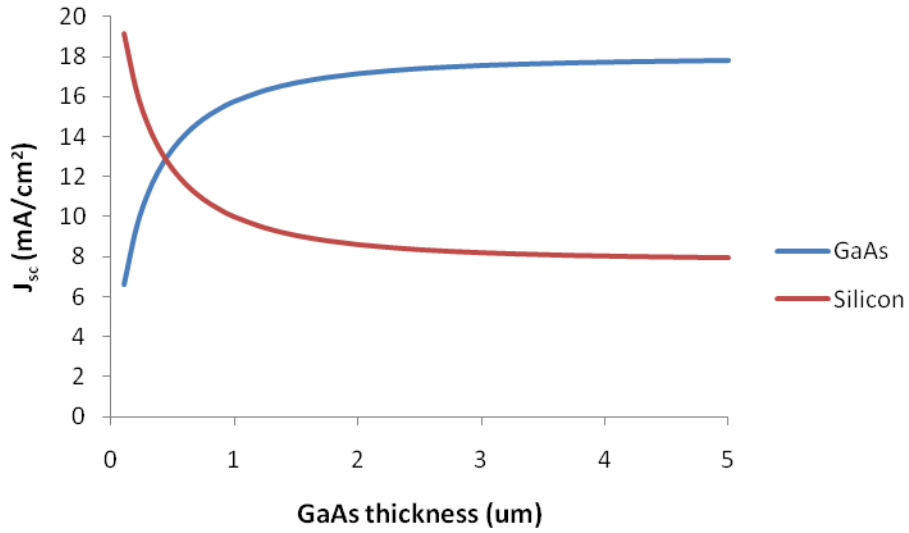
Figure 5.17: J_{sc} of the top and bottom subcells in bare GaAs/Si.

ARC	t (nm)	GaAs (μm)	J_{sc} (mA/cm^2)	SWR (%)
None	-	0.44	12.848	34.18
Al$_2$O$_3$	91	0.40	17.831	8.65
Si$_3$N$_4$	78	0.39	17.905	8.28
TiO$_2$	62	0.38	17.152	12.13
MgF$_2$/ZnS	115 / 59	0.40	19.005	2.64

Table 5.11: Optimized results for GaAs/Si.
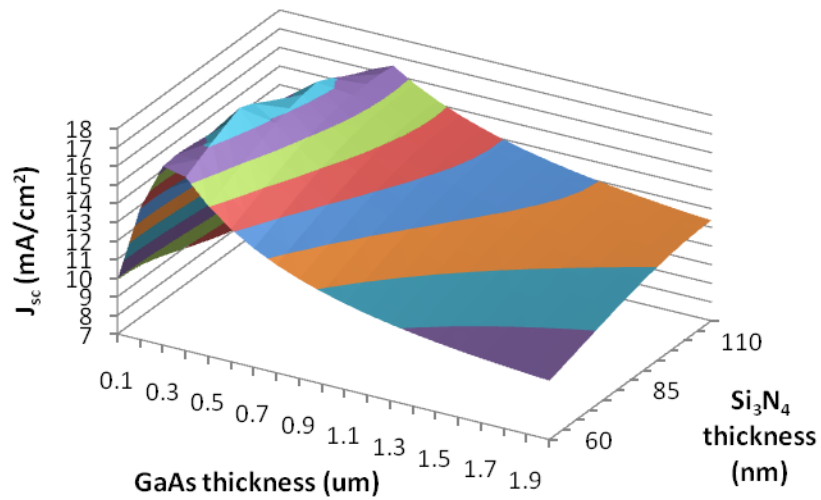
Figure 5.18: Output J_{sc} in Si$_3$N$_4$-coated GaAs/Si.
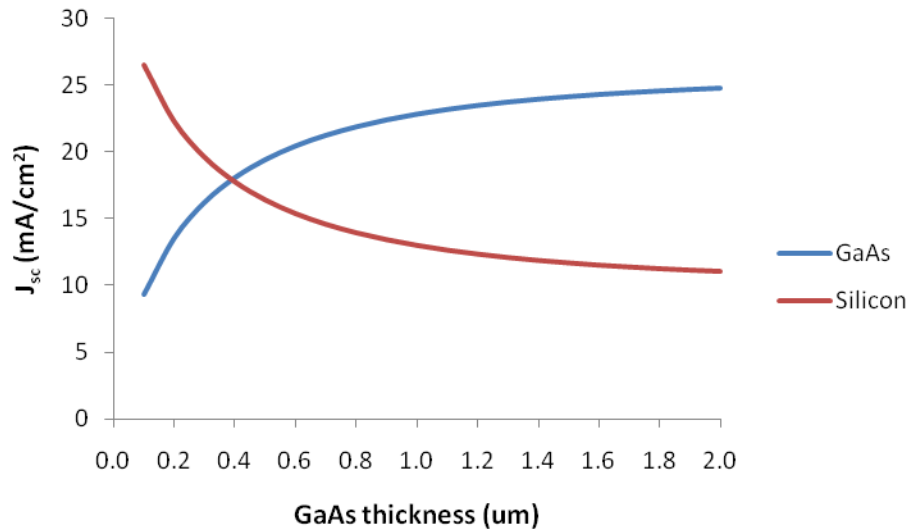
Figure 5.19: J_{sc} of the top and bottom subcells in Si_3N_4-coated GaAs/Si.

In Figure 5.20, output current density is plotted as a function of GaAs thickness under the application of a MgF_2/ZnS double-layer coating. The optimal thicknesses of the MgF_2 and ZnS for each GaAs value are also plotted. The current density peaks at a thickness of 0.40 μm for the GaAs. Figure 5.21 is an output current density surface plot that varies with MgF_2 and ZnS thickness while the GaAs is fixed at 0.40 μm. As in the AlGaAs/Si solar cell, the current density drops off sharply away from the peak, demonstrating the sensitivity to variations in ARC thickness.
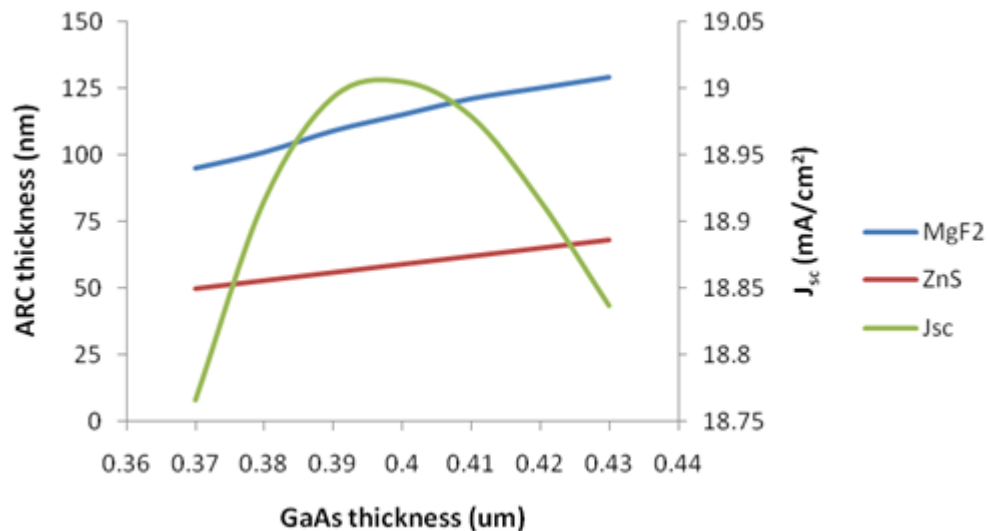
Figure 5.20: Output J_{sc} and ARC thickness in MgF_2/ZnS-coated GaAs/Si.
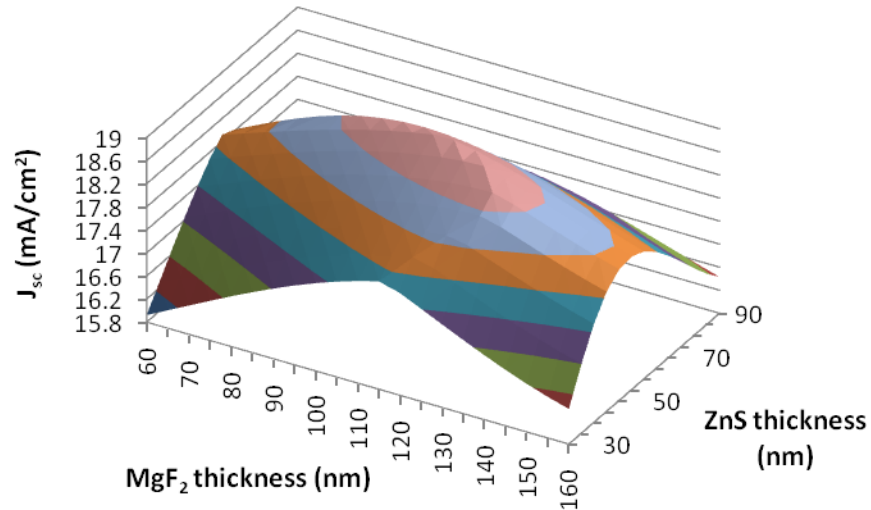
Figure 5.21: Surface plot of output J_{sc} in MgF$_2$/ZnS-coated GaAs/Si for a GaAs thickness of 0.40 μm.

Theoretical efficiencies associated with the current densities for each optimized scenario are shown in Table 5.12. Open-circuit voltage V_{oc} was set at 1.9009 V and a fill factor of 0.8775 was used. The detailed balance limit can once again be surpassed with just a single-layer ARC, although the efficiencies can only reach a little bit beyond 35% even with a double-layer coating. This pales in comparison to the 40% achievable in AlGaAs/Si multi-junction solar cell.

ARC	J_{sc} (mA/cm^2)	η (%)
None	12.848	23.81
Al$_2$O$_3$	17.831	33.04
Si$_3$N$_4$	17.905	33.18
TiO$_2$	17.152	31.78
MgF$_2$/ZnS	19.005	35.22

Table 5.12: Optimized J_{sc} and theoretical efficiencies of GaAs/Si.

5.3. Reflection Analysis

The results presented can be further evaluated by comparing and contrasting the reflectance curves under optimized conditions. Using the planar silicon model as a reference, its reflectance under normal incidence can be compared to that of the textured silicon model, the GaAs model, and the multi-junction models. Comparisons can be made for single-layer and double-layer coating design.

5.3.1. Texturing vs. Anti-Reflection Coating

It is helpful to see the difference in reflection reduction between ARCs and textured surfaces. In Figure 5.22, the reflection curves from textured silicon and TiO_2-coated planar silicon (red and green curves) have approximately same SWR (12.24% and 12.53%, respectively) while exhibiting different characteristics. Since texturing is a geometric method of reducing reflection, the textured silicon curve is nearly identical to the polished silicon reflection curve but with a large vertical shift. The TiO_2-coated planar silicon curve is quite different because it is based on the principle of interference and varies greatly in value due to phase differences. While reflection is hardly reduced at some wavelengths, this is made up for with a minimum where the solar spectrum peaks (i.e. where the number of photons is greatest).
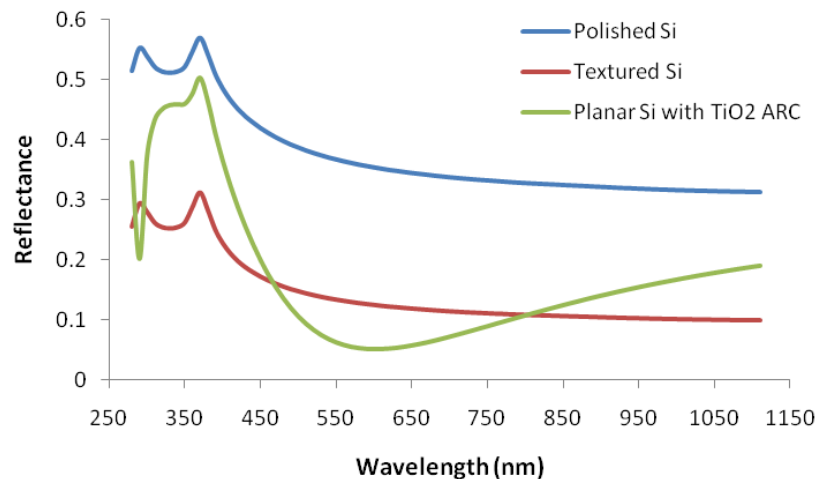
Figure 5.22: Reflectance of bare planar silicon, bare texture silicon and TiO_2-coated planar silicon.

5.3.2. Single-Layer Coating: Si_3N_4

   Figure 5.23 illustrates reflectance for planar and textured silicon. It shows that texturing essentially compresses the planar curve, lowering reflectance for all wavelengths. Whereas the planar reflectance curve has a narrow minimum at around 650 nm, the textured reflectance curve has a broader window of near-zero reflection. Consequently, the SWR drops substantially from 8.69% to 3.00%.
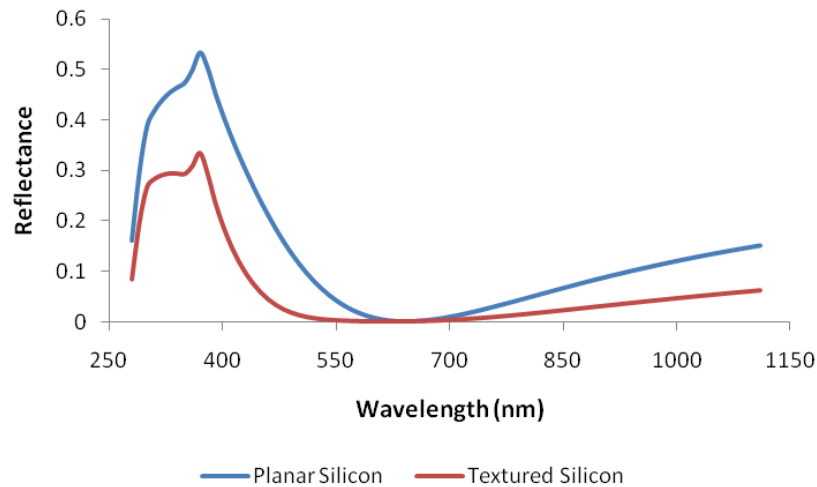
Figure 5.23: Reflectance of Si_3N_4-coated planar and textured silicon.

   Figure 5.24 compares the planar silicon reflectance to that of GaAs. There is a fairly large shift to lower wavelengths (a blue shift) in the curve relative to silicon due to the smaller spectral range of GaAs. The more limited spectral range allows for minimizing reflectance closer to the peak of the solar spectrum by disregarding wavelengths in the near-infrared. As a result, the SWR in the GaAs model is 2.5% lower than in the silicon model (6.19% vs. 8.69%).
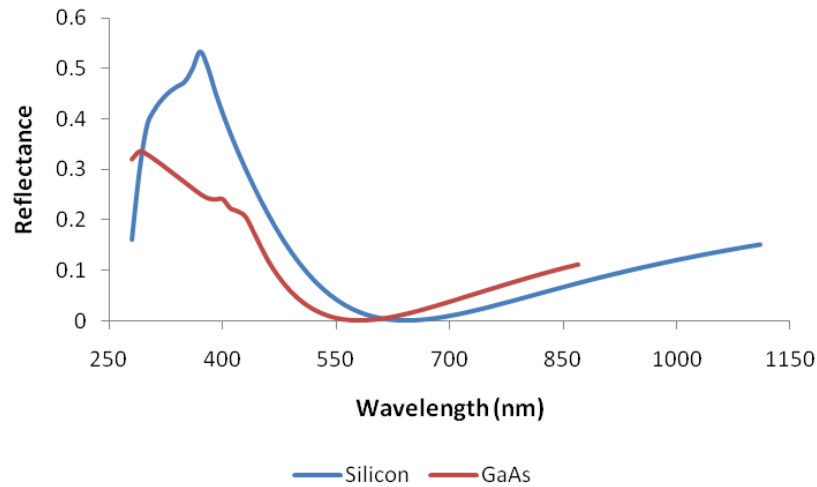
Figure 5.24: Reflectance of Si_3N_4-coated planar silicon and GaAs.

In Figure 5.25, the reflectance of the GaAs/Si model is compared to that of planar silicon. A slight blue shift notwithstanding, the two curves mostly overlap in the visible and near infrared regions of the spectrum. There is a noticeable decrease in reflection in the near-ultraviolet region because of the lower refractive index of GaAs there. However, it only has a minor effect, so the SWR decreases but not appreciably (8.28% vs. 8.69%). The situation is similar in Figure 5.26 for the reflection of AlGaAs/Si. However, the blue shift is more pronounced in this case, resulting in a slightly lower SWR (8.06%) than for GaAs/Si.

Figure 5.25: Reflectance of Si_3N_4-coated planar silicon and GaAs/Si.
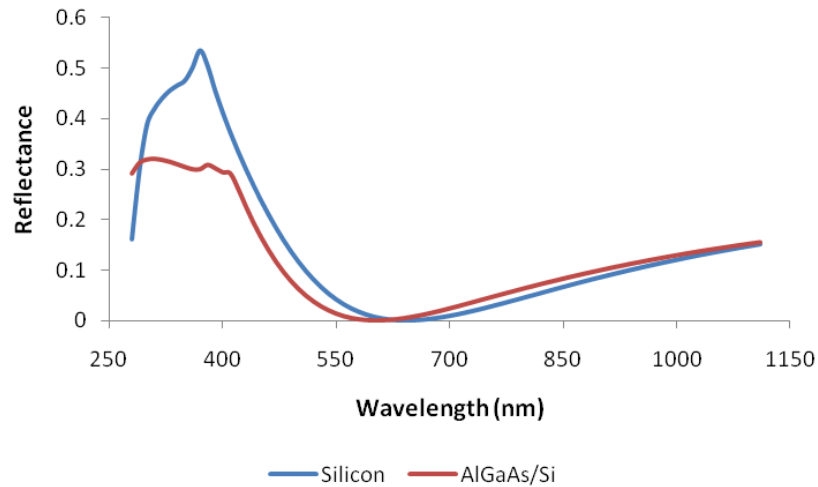
Figure 5.26: Reflectance of Si_3N_4-coated planar silicon and AlGaAs/Si.

5.3.3. Double-Layer Coating: MgF_2/ZnS

In Figure 5.27 is presented the reflectance curves of planar silicon and textured silicon. Both of these curves demonstrate much lower reflectance in the visible and near-infrared than their single-layer counterparts in Figure 5.23. The planar surface contains a fairly broad near-zero reflectance window for wavelengths between 500 nm and 800 nm, which leads to a SWR of 3.00%. On the other hand, for the textured surface, the near-zero reflectance window spans nearly the entire spectral range of interest – from about 400 nm to nearly 1,000 nm. Accordingly, as most of the incident light is captured, the SWR drops to a fraction of a percent (0.61%).
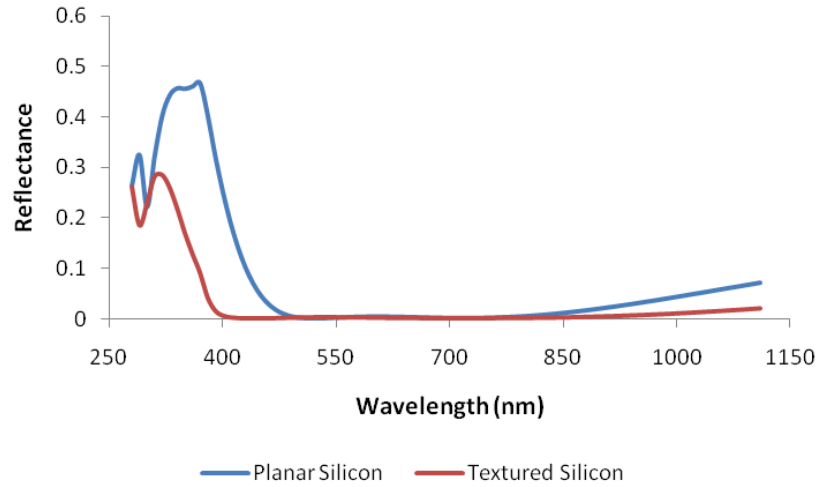
Figure 5.27: Reflectance of MgF_2/ZnS-coated planar and textured silicon.

Figure 5.28 contrasts the reflectance curve for GaAs with that of silicon. The GaAs curve exhibits a broad near-zero reflectance window over a similar range as the silicon curve. Lower reflectance over most of the near-ultraviolet, combined with the irrelevance of reflection from wavelengths in the near-infrared, is enough to decrease the SWR by almost half (1.53% vs. 3.00%).
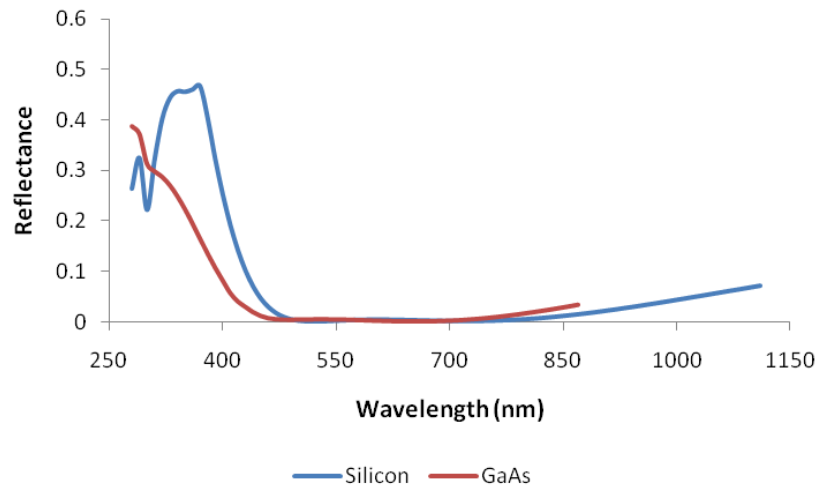
Figure 5.28: Reflectance of MgF_2/ZnS-coated planar silicon and GaAs.

Figures 5.29 and 5.30 are nearly identical due to the similarity in the reflectance curves of GaAs/Si and AlGaAs/Si. As in Figure 5.25, there is nearly perfect overlap with the silicon reflectance curve in the visible and near-infrared regions. The lower reflection

in the near-ultraviolet, as before, results in marginally lower SWRs that are still comparable to the SWR of silicon: 2.64% in the GaAs/Si model and 2.73% in the AlGaAs/Si model.
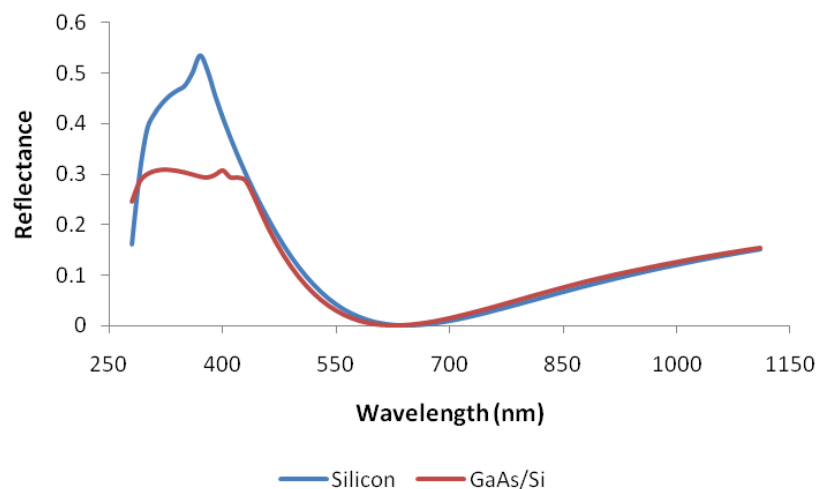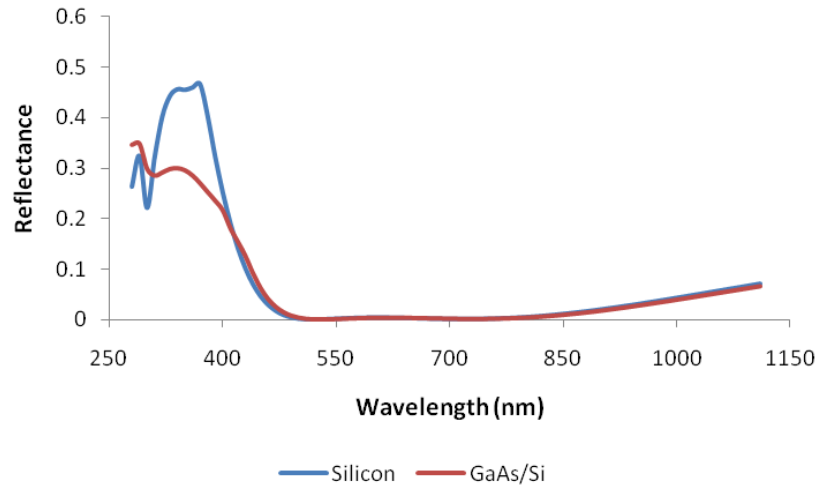

Figure 5.29: Reflectance of MgF$_2$/ZnS-coated planar silicon and GaAs/Si.
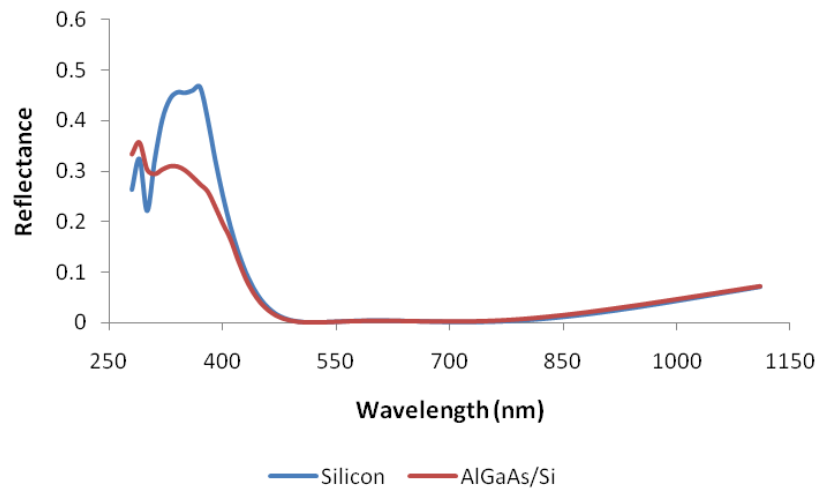
Figure 5.30: Reflectance of MgF$_2$/ZnS-coated planar silicon and AlGaAs/Si.

Chapter 6

Conclusions and Recommended Future Work

In this study, analytic models were created to study ARC design in solar cells. The models took into account the effects of dispersion, polarization and non-normal incidence. In the silicon single-junction models, a method was developed to determine reflection on a textured surface under non-normal incidence. In the GaAs single-junction models, the optical effect of a GaInP window layer was studied. Finally, multi-junction models of AlGaAs/Si and GaAs/Si were optimized by adjusting both the top subcell thickness and ARC. Several conclusions can be reached from the aforementioned results:

• Under normal incidence, a textured substrate with a single-layer ARC performs as well as a double-layer ARC on a planar substrate. When angle-averaged, however, the textured substrate usually comes out ahead as it is able to reduce reflection more effectively at high angles of incidence.

• The best choice of ARC material varies depending on incident angle and surface feature conditions. For example, Si_3N_4 is the best choice under normal incidence on a planar substrate, but under angle-averaged incidence on a textured substrate SiO_2 tops all other single-layer ARCs considered. Furthermore, double-layer coatings are not necessarily better than single-layer coatings under all circumstances. This was seen when the Al_2O_3/TiO_2 combination performed worse than most of the single-layer coatings under angle-averaged incidence on a textured substrate.

• Optimum thicknesses of ARCs also vary depending on the incident angle and surface feature conditions, with the general trend emerging as a lower refractive index resulting in greater variation and vice versa. The optimum thicknesses of SiO_2 ($n \approx 1.46$) and MgF_2 ($n \approx 1.38$) differed considerably, while that of TiO_2 ($n \approx 2.5$) hardly changed.

• A high refractive index window layer can be added and optimized with an ARC to increase absolute efficiency by 0.5% from optical contribution alone. (It would improve efficiency further by increasing internal quantum efficiency within the solar cell, but that effect lies outside the scope of this study). When the refractive index of the ARC is too high, the optimum window layer thickness decreases considerably, which may make it too thin to serve its intended purpose of improving carrier collection.

• GaAs/Si multi-junction solar cells can be current-matched without the use of ARCs, although the coatings are essential for reducing reflection and increasing efficiency. In contrast, for $Al_{0.198}Ga_{0.802}As$/Si cells, the coatings significantly affect the current-matching condition in addition to reducing reflection and increasing efficiency. AlGaAs/Si cells can theoretically reach 40% efficiency with double-layer ARCs, which is comparable to some triple-junction solar cells. GaAs/Si cells can only reach around 35% efficiency with double-layer coatings, but they have the advantage of a top subcell thickness being an order of magnitude smaller.

Based on the results, the models created for this study can be modified in a number of ways to further explore ARC design in solar cells. For instance, the effect of concentration in multi-junction solar cells can be explored. This would require the consideration of non-normal incidence as most solar cells experience an angular distribution of light from concentrators. The effect of encapsulation can also be considered, and reflection from grid contacts can be modeled analytically as well [53]. Finally, in the interest of greater accuracy, the textured surface model can be improved by including tertiary reflections and modifying it to describe non-uniform pyramid distributions. Realistic internal quantum efficiencies can also be included in any of the models fairly easily, if desired.

Bibliography

[1] M. Tsoskounoglou, G. Ayerides and E. Tritopoulou. The end of cheap oil: Current status and prospects. *Energy Policy 36* (2008), pp. 3797-3806.

[2] K. Yu and J. Chen. Enhancing solar cell efficiencies through 1-D nanostructures. *Nanoscale Research Letters 4(1)* (2009), pp. 1-10.

[3] J. Meier et al. Efficiency enhancement of amorphous silicon p-i-n solar cells by LP-CVD ZnO. *Conference Record of the Twenty-Eighth IEEE Photovoltaic Specialists Conference* (2000), pp. 746-749.

[4] H. A. Atwater and A. Polman. Plasmonics for improved photovoltaic devices. *Nature Materials 9(3)* (2010), pp. 205-213.

[5] D. Bouhafs et al. Design and simulation of antireflection coating systems for optoelectronic devices: Application to silicon solar cells. *Solar Energy Mater. Solar Cells 52(1-2)* (1998), pp. 79-93.

[6] S. C. Chiao, J. L. Zhou and H. A. Macleod. Optimized design of an antireflection coating for textured silicon solar-cells. *Appl. Opt. 32(28)* (1993), pp. 5557-5560.

[7] B. L. Sopori and R. A. Pryor. Design of anti-reflection coatings for textured silicon solar-cells. *Solar Cells 8(3)* (1983), pp. 249-261.

[8] H. A. Macleod, *Thin-film optical filters, 2nd ed*. Bristol, Great Britain: Adam Hilger Ltd, 1986.

[9] D. M. Chapin, C. S. Fuller and G. L. Pearson. A New Silicon p-n Junction Photocell for Converting Solar Radiation into Electrical Power. *J. Appl. Phys. 25* (1954), pp. 676-677.

[10] H. C. Barshilia et al. TiAlN/TiAlON/Si3N4 tandem absorber for high temperature solar selective applications. *Appl. Phys. Lett. 89(19)* (2006), pp. 191909.

[11] H. C. Lee et al. Discussion on electrical characteristics of i-In$_{0.13}$Ga$_{0.87}$N p-i-n photovoltaics by using a single/multi-antireflection layer. *Solar Energy Mater. Solar Cells 94(7)* (2010), pp. 1259-1262.

[12] B. Sopori. Dielectric films for si solar cell applications. *J. Electron Mater. 34(5)* (2005), pp. 564-570.

[13] A. Alemu et al. Low temperature deposited boron nitride thin films for a robust anti-reflection coating of solar cells. *Solar Energy Mater. Solar Cells 94* (2010), pp. 921–923.

[14] H. Taguchi, T. Soga and T. Jimbo. Fabrication of GaAs/Si tandem solar cell by epitaxial lift-off technique. *Japanese Journal of Applied Physics Part 2-Letters 42(12A)* (2003), pp. L1419-L1421.

[15] C. E. Valdivia et al. Optimization of antireflection coating design for multi-junction solar cells and concentrator systems. *Proceedings of the Society of Photo-Optical Instrumentation Engineers 7099* (2008), pp. 709915.

[16] T. Yamada et al. 5 x 5 cm^2 GaAs and GaInAs solar cells with high conversion efficiency. *Japanese Journal of Applied Physics Part 2-Letters & Express Letters 44(28-32)* (2005), pp. L985-L987.

[17] A. W. Bett et al. Advanced III-V solar cell structures grown by MOVPE. *Solar Energy Mater. Solar Cells 66(1-4)* (2001), pp. 541-550.

[18] D. J. Aiken. Antireflection coating design for series interconnected multi-junction solar cells. *Progress in Photovoltaics 8(6)* (2000), pp. 563-570.

[19] D. J. Aiken. High performance anti-reflection coatings for broadband multi-junction solar cells. *Solar Energy Mater. Solar Cells 64(4)* (2000), pp. 393-404.

[20] M. F. Schubert et al. Design of multilayer antireflection coatings made from co-sputtered and low-refractive-index materials by genetic algorithm. *Optics Express 16(8)* (2008), pp. 5290-5298.

[21] S. L. Diedenhofen et al. Broad-band and omnidirectional antireflection coatings based on semiconductor nanorods. *Adv Mater 21(9)* (2009), pp. 973-978.

[22] A. Mahdjoub and L. Zighed. New designs for graded refractive index antireflection coatings. *Thin Solid Films 478(1-2)* (2005), pp. 299-304.

[23] S. Callard, A. Gagnaire and J. Joseph. Characterization of graded refractive index silicon oxynitride thin films by spectroscopic ellipsometry. *Thin Solid Films 313* (1998), pp. 384-388.

[24] M. A. Green et al. Very high efficiency silicon solar cells - science and technology. *IEEE Trans. Electron Devices 46(10)* (1999), pp. 1940-1947.

[25] J. M. Gee, R. Gordon and H. F. Laing. Optimization of Textured-Dielectric Coatings for Crystalline-Silicon Solar Cells. *Conference Record of the Twenty-Fifth IEEE Photovoltaic Specialists Conference* (1996), pp. 733-736.

[26] X. Zhu, L. Wang and D. Yang. Investigations of Random Pyramid Texture on the Surface of Single-Crystalline Silicon for Solar Cells. *Proceedings of ISES Solar World Congress* (2007), pp. 1126-1130.

[27] E. S. Marstein et al. Acidic texturing of multicrystalline silicon wafers. *Conference Record of the Thirty-First IEEE Photovoltaic Specialists Conference* (2005), pp. 1309-1312.

[28] J. Hylton, "Light coupling and light trapping in alkaline etched multicrystalline silicon wafers for solar cells," Ph.D. thesis, University of Utrecht, The Netherlands, 2006.

[29] W. J. Yang et al. Internal quantum efficiency for solar cells. *Solar Energy 82(2)* (2008), pp. 106-110.

[30] P. Campbell, S. R. Wenham and M. A. Green. Light trapping and reflection control with tilted pyramids and grooves. *Conference Record of the Twentieth IEEE Photovoltaic Specialists Conference, vols. 1-2* (1988), pp. 713-716.

[31] R. Brendel. Coupling of light into mechanically textured silicon solar-cells - a ray-tracing study. *Progress in Photovoltaics 3(1)* (1995), pp. 25-38.

[32] S. H. Zaidi and S. R. J. Brueck. Si texturing with sub-wavelength structures. *Conference Record of the Twenty Sixth IEEE Photovoltaic Specialists Conference* (1997), pp. 171-174.

[33] K. L. Chopra, P. D. Paulson and V. Dutta. Thin-film solar cells: An overview. *Progress in Photovoltaics 12(2-3)* (2004), pp. 69-92.

[34] C. Y. Tseng, C. K. Lee and C. T. Lee. Performance enhancement of III-V compound multijunction solar cell incorporating transparent electrode and surface treatment. *Progress in Photovoltaics 19(4)* (2011), pp. 436-441.

[35] R. Groenen et al. Surface textured ZnO films for thin film solar cell applications by expanding thermal plasma CVD. *Thin Solid Films 392(2)* (2001), pp. 226-230.

[36] H. Jia, T. Matsui and M. Kondo. Highly-transparent ZnO:Ga through rapid thermal annealing for low-bandgap solar cell application. *34th IEEE Photovoltaic Specialists Conference*, *vols. 1-3* (2009), pp. 1895-1898.

[37] J. Meier et al. Microcrystalline silicon and the impact on micromorph tandem solar cells. *Solar Energy Mater. Solar Cells 74(1-4)* (2002), pp. 457-467.

[38] K. Ramamoorthy et al. Epi-n-ZnO/(100) si, GaAs and InP by L-MBE: A novel approach for III-V devices. *Materials Science in Semiconductor Processing 6(4)* (2003), pp. 219-224.

[39] J. Tommila et al. Nanostructured broadband antireflection coatings on AlInP fabricated by nanoimprint lithography. *Solar Energy Mater. Solar Cells 94(10)* (2010), pp. 1845-1848.

[40] D. J. Poxson et al. Broadband omnidirectional antireflection coatings optimized by genetic algorithm. *Opt. Lett. 34(6)* (2009), pp. 728-730.

[41] M. D. Yang et al. Improvement of conversion efficiency for multi-junction solar cells by incorporation of Au nanoclusters. *Optics Express 16(20)* (2008), pp. 15754-15758.

[42] M. Planck. On the Law of Distribution of Energy in the Normal Spectrum. *Annalen der Physik 4* (1901), pp. 553-563.

[43] G. B. Rybicki and A. P. Lightman, *Radiative Processes in Astrophysics*. New York: John Wiley & Sons, 1979.

[44] J. E. Parrott. Choice of an equivalent black-body solar temperature. *Solar Energy 51(3)* (1993), pp. 195-195.

[45] National Renewable Energy Laboratory, *Reference Solar Spectral Irradiance: Air Mass 1.5* [Online]. Available: http://rredc.nrel.gov/solar/spectra/am1.5/

[46] W. Shockley and H. J. Queisser. Detailed Balance Limit of Efficiency of p-n Junction Solar Cells. *J. Appl. Phys. 32(3)* (1961), pp. 510-519.

[47] F. Dimroth and S. Kurtz. High-efficiency multijunction solar cells. *MRS Bulletin 32(3)* (2007), pp. 230-235.

[48] M. A. Green and M. J. Keevers. Optical-properties of intrinsic silicon at 300 K. *Progress in Photovoltaics 3(3)* (1995), pp. 189-192.

[49] F. L. Pedrotti, L. S. Pedrotti and L. M. Pedrotti, *Introduction to Optics, 3rd ed*. Upper Saddle River, NJ: Pearson Prentice Hall, 2007.

[50] O. S. Heavens, *Optical Properties of Thin Solid Films*. Mineola, NY: Dover Publications Inc., 1991.

[51] SOPRALAB, *Basic N&K Files Database* [Online]. Available: http://www.sopra-sa.com/index2.php?goto=dl&rub=4

[52] S. Adachi, *GaAs and Related Materials: Bulk Semiconducting and Superlattice Properties*. Singapore: World Scientific, 1994.

[53] A. Parretta et al. Angle-dependent reflectance measurements on photovoltaic materials and solar cells. *Opt. Commun. 172(1-6)* (1999), pp. 139-151.

[54] Photovoltaic Education Network, *Arbitrary Orientation and Tilt* [Online]. Available: http://pveducation.org/pvcdrom/properties-of-sunlight/arbitrary-orientation-and-tilt

[55] C. H. Henry. Limiting efficiencies of ideal single and multiple energy-gap terrestrial solar-cells. *J. Appl. Phys. 51(8)* (1980), pp. 4494-4500.

[56] M. A. Green. Accuracy of analytical expressions for solar-cell fill factors. *Solar Cells 7(3)* (1982), pp. 337-340.

Appendix A: Optical Data of Materials Used
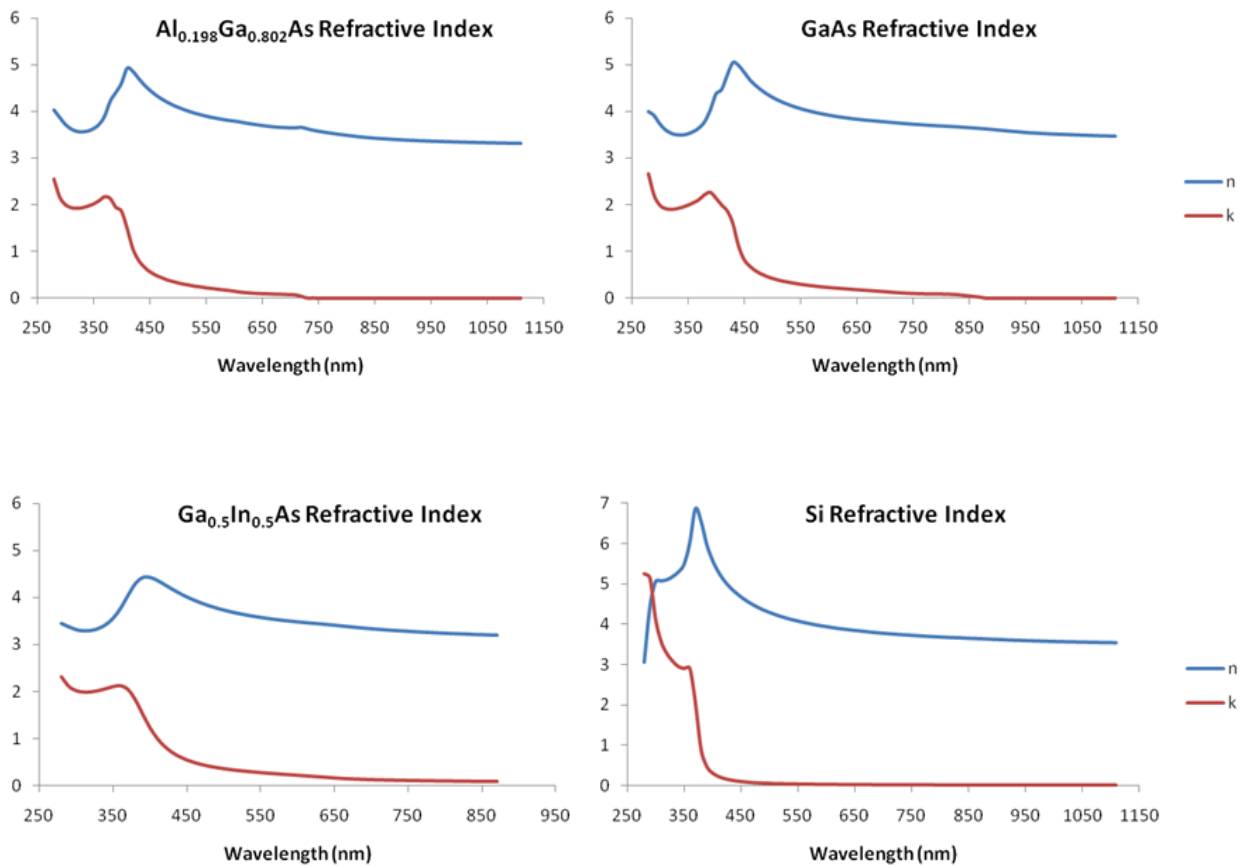
Figure A.1: Real refractive indices and extinction coefficients of semiconductors modeled.
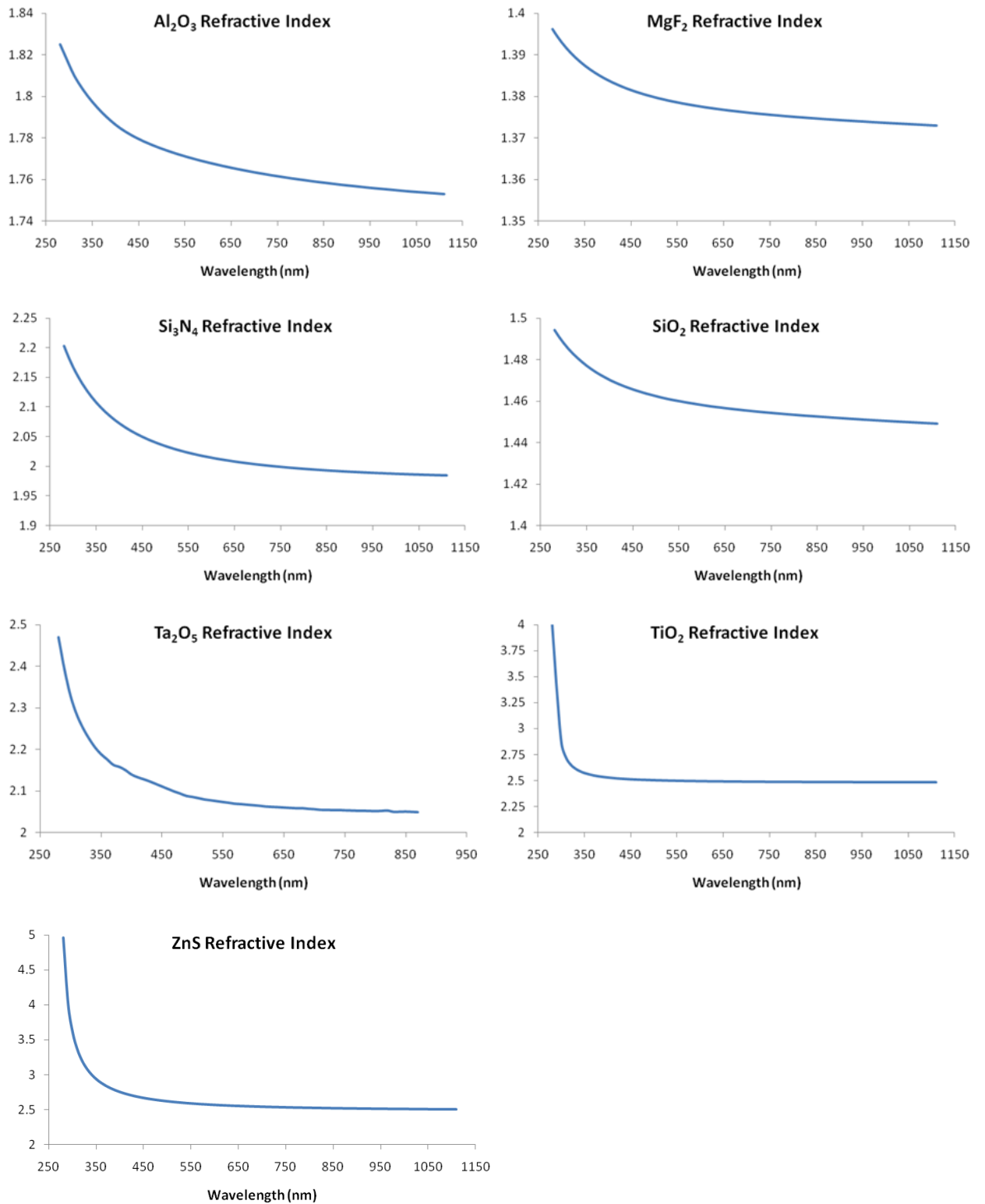
Figure A.2: Refractive indices of ARC materials modeled.

Appendix B: Derivations of Reflectance Equations

Single-layer ARC, normal incidence

Using the transfer matrix from equation 3.24 and setting all cosine terms equal to one, the matrix elements become:

$$\begin{bmatrix} m_{11} & m_{12} \\ m_{21} & m_{22} \end{bmatrix} = \begin{bmatrix} \cos(\delta) & \dfrac{i\sin(\delta)}{n_1\sqrt{\varepsilon_0\mu_0}} \\ i\,n_1\sqrt{\varepsilon_0\mu_0}\,\sin(\delta) & \cos(\delta) \end{bmatrix}$$

Substituting these terms in equation 3.35, dividing by $\sqrt{\varepsilon_0\mu_0}$ and simplifying results in:

$$r = \frac{(n_0 - n_s) + i\left(\dfrac{n_0 n_s}{n_1} - n_1\right)\tan(\delta)}{(n_0 + n_s) + i\left(\dfrac{n_0 n_s}{n_1} + n_1\right)\tan(\delta)}$$

The reflectance is then given by:

$$R = |r|^2 = \frac{(n_0 - n_s)^2 + \left(\dfrac{n_0 n_s}{n_1} - n_1\right)^2 \tan^2(\delta)}{(n_0 + n_s)^2 + \left(\dfrac{n_0 n_s}{n_1} + n_1\right)^2 \tan^2(\delta)}$$

Single-layer ARC, non-normal incidence

The same approach is taken in this case but the cosine terms are kept. Furthermore, two slightly different equations must be derived, one for TE polarization and one for TM polarization. For the former, equation 3.16 applies directly while for the latter a change is to γ_1.

For TE polarization, the transfer matrix elements are:

$$\begin{bmatrix} m_{11} & m_{12} \\ m_{21} & m_{22} \end{bmatrix} = \begin{bmatrix} \cos(\delta) & \dfrac{i\sin(\delta)}{n_1\sqrt{\varepsilon_0\mu_0}\cos(\theta_{t1})} \\ i\,n_1\sqrt{\varepsilon_0\mu_0}\cos(\theta_{t1})\sin(\delta) & \cos(\delta) \end{bmatrix}$$

Substituting these terms in equation 3.35, dividing by $\sqrt{\varepsilon_0\mu_0}$ and simplifying results in:

$$r = \frac{[n_0\cos(\theta_0) - n_s\cos(\theta_s)] + i\left[\dfrac{n_0 n_s}{n_1}\cdot\dfrac{\cos(\theta_0)\cos(\theta_s)}{\cos(\theta_1)} - n_1\cos(\theta_1)\right]\tan(\delta)}{[n_0\cos(\theta_0) + n_s\cos(\theta_s)] + i\left[\dfrac{n_0 n_s}{n_1}\cdot\dfrac{\cos(\theta_0)\cos(\theta_s)}{\cos(\theta_1)} + n_1\cos(\theta_1)\right]\tan(\delta)}$$

The reflectance is then given by:

$$R = \frac{[n_0\cos(\theta_0) - n_s\cos(\theta_s)]^2 + \left[\dfrac{n_0 n_s}{n_1}\cdot\dfrac{\cos(\theta_0)\cos(\theta_s)}{\cos(\theta_1)} - n_1\cos(\theta_1)\right]^2\tan^2(\delta)}{[n_0\cos(\theta_0) + n_s\cos(\theta_s)]^2 + \left[\dfrac{n_0 n_s}{n_1}\cdot\dfrac{\cos(\theta_0)\cos(\theta_s)}{\cos(\theta_1)} + n_1\cos(\theta_1)\right]^2\tan^2(\delta)}$$

For TM polarization, the slight difference in the transfer matrix elements leads to the following:

$$\begin{bmatrix} m_{11} & m_{12} \\ m_{21} & m_{22} \end{bmatrix} = \begin{bmatrix} \cos(\delta) & \dfrac{i\sin(\delta)\cos(\theta_{t1})}{n_1\sqrt{\varepsilon_0\mu_0}} \\ \dfrac{i\,n_1\sqrt{\varepsilon_0\mu_0}\sin(\delta)}{\cos(\theta_{t1})} & \cos(\delta) \end{bmatrix}$$

$$r = \frac{[n_0\cos(\theta_0) - n_s\cos(\theta_s)] + i\left[\dfrac{n_0 n_s}{n_1}\cdot\cos(\theta_0)\cos(\theta_1)\cos(\theta_s) - \dfrac{n_1}{\cos(\theta_1)}\right]\tan(\delta)}{[n_0\cos(\theta_0) + n_s\cos(\theta_s)] + i\left[\dfrac{n_0 n_s}{n_1}\cdot\cos(\theta_0)\cos(\theta_1)\cos(\theta_s) + \dfrac{n_1}{\cos(\theta_1)}\right]\tan(\delta)}$$

$$R = \frac{[n_0 \cos(\theta_0) - n_s \cos(\theta_s)]^2 + \left[\frac{n_0 n_s}{n_1} \cdot \cos(\theta_0) \cos(\theta_1) \cos(\theta_s) - \frac{n_1}{\cos(\theta_1)}\right]^2 \tan^2(\delta)}{[n_0 \cos(\theta_0) + n_s \cos(\theta_s)]^2 + \left[\frac{n_0 n_s}{n_1} \cdot \cos(\theta_0) \cos(\theta_1) \cos(\theta_s) + \frac{n_1}{\cos(\theta_1)}\right]^2 \tan^2(\delta)}$$

Double-layer ARC, normal incidence

With a double-layer thin film arrangement, each layer has a corresponding matrix as generalized in equation 3.26. The matrices are written in the order in which light is incident on them, meaning the first matrix corresponds to the top film and the second matrix corresponds to the bottom film. The transfer matrix can then be set up as follows:

$$
\begin{bmatrix} m_{11} & m_{12} \\ m_{21} & m_{22} \end{bmatrix} = \begin{bmatrix} \cos(\delta_1) & \dfrac{i\sin(\delta_1)}{n_1\sqrt{\varepsilon_0\mu_0}} \\ i\,n_1\sqrt{\varepsilon_0\mu_0}\sin(\delta_1) & \cos(\delta_1) \end{bmatrix} \begin{bmatrix} \cos(\delta_2) & \dfrac{i\sin(\delta_2)}{n_2\sqrt{\varepsilon_0\mu_0}} \\ i\,n_2\sqrt{\varepsilon_0\mu_0}\sin(\delta_2) & \cos(\delta_2) \end{bmatrix}
$$

$$
= \begin{bmatrix} \cos(\delta_1)\cos(\delta_2) - \dfrac{n_2}{n_1}\sin(\delta_1)\sin(\delta_2) & \dfrac{i\cos(\delta_1)\sin(\delta_2)}{n_2\sqrt{\varepsilon_0\mu_0}} + \dfrac{i\sin(\delta_1)\cos(\delta_2)}{n_1\sqrt{\varepsilon_0\mu_0}} \\ i\,n_1\sqrt{\varepsilon_0\mu_0}\sin(\delta_1)\cos(\delta_2) + i\,n_2\sqrt{\varepsilon_0\mu_0}\cos(\delta_1)\sin(\delta_2) & \cos(\delta_1)\cos(\delta_2) - \dfrac{n_1}{n_2}\sin(\delta_1)\sin(\delta_2) \end{bmatrix}
$$

Substituting these terms in equation 3.35 and dividing by $\sqrt{\varepsilon_0\mu_0}$ results in:

$$
r = \frac{\begin{aligned} &n_0\left[\cos(\delta_1)\cos(\delta_2) - \tfrac{n_2}{n_1}\sin(\delta_1)\sin(\delta_2)\right] + i\,n_0 n_s\left[\tfrac{\cos(\delta_1)\sin(\delta_2)}{n_2} + \tfrac{\sin(\delta_1)\cos(\delta_2)}{n_1}\right] \\ &-i[n_1\sin(\delta_1)\cos(\delta_2) + n_2\cos(\delta_1)\sin(\delta_2)] - n_s\left[\cos(\delta_1)\cos(\delta_2) - \tfrac{n_1}{n_2}\sin(\delta_1)\sin(\delta_2)\right] \end{aligned}}{\begin{aligned} &n_0\left[\cos(\delta_1)\cos(\delta_2) - \tfrac{n_2}{n_1}\sin(\delta_1)\sin(\delta_2)\right] + i\,n_0 n_s\left[\tfrac{\cos(\delta_1)\sin(\delta_2)}{n_2} + \tfrac{\sin(\delta_1)\cos(\delta_2)}{n_1}\right] \\ &+i[n_1\sin(\delta_1)\cos(\delta_2) + n_2\cos(\delta_1)\sin(\delta_2)] + n_s\left[\cos(\delta_1)\cos(\delta_2) - \tfrac{n_1}{n_2}\sin(\delta_1)\sin(\delta_2)\right] \end{aligned}}
$$

Upon inspection, the above equation is in the form:

$$
r = \frac{A + iB - iC - D}{A + iB + iC + D}
$$

Thus, the reflectance is will be in the form:

$$
R = |r|^2 = \frac{(A + iB - iC - D)}{(A + iB + iC + D)} \cdot \frac{(A - iB + iC - D)}{(A - iB - iC + D)} = \frac{A^2 + B^2 + C^2 + D^2 - 2(AD + BC)}{A^2 + B^2 + C^2 + D^2 + 2(AD + BC)}
$$

The term AD+BC simply evaluates to $n_0 n_s$. The reflectance is therefore:

$$
R = \frac{\begin{aligned} &n_0^2\left[\cos(\delta_1)\cos(\delta_2) - \tfrac{n_2}{n_1}\sin(\delta_1)\sin(\delta_2)\right]^2 + (n_0 n_s)^2\left[\tfrac{\cos(\delta_1)\sin(\delta_2)}{n_2} + \tfrac{\sin(\delta_1)\cos(\delta_2)}{n_1}\right]^2 \\ &+[n_1\sin(\delta_1)\cos(\delta_2) + n_2\cos(\delta_1)\sin(\delta_2)]^2 + n_s^2\left[\cos(\delta_1)\cos(\delta_2) - \tfrac{n_1}{n_2}\sin(\delta_1)\sin(\delta_2)\right]^2 - 2n_0 n_s \end{aligned}}{\begin{aligned} &n_0^2\left[\cos(\delta_1)\cos(\delta_2) - \tfrac{n_2}{n_1}\sin(\delta_1)\sin(\delta_2)\right]^2 + (n_0 n_s)^2\left[\tfrac{\cos(\delta_1)\sin(\delta_2)}{n_2} + \tfrac{\sin(\delta_1)\cos(\delta_2)}{n_1}\right]^2 \\ &+[n_1\sin(\delta_1)\cos(\delta_2) + n_2\cos(\delta_1)\sin(\delta_2)]^2 + n_s^2\left[\cos(\delta_1)\cos(\delta_2) - \tfrac{n_1}{n_2}\sin(\delta_1)\sin(\delta_2)\right]^2 + 2n_0 n_s \end{aligned}}
$$

Double-layer ARC, non-normal incidence

As in the single-layer case, the cosines are kept in the transfer matrices and an equation for each polarization must be derived. For TE polarization:

$$\begin{bmatrix} m_{11} & m_{12} \\ m_{21} & m_{22} \end{bmatrix}$$

$$= \begin{bmatrix} \cos(\delta_1) & \dfrac{i\sin(\delta_1)}{n_1\sqrt{\varepsilon_0\mu_0}\cos(\theta_1)} \\ i\, n_1\sqrt{\varepsilon_0\mu_0}\cos(\theta_1)\sin(\delta_1) & \cos(\delta_1) \end{bmatrix} \begin{bmatrix} \cos(\delta_2) & \dfrac{i\sin(\delta_2)}{n_2\sqrt{\varepsilon_0\mu_0}\cos(\theta_2)} \\ i\, n_2\sqrt{\varepsilon_0\mu_0}\cos(\theta_2)\sin(\delta_2) & \cos(\delta_2) \end{bmatrix}$$

$$= \begin{bmatrix} \cos(\delta_1)\cos(\delta_2) - \dfrac{n_2\cos(\theta_2)}{n_1\cos(\theta_1)}\sin(\delta_1)\sin(\delta_2) & \dfrac{i\cos(\delta_1)\sin(\delta_2)}{n_2\sqrt{\varepsilon_0\mu_0}\cos(\theta_2)} + \dfrac{i\sin(\delta_1)\cos(\delta_2)}{n_1\sqrt{\varepsilon_0\mu_0}\cos(\theta_1)} \\ i\, n_1\sqrt{\varepsilon_0\mu_0}\cos(\theta_1)\sin(\delta_1)\cos(\delta_2) + i\, n_2\sqrt{\varepsilon_0\mu_0}\cos(\theta_2)\cos(\delta_1)\sin(\delta_2) & \cos(\delta_1)\cos(\delta_2) - \dfrac{n_1\cos(\theta_1)}{n_2\cos(\theta_2)}\sin(\delta_1)\sin(\delta_2) \end{bmatrix}$$

Following the same procedure as previously outlined leads to the following reflectance equation:

$$R = \cfrac{\begin{aligned} &n_0^2\cos^2(\theta_0)\left[\cos(\delta_1)\cos(\delta_2) - \frac{n_2\cos(\theta_2)}{n_1\cos(\theta_1)}\sin(\delta_1)\sin(\delta_2)\right]^2 \\ &+[n_0\cos(\theta_0)n_s\cos(\theta_s)]^2\left[\frac{\cos(\delta_1)\sin(\delta_2)}{n_2\cos(\theta_2)} + \frac{\sin(\delta_1)\cos(\delta_2)}{n_1\cos(\theta_1)}\right]^2 \\ &+[n_1\cos(\theta_1)\sin(\delta_1)\cos(\delta_2) + n_2\cos(\theta_2)\cos(\delta_1)\sin(\delta_2)]^2 \\ &+n_s^2\cos^2(\theta_s)\left[\cos(\delta_1)\cos(\delta_2) - \frac{n_1\cos(\theta_1)}{n_2\cos(\theta_2)}\sin(\delta_1)\sin(\delta_2)\right]^2 - 2n_0\cos(\theta_0)\,n_s\cos(\theta_s)\end{aligned}}{\begin{aligned} &n_0^2\cos^2(\theta_0)\left[\cos(\delta_1)\cos(\delta_2) - \frac{n_2\cos(\theta_2)}{n_1\cos(\theta_1)}\sin(\delta_1)\sin(\delta_2)\right]^2 \\ &+[n_0\cos(\theta_0)n_s\cos(\theta_s)]^2\left[\frac{\cos(\delta_1)\sin(\delta_2)}{n_2\cos(\theta_2)} + \frac{\sin(\delta_1)\cos(\delta_2)}{n_1\cos(\theta_1)}\right]^2 \\ &+[n_1\cos(\theta_1)\sin(\delta_1)\cos(\delta_2) + n_2\cos(\theta_2)\cos(\delta_1)\sin(\delta_2)]^2 \\ &+n_s^2\cos^2(\theta_s)\left[\cos(\delta_1)\cos(\delta_2) - \frac{n_1\cos(\theta_1)}{n_2\cos(\theta_2)}\sin(\delta_1)\sin(\delta_2)\right]^2 + 2n_0\cos(\theta_0)\,n_s\cos(\theta_s)\end{aligned}}$$

For TM polarization:

$$\begin{bmatrix} m_{11} & m_{12} \\ m_{21} & m_{22} \end{bmatrix} = \begin{bmatrix} \cos(\delta_1) & \dfrac{i\sin(\delta_1)\cos(\theta_1)}{n_1\sqrt{\varepsilon_0\mu_0}} \\ \dfrac{i\, n_1\sqrt{\varepsilon_0\mu_0}\sin(\delta_1)}{\cos(\theta_1)} & \cos(\delta_1) \end{bmatrix} \begin{bmatrix} \cos(\delta_2) & \dfrac{i\sin(\delta_2)\cos(\theta_2)}{n_2\sqrt{\varepsilon_0\mu_0}} \\ \dfrac{i\, n_2\sqrt{\varepsilon_0\mu_0}\sin(\delta_2)}{\cos(\theta_2)} & \cos(\delta_2) \end{bmatrix}$$

$$= \begin{bmatrix} \cos(\delta_1)\cos(\delta_2) - \dfrac{n_2\cos(\theta_1)}{n_1\cos(\theta_2)}\sin(\delta_1)\sin(\delta_2) & \dfrac{i\cos(\delta_1)\sin(\delta_2)\cos(\theta_2)}{n_2\sqrt{\varepsilon_0\mu_0}} + \dfrac{i\sin(\delta_1)\cos(\delta_2)\cos(\theta_1)}{n_1\sqrt{\varepsilon_0\mu_0}} \\ \dfrac{i\,n_1\sqrt{\varepsilon_0\mu_0}\,\sin(\delta_1)\cos(\delta_2)}{\cos(\theta_1)} + \dfrac{i\,n_2\sqrt{\varepsilon_0\mu_0}\,\cos(\delta_1)\sin(\delta_2)}{\cos(\theta_2)} & \cos(\delta_1)\cos(\delta_2) - \dfrac{n_1\cos(\theta_2)}{n_2\cos(\theta_1)}\sin(\delta_1)\sin(\delta_2) \end{bmatrix}$$

$$R = \cfrac{\begin{aligned} &n_0^2\cos^2(\theta_0)\left[\cos(\delta_1)\cos(\delta_2) - \frac{n_2\cos(\theta_1)}{n_1\cos(\theta_2)}\sin(\delta_1)\sin(\delta_2)\right]^2 \\ &+[n_0\cos(\theta_0)n_s\cos(\theta_s)]^2\left[\frac{\cos(\theta_2)\cos(\delta_1)\sin(\delta_2)}{n_2} + \frac{\cos(\theta_1)\sin(\delta_1)\cos(\delta_2)}{n_1}\right]^2 \\ &+\left[\frac{n_1\sin(\delta_1)\cos(\delta_2)}{\cos(\theta_1)} + \frac{n_2\cos(\delta_1)\sin(\delta_2)}{\cos(\theta_2)}\right]^2 \\ &+n_s^2\cos^2(\theta_s)\left[\cos(\delta_1)\cos(\delta_2) - \frac{n_1\cos(\theta_2)}{n_2\cos(\theta_1)}\sin(\delta_1)\sin(\delta_2)\right]^2 - 2n_0\cos(\theta_0)\,n_s\cos(\theta_s) \end{aligned}}{\begin{aligned} &n_0^2\cos^2(\theta_0)\left[\cos(\delta_1)\cos(\delta_2) - \frac{n_2\cos(\theta_1)}{n_1\cos(\theta_2)}\sin(\delta_1)\sin(\delta_2)\right]^2 \\ &+[n_0\cos(\theta_0)n_s\cos(\theta_s)]^2\left[\frac{\cos(\theta_2)\cos(\delta_1)\sin(\delta_2)}{n_2} + \frac{\cos(\theta_1)\sin(\delta_1)\cos(\delta_2)}{n_1}\right]^2 \\ &+\left[\frac{n_1\sin(\delta_1)\cos(\delta_2)}{\cos(\theta_1)} + \frac{n_2\cos(\delta_1)\sin(\delta_2)}{\cos(\theta_2)}\right]^2 \\ &+n_s^2\cos^2(\theta_s)\left[\cos(\delta_1)\cos(\delta_2) - \frac{n_1\cos(\theta_2)}{n_2\cos(\theta_1)}\sin(\delta_1)\sin(\delta_2)\right]^2 + 2n_0\cos(\theta_0)\,n_s\cos(\theta_s) \end{aligned}}$$

Absorbing single-layer ARC, normal incidence

The matrix transfer method as presented in section 3.4.2 assumes the thin film is non-absorbing. To account for absorption, all that is needed is to make an adjustment to equation 3.17: the introduction of an exponential term containing the absorption coefficient and film thickness. The rest of the derivation procedure is unmodified.

$$E_{i2} = E_{t1}e^{-i\delta}e^{-\left(\frac{\alpha t}{2}\right)} = E_{t1}e^{-\left(i\delta+\frac{\alpha t}{2}\right)} \quad \text{and} \quad E_{i1} = E_{r1}e^{-i\delta}e^{-\left(\frac{\alpha t}{2}\right)} = E_{r1}e^{-\left(i\delta+\frac{\alpha t}{2}\right)}$$

$$E_b = E_{t1}e^{-\left(i\delta+\frac{\alpha t}{2}\right)} + E_{i1}e^{\left(i\delta+\frac{\alpha t}{2}\right)} = E_{t2}$$

$$B_b = \gamma_1(E_{t1}e^{-\left(i\delta+\frac{\alpha t}{2}\right)} - E_{i1}e^{\left(i\delta+\frac{\alpha t}{2}\right)}) = \gamma_s E_{t2}$$

$$E_{t1} = \left(\frac{\gamma_1 E_b + B_b}{2\gamma_1}\right)e^{\left(i\delta+\frac{\alpha t}{2}\right)}$$

$$E_{i1} = \left(\frac{\gamma_1 E_b - B_b}{2\gamma_1}\right)e^{-\left(i\delta+\frac{\alpha t}{2}\right)}$$

$$E_a = E_{t1} + E_{i1} = \frac{E_b}{2}e^{\left(i\delta+\frac{\alpha t}{2}\right)} + \frac{E_b}{2}e^{-\left(i\delta+\frac{\alpha t}{2}\right)} + \frac{B_b}{2\gamma_1}e^{\left(i\delta+\frac{\alpha t}{2}\right)} - \frac{B_b}{2\gamma_1}e^{-\left(i\delta+\frac{\alpha t}{2}\right)}$$

$$= E_b\left[\cos(\delta)\cosh\left(\frac{\alpha t}{2}\right) + i\sin(\delta)\sinh\left(\frac{\alpha t}{2}\right)\right] + \frac{B_b}{\gamma_1}\left[\cos(\delta)\sinh\left(\frac{\alpha t}{2}\right) + i\sin(\delta)\cosh\left(\frac{\alpha t}{2}\right)\right]$$

$$B_a = \gamma_1(E_{t1} - E_{i1}) = \frac{\gamma_1 E_b}{2}e^{\left(i\delta+\frac{\alpha t}{2}\right)} - \frac{\gamma_1 E_b}{2}e^{-\left(i\delta+\frac{\alpha t}{2}\right)} + \frac{B_b}{2}e^{\left(i\delta+\frac{\alpha t}{2}\right)} + \frac{B_b}{2}e^{-\left(i\delta+\frac{\alpha t}{2}\right)}$$

$$= \gamma_1 E_b\left[\cos(\delta)\sinh\left(\frac{\alpha t}{2}\right) + i\sin(\delta)\cosh\left(\frac{\alpha t}{2}\right)\right] + B_b\left[\cos(\delta)\cosh\left(\frac{\alpha t}{2}\right) + i\sin(\delta)\sinh\left(\frac{\alpha t}{2}\right)\right]$$

$$\begin{bmatrix} E_a \\ B_a \end{bmatrix} = \begin{bmatrix} \cos(\delta)\cosh\left(\frac{\alpha t}{2}\right) + i\sin(\delta)\sinh\left(\frac{\alpha t}{2}\right) & \frac{1}{\gamma_1}\left[\cos(\delta)\sinh\left(\frac{\alpha t}{2}\right) + i\sin(\delta)\cosh\left(\frac{\alpha t}{2}\right)\right] \\ \gamma_1\left[\cos(\delta)\sinh\left(\frac{\alpha t}{2}\right) + i\sin(\delta)\cosh\left(\frac{\alpha t}{2}\right)\right] & \cos(\delta)\cosh\left(\frac{\alpha t}{2}\right) + i\sin(\delta)\sinh\left(\frac{\alpha t}{2}\right) \end{bmatrix}\begin{bmatrix} E_b \\ B_b \end{bmatrix}$$

$$\begin{bmatrix} m_{11} & m_{12} \\ m_{21} & m_{22} \end{bmatrix} = \begin{bmatrix} \cos(\delta)\cosh\left(\frac{\alpha t}{2}\right) + i\sin(\delta)\sinh\left(\frac{\alpha t}{2}\right) & \frac{1}{\gamma_1}\left[\cos(\delta)\sinh\left(\frac{\alpha t}{2}\right) + i\sin(\delta)\cosh\left(\frac{\alpha t}{2}\right)\right] \\ \gamma_1\left[\cos(\delta)\sinh\left(\frac{\alpha t}{2}\right) + i\sin(\delta)\cosh\left(\frac{\alpha t}{2}\right)\right] & \cos(\delta)\cosh\left(\frac{\alpha t}{2}\right) + i\sin(\delta)\sinh\left(\frac{\alpha t}{2}\right) \end{bmatrix}$$

$$r = \frac{\begin{aligned}&n_0\left[\cos(\delta)\cosh\left(\tfrac{\alpha t}{2}\right)+i\sin(\delta)\sinh\left(\tfrac{\alpha t}{2}\right)\right]+\tfrac{n_0 n_s}{n_1}\left[\cos(\delta)\sinh\left(\tfrac{\alpha t}{2}\right)+i\sin(\delta)\cosh\left(\tfrac{\alpha t}{2}\right)\right]\\ &-n_1\left[\cos(\delta)\sinh\left(\tfrac{\alpha t}{2}\right)+i\sin(\delta)\cosh\left(\tfrac{\alpha t}{2}\right)\right]-n_s\left[\cos(\delta)\cosh\left(\tfrac{\alpha t}{2}\right)+i\sin(\delta)\sinh\left(\tfrac{\alpha t}{2}\right)\right]\end{aligned}}{\begin{aligned}&n_0\left[\cos(\delta)\cosh\left(\tfrac{\alpha t}{2}\right)+i\sin(\delta)\sinh\left(\tfrac{\alpha t}{2}\right)\right]+\tfrac{n_0 n_s}{n_1}\left[\cos(\delta)\sinh\left(\tfrac{\alpha t}{2}\right)+i\sin(\delta)\cosh\left(\tfrac{\alpha t}{2}\right)\right]\\ &+n_1\left[\cos(\delta)\sinh\left(\tfrac{\alpha t}{2}\right)+i\sin(\delta)\cosh\left(\tfrac{\alpha t}{2}\right)\right]+n_s\left[\cos(\delta)\cosh\left(\tfrac{\alpha t}{2}\right)+i\sin(\delta)\sinh\left(\tfrac{\alpha t}{2}\right)\right]\end{aligned}}$$

$$=\frac{n_1(n_0-n_s)\left[\cos(\delta)\cosh\left(\tfrac{\alpha t}{2}\right)+i\sin(\delta)\sinh\left(\tfrac{\alpha t}{2}\right)\right]+(n_0 n_s-n_1^2)\left[\cos(\delta)\sinh\left(\tfrac{\alpha t}{2}\right)+i\sin(\delta)\cosh\left(\tfrac{\alpha t}{2}\right)\right]}{n_1(n_0+n_s)\left[\cos(\delta)\cosh\left(\tfrac{\alpha t}{2}\right)+i\sin(\delta)\sinh\left(\tfrac{\alpha t}{2}\right)\right]+(n_0 n_s+n_1^2)\left[\cos(\delta)\sinh\left(\tfrac{\alpha t}{2}\right)+i\sin(\delta)\cosh\left(\tfrac{\alpha t}{2}\right)\right]}$$

$$=\frac{n_1(n_0-n_s)\left[1+i\tan(\delta)\tanh\left(\tfrac{\alpha t}{2}\right)\right]+(n_0 n_s-n_1^2)\left[\tanh\left(\tfrac{\alpha t}{2}\right)+i\tan(\delta)\right]}{n_1(n_0+n_s)\left[1+i\tan(\delta)\tanh\left(\tfrac{\alpha t}{2}\right)\right]+(n_0 n_s+n_1^2)\left[\tanh\left(\tfrac{\alpha t}{2}\right)+i\tan(\delta)\right]}$$

$$R=|r|^2=\frac{\begin{aligned}&(n_0-n_s)^2\left[1+\tan^2(\delta)\tanh^2\left(\tfrac{\alpha t}{2}\right)\right]+2(n_0-n_s)\left(\tfrac{n_0 n_s}{n_1}-n_1\right)\tanh\left(\tfrac{\alpha t}{2}\right)[1+\tan^2(\delta)]\\ &+\left(\tfrac{n_0 n_s}{n_1}-n_1\right)^2\left[\tanh^2\left(\tfrac{\alpha t}{2}\right)+\tan^2(\delta)\right]\end{aligned}}{\begin{aligned}&(n_0+n_s)^2\left[1+\tan^2(\delta)\tanh^2\left(\tfrac{\alpha t}{2}\right)\right]+2(n_0+n_s)\left(\tfrac{n_0 n_s}{n_1}+n_1\right)\tanh\left(\tfrac{\alpha t}{2}\right)[1+\tan^2(\delta)]\\ &+\left(\tfrac{n_0 n_s}{n_1}+n_1\right)^2\left[\tanh^2\left(\tfrac{\alpha t}{2}\right)+\tan^2(\delta)\right]\end{aligned}}$$